ABSTRACT

SHEN, BOWEN. Fiber-Reinforced Polymer Strengthened Steel Reinforced Masonry Wallettes in Out-of-Plane Bending. (Under the direction of Dr. Rudolf Seracino and Dr. Gregory W. Lucier.)

Research on the strengthening of masonry structures subject to out-of-plane bending has focused exclusively on unreinforced masonry (URM) comprised of concrete masonry units (CMU), clay bricks, or natural stone. Consequently, major international fiber-reinforced polymer (FRP) strengthening design guides are limited in their scope to URM. However, a significant portion of today's masonry building stock consists of steel reinforced CMU including, for example, residential construction in coastal areas prone to extreme hydro-meteorological events and earth retaining walls, both of which are subject to out-of-plane loading. Hence, the main purpose of this research is to create the first experimental database of steel reinforced CMU wallettes strengthened with externally bonded (EB) FRP systems subject to out-of-plane bending. The observed flexural behavior and failure modes may then be compared to the predictions of existing design guides and other published models, originally intended for URM.

Nine wallettes were constructed using lightweight two-cell CMUs with nominal overall width and height of 24.5 in. and 80 in., respectively, with a single wythe thickness of 8 in. One of the wallettes served as an unstrengthened control while the other eight were strengthened flexurally on one face with either Glass or Carbon EB-FRP applied using the wet lay-up technique. The wallettes were strengthened and tested in three-point bending in the vertical orientation. All of the strengthened wallettes demonstrated an increase in flexural capacity and post-cracking stiffness, albeit at a reduced out-of-plane displacement. All the CFRP strengthened wallettes, and the one GFRP strengthened wallette that had two-layers of

fabric, failed by intermediate crack (IC) debonding. All of the 1-layer GFRP strengthened wallettes failed by FRP rupture, where the measured maximum FRP strain was at best only 75% of the expected rupture strain. It is speculated that the sharp edge at the masonry flexural crack face may be locally exacerbating the stress concentration resulting in a perceived premature rupture failure. As may be expected, the load carrying capacity and post-cracking stiffness are related to the reinforcement ratio of each FRP strengthening alternative, with that of the CFRP strengthened wallettes higher than that of the GFRP strengthened wallettes. It was interesting to observe that due to the shallow thickness of the wallettes, the flexural capacity was sensitive to the location of the internal steel reinforcing.

It was shown that the measured maximum FRP strain in all cases exceeded the prediction provided by ACI 440.7R-10, which is a design guide for FRP strengthened URM walls. ACI 440.7R-10 is validated for use in design to predict the FRP strain, even though the force per unit width that the FRP system transfers to the masonry substrate exceeded the recommended limit in all cases. On the other hand, the compressive stress-strain relationship of CMU does not have a significant effect on the calculated moment capacity. It is believed that this represents the first experimental test program of FRP-strengthened steel reinforced CMU walls in out-of-plane bending.

Fiber-Reinforced Polymer Strengthened Steel Reinforced Masonry Wallettes in Out-of-Plane Bending

by
Bowen Shen

A thesis submitted to the Graduate Faculty of
North Carolina State University
in partial fulfillment of the
requirements for the degree of
Master of Science

Civil Engineering

Raleigh, North Carolina

2014

APPROVED BY:

_____	_____
Dr. Rudolf Seracino Co-chair of Advisory Committee	Dr. Gregory W. Lucier Co-chair of Advisory Committee

_____
Dr. Sami Rizkalla

DEDICATION

This work is dedicated to my wife, who has always had the highest support for me. I would also like to thank my parents who encouraged and believed in me. Their endless love and selfless sacrifice is appreciated more than they know.

BIOGRAPHY

Bowen SHEN was born in Changchun, Jilin province, China on September 2nd, 1987. He spent his childhood in Changchun. In September 2006, he enrolled at Harbin Institute of Technology (HIT), Harbin, China, where he pursued a Bachelor of Engineering Degree in Civil Engineering in July 2010.

In August 2011, he began to work on his Master of Science Degree in Civil Engineering, specializing in Structural Engineering, under the direction of Dr. Rudolf Seracino and Dr. Gregory W. Lucier at the Constructed Facilities Laboratory (CFL), North Carolina State University, Raleigh, North Carolina.

ACKNOWLEDGMENTS

I would like to thank Dr. Rudolf Seracino and Dr. Gregory W. Lucier for providing me this research opportunity. I will always appreciate their encouragement and direction for the duration of the program. Without their mentoring and hard work, this project would not have been possible. I would also like to thank my other committee member Dr. Sami Rizkalla for the guidance and education he gave me during my time at North Carolina State University.

I would like to thank Pinnacle Masonry, Edge Structural Composites, and the Concrete Reinforcing Steel Institute for donating the materials used in the experimental program. The technical input from Ravi Kanitkar, Gustavo Tumialan, Danks Burton and Travis Cole are all greatly appreciated. I would additionally like to thank the Constructed Facilities Laboratory (CFL) technicians, Mr. Jerry Atkinson and Mr. Jonathan McEntire, for their willingness to answer my questions and guide me in the right direction.

I would like to thank all students at the CFL for their assistance and support, particularly Amir Botros, Chad Goodnight, Cory High, Dillon Lunn, Hamid Kazem, Machel Morrison, Mohamed Nafadi, Milad Hallaji, Nehemiah Mabry, and Bryant Miller. I would also like to recognize Farnam Ghasemzadeh, Natasha Boger, Pavan Chigullapally, Zachary Van Brunt, and Griff Shapack for the happy time they gave me in the office. A special acknowledgment goes to Hao Hu and Yuhao Feng for their encouragement and friendship that I hope will continue forever.

Most of all, I would like to thank my parents who always support and trust in me. I would like to extend special thanks to my wife, Jia Li, for her constant encouragement and love. I also would like to thank my lovely daughter, Jocelyn SHEN, who kept me laughing and made my life colorful.

TABLE OF CONTENTS

LIST OF TABLES

LIST OF FIGURES

Chapter 1 INTRODUCTION

1.1 Background

Steel reinforced concrete masonry unit (CMU) walls are a typical type of wall system. Steel reinforcing bars centrally located in grouted cells increases the out-of-plane bending capacity and ductility of masonry walls. For this reason, a significant portion of today's masonry building stock consists of steel reinforced CMU including, for example, residential construction in coastal areas prone to extreme hydro-meteorological events and earth retaining walls, both of which are subject to out-of-plane loading. According to existing reports (Marshall, 2009), reinforced masonry buildings in Navarre, Florida, that were subjected to wind gusts up to 121 mph due to Hurricane Dennis on July 10th, 2005, performed well with damage limited mainly to roof coverings. However, many of the existing reinforced masonry walls needed to be strengthened in case of damages or changes in loading.

Examples of some traditional methods commonly used to strengthen or repair unreinforced masonry structures include:

- Construction of an additional wythe;
- External application of steel plates; and
- External coating with reinforced cement paste or shotcrete.

However, these methods add considerable weight to the original structure and are labor intensive which will impact the occupants. For these reasons, new strengthening techniques have been developed during the past 20 years using externally bonded (EB) fiber reinforced polymer (FRP) systems.

The efficiency of FRP strengthening of masonry structures subject to out-of-plane bending has been demonstrated by many previous researches. However, past research focused exclusively on unreinforced masonry (URM) comprised of CMU, clay bricks, or natural stone. Consequently, major international FRP strengthening design guides are limited in their scope to URM. To the author's knowledge, there are no efforts or design guidelines on the flexural behavior of the steel reinforced CMU walls. Hence, the main purpose of this research is to create the first experimental database of steel reinforced CMU wallettes strengthened with EB FRP systems subject to out-of-plane bending.

1.2 Objectives

The main objective of this research program is to establish a design procedure and recommendations for FRP strengthened steel reinforced CMU walls subject to out-of-plane bending. To achieve this objective, the following tasks are required:

- Critically assess debonding models related to EB FRP strengthening systems. The fundamental intermediate crack (IC) debonding strain will be calculated using well-

known models and used in a strain based sectional analysis to predict the ultimate flexural strength of each wallette.

- Experimentally examine the effectiveness of various FRP strengthening systems. Eight wallettes with different strengthening systems will be tested to obtain the moment capacity of each wallette and observe the behavior and failure modes.

- Compare the theoretical moment capacity with the experimental data to check the suitability of each debonding model.

- Investigate the full response of the strengthened wallettes by developing a layered-sectional analysis. Once validated, the analysis technique can be used to examine the effect of various parameters. The completed moment-curvature relationship will be given for each wallette.

1.3 Scope

The scope of this research program consists of the construction and testing of nine wallettes, including one unstrengthened control wallette and eight FRP strengthened wallettes. Three parameters will be investigated: type of FRP, FRP width, and number of FRP layers. The following measurements will be recorded during testing: total applied load, FRP tension strain along the length, and the out-of-plane deflection of wallette. Supplementary material tests will be conducted to determine the properties of the materials

used in the experimental program. A comparison will be made with existing FRP IC debonding models. Finally, a recommended design procedure for FRP strengthened steel reinforced CMU wallettes will be provided.

1.4 Layout of the thesis

This thesis contains six chapters. Besides the introduction presented in Chapter 1, the other chapters are arranged as follows:

Chapter 2 provides a review of the previous literature, including previous research and design guides on FRP strengthened concrete structures and URM walls. Five existing IC debonding models are presented and are later used for comparison with the experimental data.

Chapter 3 presents the details of the experimental program. The detailed steps of wallette construction and FRP strengthening procedure are firstly described. In addition, this chapter also describes tests on the materials used, including the mortar, grouted concrete, steel reinforcement, FRP composite, CMU prism and individual CMU. The last part of Chapter 3 provides a description of the test setup and instrumentation used in this experimental program.

Chapter 4 presents the experimental result of each CMU wallette. The failure mode and experimental observations of each wallette is given. In addition, a brief analysis and

discussion of each wallette are also provided, such as the load-strain relationship and the load - mid-height deflection relationship, strain distribution and out-of-plane deformation.

Chapter 5 presents the comparison of the experimental IC debonding strain and the strain calculated using the five different models described in Chapter 2. The layered-sectional analysis approach is then developed to calculate the moment capacity as well as the moment-curvature relationship of each wallette. Finally, a simplified design procedure and recommendations are provided.

Chapter 6 summarizes the conclusions derived from this research program, and provides the recommendations for future work.

Chapter 2 LITERATURE REVIEW

2.1. Introduction

2.1.1. Fiber Reinforced Polymers (FRP)

FRP is a composite material created by combining high strength fibers with a resin matrix. The result is a rigid material that has high strength with light weight. The fibers in the material give the material all of its strength and stiffness characteristics. The primary functions of the resin are to transfer stresses among fibers and protect the fibers from mechanical and environmental damage. Also, resins are used as adhesive to bond the FRP to the masonry substrate in the wet lay-up installation approach.

Two types of fiber are widely used in FRP strengthening of masonry structures: carbon and glass fibers. Based on the fibers used, FRP can be classified as carbon-fiber-reinforced polymer (CFRP) and glass-fiber-reinforced polymer (GFRP). The commonly used resins are epoxy, polyester resins and vinylester. In the wet lay-up approach, a typical strengthening method is combining carbon or glass fibers with epoxy resin. Figure 2.1 shows typical fiber sheets and epoxy resin.

Figure 2.1 – Carbon and Glass Fibers and Resins

The mechanical property of each FRP varies depending on the types of fiber and resin used. Figure 2.2 shows typical stress-strain curves for CFRP, GFRP and mild steel. Compared with steel, there is no yielding for both CFRP and GFRP, which indicates that the FRP is a linear elastic material. In general, the ultimate strength of FRP is much higher than steel, while the ultimate strain is lower. It is important to note that there are a range of properties even within the same type of fiber. The properties of the fibers are dependent on the composition and manufacturer.

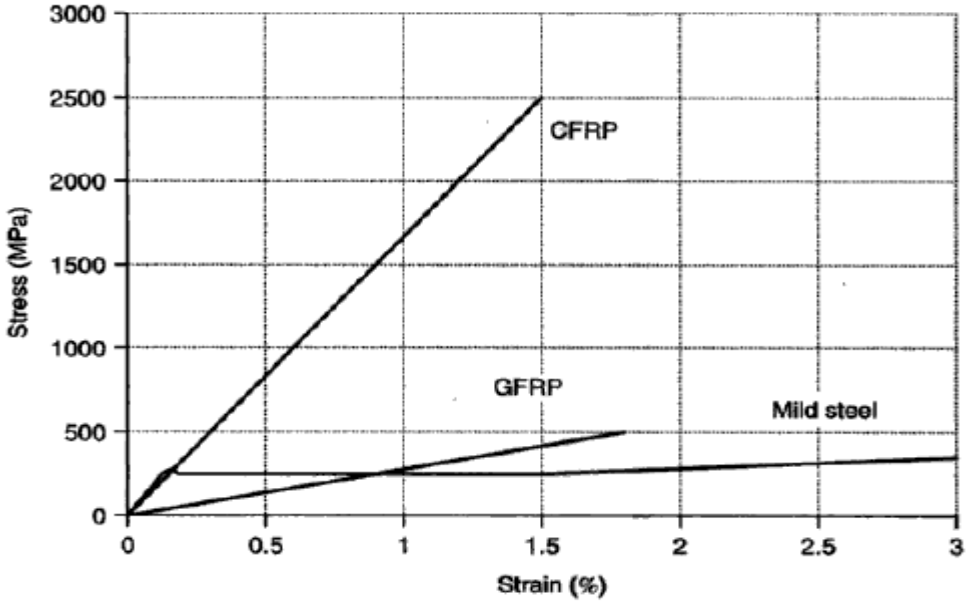

Figure 2.2 - Typical FRP and Mild-steel Stress-strain Curves (Teng & Chen, 2002)

Although the tensile strength is much higher than steel, the density of FRP is only about 20% that of the steel as summarized in Table 2.1. The high strength-to-weight ratio of FRP is the main advantage of the FRP strengthening approach alongside its corrosion resistance. The FRP's light weight and flexibility result in easy installation and reduce the labor cost and impact on the occupants.

Table 2.1 - Typical densities of FRP materials, lb/ft^3 (g/cm^3) (ACI440.2R-08)

Steel	CFRP	GFRP
490 (7.9)	90 to 100 (1.5 to 1.6)	75 to 130 (1.2 to 2.1)

2.1.2. Reinforced Concrete Masonry Unit (CMU) walls

Concrete masonry units (CMUs) are widely used in structural and face veneer applications. CMUs are available in several different sizes. The shape of a typical unit is shown in Figure 2.3. The nominal length and height of the units are generally 16 in. and 8 in., respectively. The width ranges from 4 in. to 12 in. with increments of 2 in.

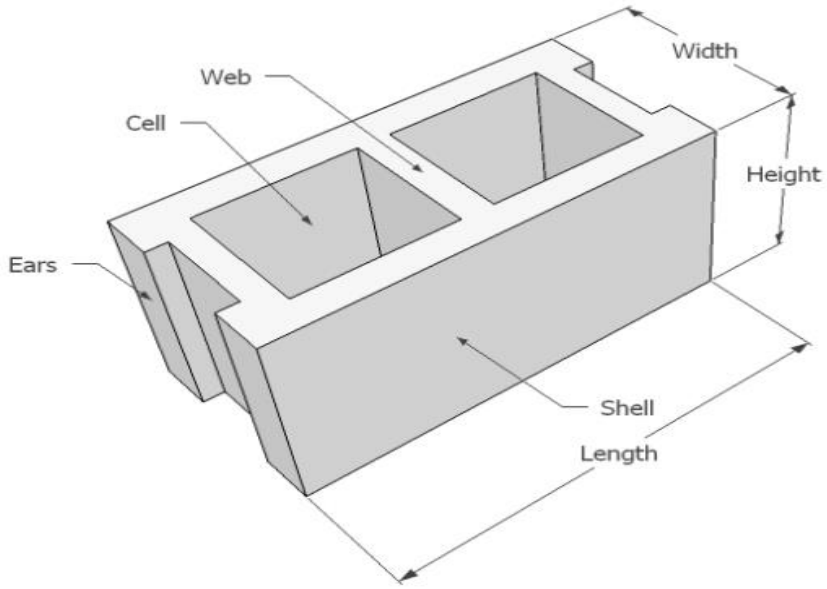

Figure 2.3 - Typical Shape of CMU

There are generally two cores, or cells, in a CMU. The cores are typically tapered for case of demolding in the production process. In addition, the tapered cores can help the mason lift and place the units; the wide side should be on top. The cores are continuous

through the whole height of the units, which allows them to be grouted, typically with concrete. The sectional area of the cores in an 8-in. wide unit is almost 23 in^2, which is large enough to insert a vertical steel rebar within a grouted core. Figure 2.4 shows the typical form of a steel reinforced CMU wall with a running bond pattern.

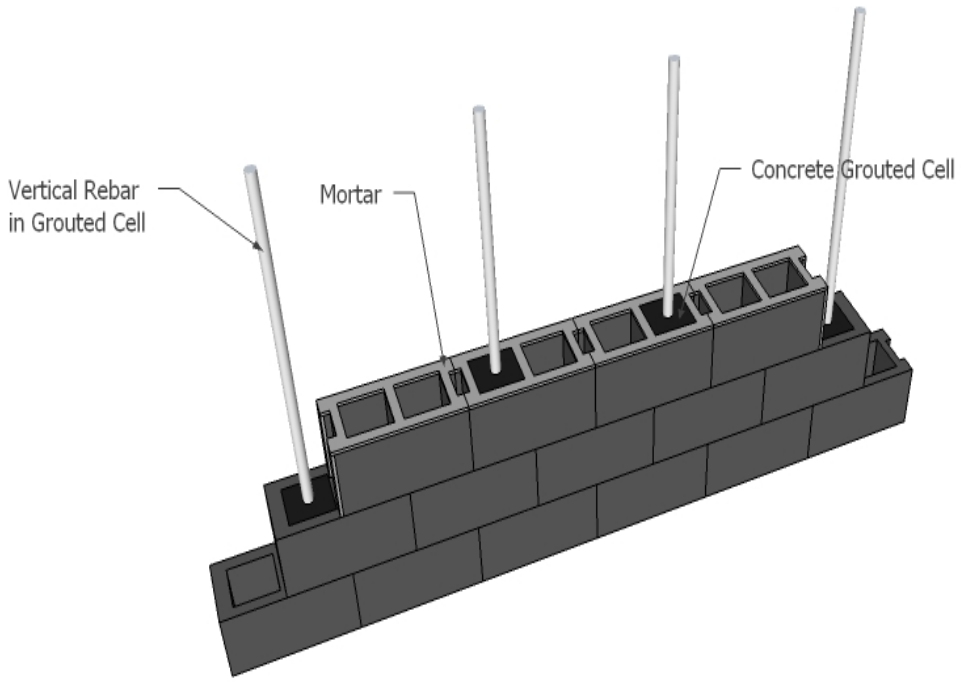

Figure 2.4 -Vertically Reinforced CMU Wall

2.2. Failure Modes of FRP strengthened URM Walls

FRP has been widely applied on masonry structures. Although existing studies focus mainly on unreinforced masonry (URM) walls under out-of-plane loads, they provide good reference of the failure modes. According to those researches, several typical failure modes

have been observed: (1) FRP intermediate crack (IC) debonding; (2) FRP rupture; (3) masonry crushing; and (4) shear failure.

2.2.1 IC Debonding

The debonding of FRP usually occurs at the masonry-FRP interface and starts from flexural cracks at the maximum bending moment region and propagates toward the support, which is called Intermediate Crack (IC) debonding. As the tensile strength of masonry is lower than the epoxy, debonding typically happens in the masonry substrate. IC debonding is a typical failure mode in FRP strengthened URM walls. IC debonding is considered a premature failure mode, since the tensile strength of the FRP material is not fully developed in this case.

Tumialan & Morbin (2002) showed that FRP debonding is the most common failure mode for low FRP reinforcement ratios. They built 25 masonry walls, including 12 concrete-masonry walls and 13 clay-brick walls. The nominal dimensions were 3.75 x 24 x 48 in. All the walls were strengthened with a single strip of GFRP or Aramid FRP on the tension side. The FRP width varied from 3 in. to 12 in. The walls were tested horizontally under simply supported conditions. Figure 2.5 shows the test setup.

Figure 2.5 - Test Setup (Tumialan & Morbin 2002)

Velazquez-Dimas & Ehsani (2000) strengthened seven brick masonry walls with externally bonded (EB) GFRP. The walls were divided into two sets: short walls (48 in. x 28 in.); and tall walls (48 in. x 56 in.). All of the specimens were vertically simply supported and subjected to static cyclic out-of-plane load by an air bag. The load was applied in two stages: (1) A load-controlled stage before cracking; and (2) a displacement-controlled stage with constant maximum displacement. The results showed that debonding controlled the majority of the failure modes of the specimens. Both the flexural capacity and ductility of the walls were significantly enhanced.

2.2.2 FRP Rupture

Compared with IC debonding, the entire tensile strength of FRP is utilized when rupture occurs. However, in most cases, IC debonding will happen before FRP rupture if there are no mechanical anchorages.

Hamilton & Dolan (2001) built four short walls and two tall walls using 8 in. thick normal and lightweight concrete units. The dimensions of the short walls were 2 ft. long by 6 ft. tall and the tall walls were 4 ft. long by 15 ft. 4 in. tall. All the specimens were ungrouted and strengthened vertically with EB GFRP. Each of the short walls was strengthened using a single GFRP strip at the center, while the tall walls were strengthened by 4 vertical GFRP strips. One of the tall walls had two sets of 2-layer strips, the other had 4 single layer strips. The walls were tested vertically using an air bag and reaction frame monotonically to failure. The results showed that the common failure in this program was GFRP rupture.

Albert & Elwi (2001) also observed rupture failure in two CMU walls. One wall was strengthened with two 125 mm carbon sheets, the other was strengthened with 10 125 mm diagonal carbon sheets. Similarly, Tumialan & Morbin (2002) observed the rupture failure in four of the specimens. Only one of them was constructed by concrete block, the other three walls were built using clay bricks.

2.2.3 Masonry Crushing

Masonry crushing is a possible flexural failure mode where the full compressive strength of the masonry is used. It is a typical failure mode for walls under both axial and out-of-plane load. While for simply-supported masonry walls, this failure rarely happens.

Ehsani & Saadatmanesh (1996) built 6 small unreinforced masonry beams with solid clay bricks. All of the beams had the same dimension as 8.5 in. x 4 in. x 57 in. The beams were strengthened by 3 different kinds of GFRP. The first one was a bi-directional fabric with glass fabric and acrylic polyvinyl. The tensile strength in the weak and strong direction were 220 lb./in. and 270 lb./in., respectively. Both of the other fabrics were comprised by unidirectional E-glass fibers, with strength of 1422 lb./in. and 855 lb./in., respectively. All of those beam specimens were tested horizontally under static load to failure by two concentrated loads with a clear span of 47 in. All of the specimens strengthened by the first and third type of GFRP failed by rupture of the composite, while the specimens strengthened by the second type of GFRP failed by compression of the masonry. The test results concluded the rupture occurs when light fabrics are used. However, the compression failure was typical failure for the specimens strengthened by heavy fabrics.

2.2.4 Shear Failure

Tumialan & Morbin (2002) observed shear failure in specimens strengthened with large amounts of FRP. There were two different types of shear failure: flexural-shear and sliding shear. In the flexural-shear mode, the flexural cracks form first, then an almost 45^{o} shear crack develops. This failure might cause FRP debonding because of the small displacement in the shear plane. The out-of-plane capacity of those specimens failed in this mode was increased. Conversely, sliding shear occurs along a bed joint near the boundary support causing sliding of the wall at that location without an increase of flexural capacity.

Hamoush & McGinley (2001) also observed shear failure when testing fifteen 4 ft. x 6 ft. x 8 in. CMU walls, including three control walls. Six of the walls were strengthened both vertically and horizontally using unidirectional GFRP. The others were strengthened by continuous bi-directional glass fibers. The walls were simply supported in the vertical direction and loaded using an air bag. The result showed shear cracks initiated in the web of the masonry at or near the upper support. Failure occurred when the shear crack reached the interface between the fiber and the masonry, at which time a debonding crack propagated along the interface to the fiber sheet ends. This failure is sudden and provided no warning before failure. Similarly, Albert & Elwi (2001) built ten walls strengthened by carbon sheets, glass sheets and carbon plate. All of the specimens were vertically simply-supported and tested under four point bending. Six of the tests failed by flexure-shear. The test result concluded that this failure is the most common mode.

2.3. Design of FRP Strengthened URM Walls

2.3.1. Basic failure modes and assumptions

There are several references available on predicting flexural strength of the masonry walls strengthened with EB FRP. As presented previously, failure is typically controlled by the following modes:

- Crushing of the masonry in compression
- Debonding of the FRP system
- Rupture of the FRP system

Although the failure modes are varied in different design methods, all of them are based on a section analysis with similar assumptions:

- A plane section before loading remains plane after loading, which means the strain is linearly distributed through the full depth of the cross-section;
- The tensile strength of masonry and the compressive strength of FRP are neglected;
- The tensile behavior of FRP is linear elastic up of failure;
- There is no relative slip between EB FRP and the masonry until failure occurs.

2.3.2. Linear Elastic Approach

Velazquez-Dimas and Ehsani (2000) developed a theoretical approach by the assumption that the ultimate flexural strength should be controlled by either tensile rupture or debonding of FRP. Since no compressive failure of brick masonry was expected, the masonry could be considered as a linearly elastic material up to failure of the section. The strain in FRP composites was assumed to be 0.0055 corresponding to the formation of debonding.

Figure 2.6 shows the strain and stress distribution along the cross-section such that the flexural capacity can be calculated by the following Equation 2.1:

$$M_n = \varepsilon_{fe} \cdot A_f \cdot E_{fe} \cdot \left(t_m - \frac{1}{3} \cdot c\right) \tag{2.1}$$

where, ε_{fe} is the tensile strain in FRP composite at failure, A_f is cross-sectional area of FRP laminate, E_{fe} is the elastic modulus of FRP laminate, t_m is the thickness of CMU wall, and c is the depth of neutral axis. As shown in Figure 2.6, ε_m and f_m are the strain and stress in CMU.

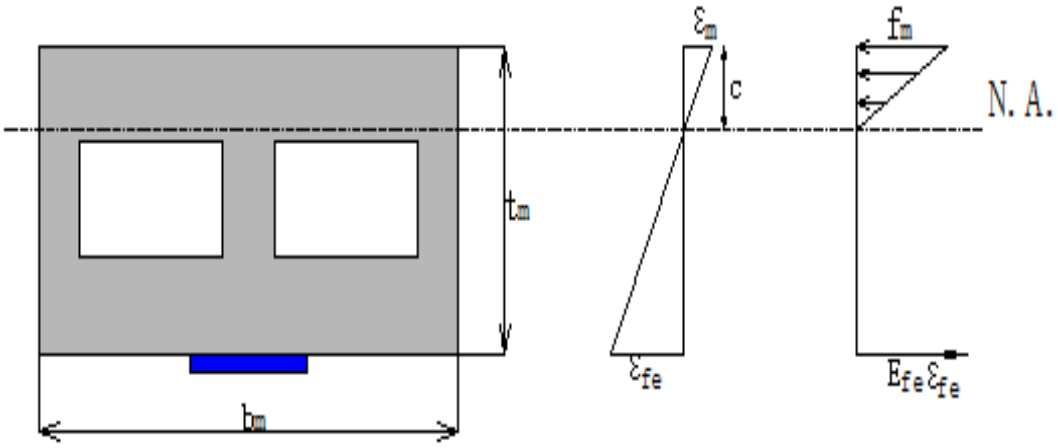

Figure 2.6 - Sectional Analysis (Velazquez-Dimas & Ehsani, 2000)

Albert & Elwi (2001) established a procedure to predict the failure load based on the test results of 13 specimens. The experimental result showed three failure modes: (1) sliding shear; (2) flexure-shear; (3) flexural failure. Unlike Velazquez-Dimas & Ehsani (2000), they do not treat the FRP debonding as a flexural failure mode. Only rupture of FRP and crushing of masonry were considered to control the flexural failure. A triangular stress block was also assumed to calculate the compressive stresses within the masonry face shell. The ultimate load can be obtained by Equation 2.1, however, when masonry crushing governs the failure, the flexural capacity should be calculated by Equation 2.2.

$$M_n = 0.5 \cdot f'_m \cdot b_m \cdot c \cdot \left(t_m - \frac{1}{3} \cdot c\right) \tag{2.2}$$

where b_m is the width of CMU wall, and f'_m is the specified compressive strength of masonry.

2.3.3. Rectangular Stress Block Approach

In contrast to the triangular stress block, a rectangular stress block approach similar to that used in the flexural analysis of reinforced concrete was also used to calculate the compressive force in the FRP strengthened masonry cross section. Figure 2.7 shows the strain and stress distribution within the masonry. The values of γ, β_1 and maximum compressive strain ε_{mu} varies in different methods, which are shown in Table 2.2.

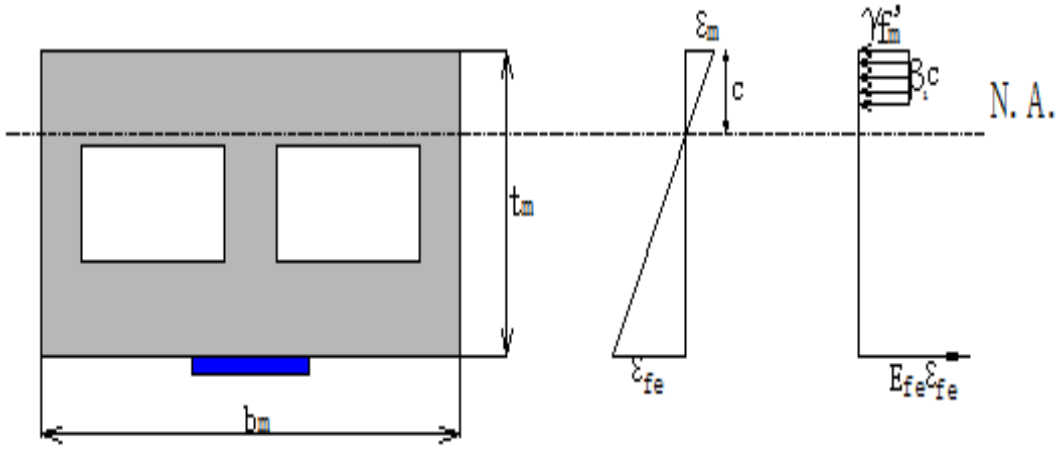

Figure 2.7 - Rectangular Stress Block Approach

Table 2.2 - Values of γ, β_1 and ε_{mu}

	γ	β_1	ε_{mu}
Hamoush & McGinley (2001)	0.85	0.85	0.003 (CMU)
Hamilton & Dolan (2001)	0.85	0.85	0.003 (CMU)
Tumialan & Galati (2003)	0.70	0.70	0.0025 (CMU)
Galati & Garbin (2005)	0.853	0.805	0.0025 (CMU)

Hamilton & Dolan (2001) defined a balanced condition to distinguish between underreinforced and overreinforced conditions. The balanced condition can be calculated by assuming that the maximum strain at masonry crushing occurs at the same time that the FRP fails by rupture. Equation 2.3 gives a formula to compute the balance condition

$$\alpha_c = \frac{b_f}{b_m} = 0.85^2 \cdot t_m \cdot \left(\frac{f'_m}{f_{fu}}\right) \cdot \left(\frac{\varepsilon_{mu}}{\varepsilon_{mu}+\varepsilon_{fu}}\right) \quad (2.3)$$

where α_c is the coverage ratio, b_f is the width of FRP laminate, f_{fu} and ε_{fu} are the ultimate stress and strain of FRP laminate, respectively. When the coverage ratio α_c is less than the balanced condition (underreinforced condition), the wall is likely failed by rupture of FRP. However, the failure mode will be governed by masonry crushing when the coverage ratio is higher than the balanced condition (overreinforced condition). For walls in the overreinforced condition, the moment capacity was mainly dependent on the masonry compressive strength, which is not convenient for existing structures. According to Hamilton

& Holberg (1999), FRP rupture was suggested to be the preferred failure mode in design. Equation 2.4 can be used to predict the flexural capacity in the underreinforced condition.

$$M_n = f_{fu}A_f \cdot \left(t_m - \frac{1}{2} \cdot \frac{f_{fu}A_f}{0.85f'_m b_m}\right) \tag{2.4}$$

Tumialan & Galati (2003) established a rectangular stress block to idealize the compressive distribution. For simplicity, the parameters γ and β_1 can be assumed to be 0.70. However, a detailed expression for parameters γ and β_1 was given as Equations 2.5 and 2.6.

$$\gamma\beta_1 = \left(\frac{\varepsilon_m}{\varepsilon'_m}\right) - \frac{1}{3}\left(\frac{\varepsilon_m}{\varepsilon'_m}\right)^2 \tag{2.5}$$

$$\gamma\beta_1\left(1 - \frac{1}{2}\beta_1\right) = \frac{2}{3}\left(\frac{\varepsilon_m}{\varepsilon'_m}\right) - \frac{1}{4}\left(\frac{\varepsilon_m}{\varepsilon'_m}\right)^2 \tag{2.6}$$

Galati & Garbin (2005) also used the nonlinear behavior of masonry in compression. Before crushing failure occurs, the β_1 and γ can be expressed as Equations 2.7 and 2.8, respectively.

$$\beta_1 = 2 - \frac{4\left[\left(\frac{\varepsilon_m}{\varepsilon_{m'}}\right) - \tan^{-1}\left(\frac{\varepsilon_m}{\varepsilon_{m'}}\right)\right]}{\left(\frac{\varepsilon_m}{\varepsilon_{m'}}\right)\ln\left(1+\left(\frac{\varepsilon_m}{\varepsilon_{m'}}\right)^2\right)} \tag{2.7}$$

$$\gamma = 0.90\frac{\ln\left(1+\left(\frac{\varepsilon_m}{\varepsilon_{m'}}\right)^2\right)}{\beta_1\left(\frac{\varepsilon_m}{\varepsilon_{m'}}\right)} \tag{2.8}$$

where $\varepsilon'_m = \frac{1.71f'_m}{E_m}$ and $\tan^{-1}\left(\frac{\varepsilon_m}{\varepsilon_{m'}}\right)$ is calculated in radians. The maximum usable strain, ε_{mu}, at the extreme compressive face is assumed to be 0.0025 for concrete masonry. The

modulus of elasticity of masonry, E_m, is directly proportional to f_m' for concrete masonry and can be computed by Equation 2.9.

$$E_m = 900 f_m{}' \tag{2.9}$$

2.3.4. Design Guides for FRP Strengthened Unreinforced walls

Besides the research presented, design guides are available for masonry walls strengthened with EB FRP. Among those design guides are ACI 440.7R-10 and CNR_DT200 (2004). Both of these identify IC debonding as the dominate failure mode.

ACI 440.7R-10 is based primarily on the experimental results of Tumialan & Galati (2003) and tests consisting of 25 masonry walls subject to out-of-plane loads. Twelve of the walls were constructed with unreinforced concrete masonry and the rest were built using clay bricks. The surface of the clay brick walls was prepared with putty, while no putty was applied to the concrete masonry walls. A single FRP strip, GFRP or AFRP, was externally bonded at the center of the wall to flexurally strengthen the wall specimens. The FRP width ranged from 3 in. to 12 in. All the specimens were tested horizontally with simply supported boundary conditions. The results showed three failure modes: IC debonding; FRP rupture and shear failure, including flexural-shear failure and shear sliding failure.

The main parameter considered in the Tumialan & Galati (2003) is the reinforcement index ω_f, which is defined by Equation 2.10.

$$w_f = \frac{\rho_f E_f}{f'_m(h/t_m)} \tag{2.10}$$

where ρ_f is the reinforcement ratio of FRP which is defined as the area ratio of the FRP by the cross-section of the wall, h is the height of masonry wall, and f'_m is the specific compressive strength of the masonry. This index was regarded as the main influence on moment capacity, since it represented not only the slenderness ratio of the wall by the (h/t_m) ratio, but also the ratio of axial stiffness between FRP and masonry.

Figure 2.8 describes the effects of the reinforcement index. It should be noted that the theoretical moment capacity was calculated by assuming either FRP rupture or masonry crushing controlled the failure mode. Similarly, a rectangular stress block approach was used to calculate the compressive force in the FRP strengthened masonry cross-section.

According to Figure 2.8, lower bound values of $M_{experimenteal}/M_{theoretial}$ as 0.45 and 0.65 are observed in concrete and clay masonry cases, respectively. Figure 2.8 also shows clearly that shear failure can be avoided in both cases when ω_f is less than approximately 0.70.

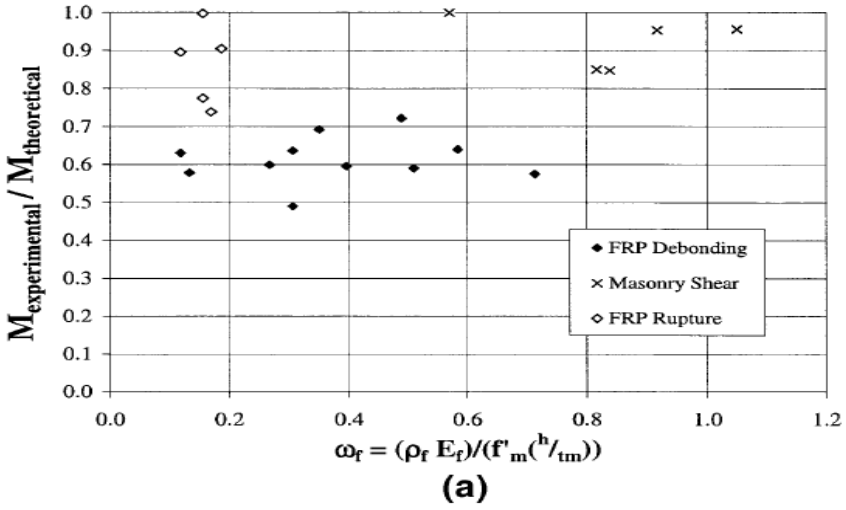

(a) Concrete Masonry

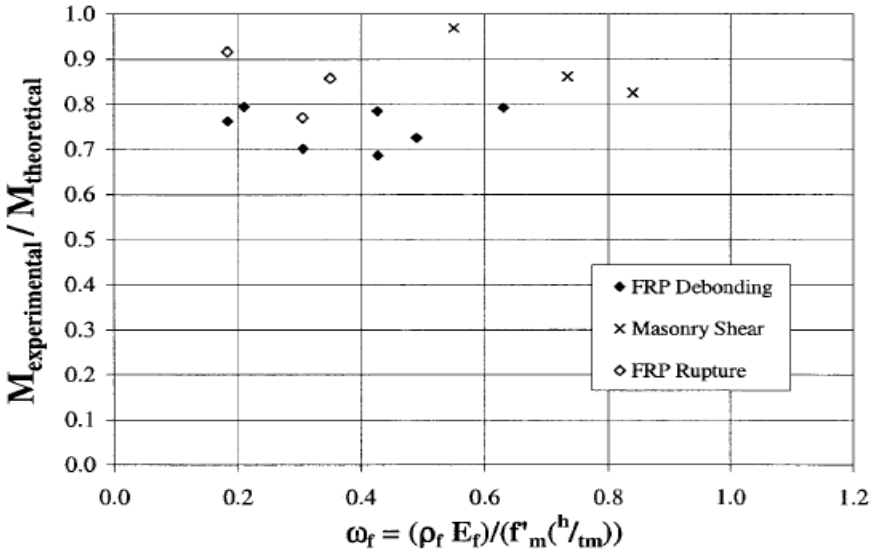

(b) Clay Masonry

Figure 2.8 - Influence of Reinforcement Index (Tumialan & Galati 2003)

ACI 440.7R-10 provides a different expression of FRP reinforcement index ω_f, which is defined by Equation 2.11.

$$w_f = \begin{cases} \frac{1}{1000}\frac{A_f E_f}{A_n\sqrt{f'_m}} & \text{for in.}-\text{lb units} \\ \frac{1}{85}\frac{A_f E_f}{A_n\sqrt{f'_m}} & \text{for SI units} \end{cases} \tag{2.11}$$

Further, ACI 440.7R-10 defines the FRP debonding strain as

$$\varepsilon_{fe} = \kappa_m \varepsilon^*_{fu} \leq C_E \varepsilon^*_{fu} \tag{2.12}$$

To be general and conservative, the bond reduction coefficient κ_m is made equal to 0.45 for EB FRP for both concrete and clay masonry walls based on the result shown in Figure 2.8. In Equation 2.12, ε^*_{fu} is the ultimate FRP rupture strain, and C_E is an environmental reduction factor. The value of C_E is given in Table 2.3.

Table 2.3 - Environmental reduction factors for various FRP systems and exposure conditions (ACI 440.7R-10)

Exposure conditions	Fiber type	Environmental reduction factor C_E
Interior exposure (for example, partitions)	Carbon	0.95
	Glass	0.75
	Aramid	0.85
Exterior exposure (including internal side of exterior walls)	Carbon	0.85
	Glass	0.65
	Aramid	0.75
Aggressive environment (basement walls)	Carbon	0.85
	Glass	0.50
	Aramid	0.70

ACI 440.7R-10 also defines a concept of "development length", which is the maximum active bond length of FRP. Beyond the development length, the bond strength will not increase with increasing bond length. The expression of development length is given as

$$l_d = \begin{cases} \sqrt{\frac{E_f t_f}{50 f_{tm}}} & \text{in.} - \text{lb units} \\ \sqrt{\frac{E_f t_f}{2 f_{tm}}} & \text{SI units} \end{cases} \tag{2.13}$$

where E_f and t_f are the elastic modulus and thickness of the FRP, respectively, and f_{tm} is the average tensile strength of masonry, which can be taken as $0.1f'_m$ if no specific data is provided.

Since the design method of ACI 440.7R-10 is based on relatively limited test data, there is also a limitation of the total force per unit width that the FRP system transfers to the masonry substrate, which is given in Equation 2.14

$$P_{fm} = \begin{cases} nt_f f_{fe} \leq 1500\,\text{lb/in.} & \text{in.}-\text{lb units} \\ nt_f f_{fe} \leq 260\,\text{N/mm} & \text{SI units} \end{cases} \tag{2.14}$$

The design method of ACI 440.7R-10 is based on relatively limited test data, and the only parameter in this approach is the ultimate strain of FRP reduced by κ_m. Although this approach is simple, many other factors whose influence on debonding has been widely accepted are not considered, such as the width of FRP, masonry compressive strength and the FRP tensile strength. Hence, the ACI 440.7R-10 might be expected to be unsuitable in some cases.

On the other hand, CNR_200 (2004) considers many parameters which are ignored by ACI 440.7R-10. CNR_200 (2004) recommends a bond resistance model that considers the specific fracture energy Γ_{Fk}, which can be calculated as follows:

$$\Gamma_{Fk} = C_1 \cdot \sqrt{f_{mk} f_{mtm}} \tag{2.15}$$

where C_1 can be taken as 0.015 if no specific data is available, f_{mk} is the characteristic compressive strength of masonry, and f_{mtm} is the masonry average tensile strength, which may be assumed equal to $0.1f_{mk}$ if no specific data is available.

If the bond length is beyond the optimal (effective) bond length, the design bond strength is expressed as

$$f_{fdd} = \frac{1}{\gamma_{f,d}\sqrt{\gamma_M}} \cdot \sqrt{\frac{2E_f \Gamma_{Fk}}{t_f}} \tag{2.16}$$

where $\gamma_{f,d}$ and γ_M are partial safety factors. For research purposes, both $\gamma_{f,d}$ and γ_M can be taken as 1.0.

The optimal bond length (development length) is given as

$$L_e = \sqrt{\frac{E_f t_f}{2f_{mtm}}} \tag{2.17}$$

When the bond length, L_b, is less than L_e, the bond strength shall be reduced to

$$f_{fdd} = f_{fdd} \cdot \frac{L_b}{L_e} \cdot \left(2 - \frac{L_b}{L_e}\right) \tag{2.18}$$

Although this model is more robust than the ACI 440.7R-10 approach, the CNR_DT 200 (2004) indicates that the ultimate compressive strain of masonry is 0.35%, which is a typical value for clay bricks. Hence, CNR_DT200 (2004) might not be suitable for CMU wallettes.

2.4. Existing Models for IC Debonding

Since both ACI440.7R-10 and CNR_200 (2004) confirm that IC debonding is the dominate failure model in masonry walls strengthened with FRP systems. And since sectional analysis is used to calculate the moment capacity of FRP strengthened masonry walls, it is critical to accurately predict the IC debonding strain in a design procedure. There is a lot of research on the out-of-plane behavior of concrete members, and existing models are available to calculate the FRP IC debonding strain. Although the materials and specimens are not the same as masonry, they do provide valuable references.

Chen & Teng (2001) presented a well-known model to predict the bond resistance of EB FRP-to-concrete joints. This model is based on a collection of published experimental test data and includes the effect of effective bond length (development length). For well-prepared specimens, failure propagates in the concrete beneath the plate-to-concrete interface. They considered the effect of the width ratio by defining a width ratio coefficient, β_p

$$\beta_p = \sqrt{\frac{2-b_p/b_c}{1+b_p/b_c}} \tag{2.19}$$

where b_p and b_c are the width of FRP and concrete, respectively. It should be noted that there is a lower bound limit of 0.33 for the width ratio b_p/b_c. Then, a simple IC debonding model was given by the following, using units of Newton and mm.

$$\varepsilon_{IC} = \alpha \cdot \beta_p \cdot \beta_L \cdot \sqrt{\frac{\sqrt{f_c'}}{E_p t_p}} \tag{2.20}$$

where f_c' is the cylinder concrete compressive strength, E_p and t_p are the elastic modulus and thickness of FRP, respectively, and α is a factor to fit this model to the test data. For flexural members, such as slabs, the value of α is given by

$$\alpha = \begin{cases} 0.72 & \text{for mean of slab test} \\ 0.478 & \text{for 95\% confidence limit of slab test} \end{cases} \tag{2.21}$$

Further, the effective bonded length (development length) coefficient, β_L, is defined as

$$\beta_L = \begin{cases} 1 & \text{if } L \geq L_e \\ \sin\frac{\pi L}{2L_e} & \text{if } L < L_e \end{cases} \tag{2.22}$$

where L is the bonded length and L_e is the effective bond length given by

$$L_e = \sqrt{\frac{E_p t_p}{\sqrt{f_c'}}} \tag{2.23}$$

Based on a statistical analysis of over 200 existing test results of FRP strengthened beams and slabs, Said & Wu (2008) proposed another IC debonding model. By comparing the relationship between IC debonding strain and the axial FRP stiffness $E_f t_f$, the basic equation of the debonding strain, ε_{db}, was established as

$$\varepsilon_{db} = C_1 (f_c')^{C_2} / \left(E_f t_f\right)^{C_3} \tag{2.24}$$

where E_f and t_f are the modulus of elastic of FRP and thickness of FRP, respectively. C_1, C_2 and C_3 are constant determined by optimizing the predicted-to-experimental load ratios. The values of C_1, C_2 and C_3 were statistically obtained to be 0.23, 0.2 and 0.35, respectively.

This model assumes that the debonding strain is only affected by the concrete compressive strength and FRP axial stiffness. Similarly, ACI 440.2R-08 considers the compressive strength of concrete and the FRP axial stiffness, which is the same as Chen & Teng (2001) and Said & Wu (2008). The expression of debonding strain, ε_{fd}, in ACI 440.2R-08 is given as follows:

$$\varepsilon_{fd} = \begin{cases} 0.083\sqrt{\frac{f_c'}{nE_f t_f}} \leq 0.9\varepsilon_{fu} & \text{in in.}-\text{lb units} \\ 0.41\sqrt{\frac{f_c'}{nE_f t_f}} \leq 0.9\varepsilon_{fu} & \text{in SI units} \end{cases} \tag{2.25}$$

where n is the number of layers of FRP reinforcement, and ε_{fu} is the design rupture strain, which is defined as ultimate rupture strain of the FRP, ε_{fu}^*, multiplied by environmental reduction factor C_E.

The ACI 440.2R-08 guide also gives the following expression for development length, l_{df}

$$l_{df} = \begin{cases} 0.057\sqrt{\frac{nE_f t_f}{\sqrt{f_c'}}} & \text{in in.}-\text{lb units} \\ \sqrt{\frac{nE_f t_f}{\sqrt{f_c'}}} & \text{in SI units} \end{cases} \tag{2.26}$$

2.5. Literature Review Summary

Though some design guides are available on externally bonded FRP strengthened concrete and masonry members (both concrete and clay brick), no guidelines explicitly consider FRP strengthened steel reinforced concrete masonry walls. And, ACI 440.7R-10, which ignores the majority of the parameters known to affect the IC debonding strain, determines the debonding strain only using the ultimate strain of the FRP reduced by a constant reduction factor, κ_m, which does not seem to be sufficient.

Further, ACI 440.7R-10 establishes the design approach based only on the test data of specimens strengthened with GFRP and AFRP. Based on typical properties of CFRP, the total force per unit width that the FRP system transfers to the masonry substrate is beyond the limitation given by Equation 2.14. So, this design approach has not been validated for walls strengthened with CFRP. More CFRP strengthened specimens should be tested to generate the experimental data and to compare the accuracy of the existing models presented.

Chapter 3 EXPERIMENTAL PROGRAM

This chapter presents the details of the experimental program that was conducted at the Constructed Facilities Laboratory (CFL) at North Carolina State University (NCSU) in Raleigh, NC. This program includes the construction and testing of wallette specimens and supplementary material tests. In addition, details of the test setup and instrumentation used in this program are given in this chapter.

3.1. Wallette Construction

Nine wallettes were constructed using one and a half two-cell 8-in. thick CMUs per course. Figure 3.1 shows the detailed dimensions of the CMU. The half CMU was cut from full-size CMU using an electric saw prior to wallette construction. According to ASTM C1314-12, the cut location should be at the edge of web so that full-width cross webs can be maintained on each side, as shown in Figure 3.2.

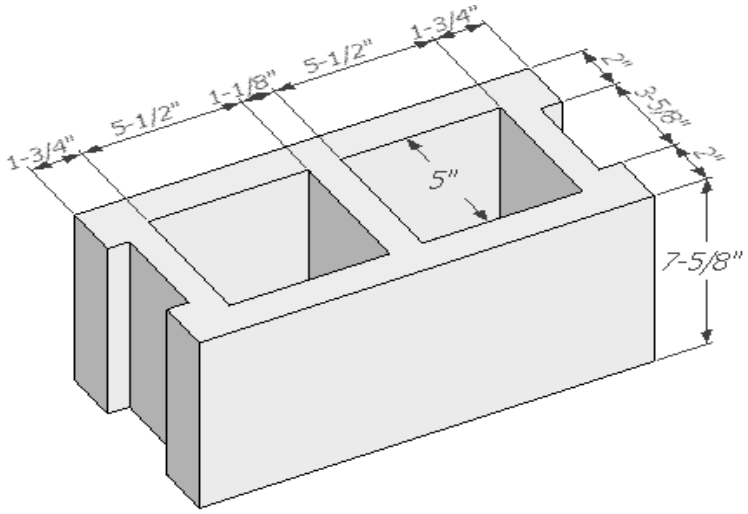

Figure 3.1 - Nominal Dimensions of 8-in. Wide CMU

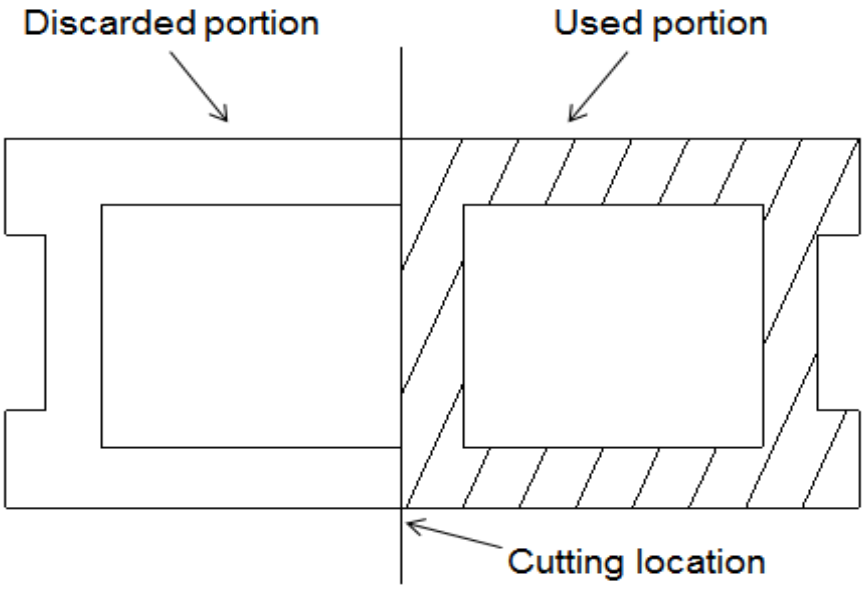

Figure 3.2 - Saw-Cut Location

All the wallettes were constructed by professional brick layers, in a running bond pattern, with nominal overall width and height of 24.5 in. and 80 in., respectively, with a single wythe thickness of 8 in. The mortar and grouted concrete were mixed by the professional masons in the meantime of wallette construction. All of the wallettes were reinforced with a single 0.625 in. diameter (No. 5) Grade 60 steel reinforcing bar over the full height, centrally located within the cross-section in a concrete grouted core. To avoid a premature shear sliding failure during testing, the outside cores of the top and bottom two courses were also filled with concrete. A 0.15 in. diameter (No. 9) gage ladder-type wire joint reinforcement was placed with a vertical spacing of 16 in. in order to control shrinkage. As is typically done in practice, the web of the units in the top course was cut to horizontally locate a 0.5 in. diameter (No. 4) steel reinforcing bar. The details of the wallette construction are shown in Figure 3.3.

(a) Joint Reinforcement

(b) Top Course

(c) Grouting Concrete

(d) Constructed Wallettes

Figure 3.3 - Wallette Construction

3.2. FRP Strengthening Procedure

Eight of the nine steel reinforced CMU wallettes were strengthened with wet lay-up Carbon or Glass externally bonded FRP systems. The following section presents the details of the strengthening procedure of all the strengthened wallettes.

3.2.1. Wallette Surface Preparation

Prior to applying the FRP to the CMU wallettes, several steps had to be taken to prepare the surface of the wallettes and the dry fibers. The wallette surface was prepared according to the manufacturer's instruction to ensure a good bond quality. An electric grinding disc was used to make the wallette surface rough and level. Since the CMU surface is rough enough, only the mortar joints should be grinded to remove any sharp edges and projections. All the dust generated from the grinding was removed using high-pressure air to provide a good bond with the masonry substrate. The surface preparation procedure is shown in Figure 3.4.

(a) Grinding Surface **(b) Removing Dust**

Figure 3.4 - Wallette Surface Preparation

3.2.2. FRP Installation

The dry fibers were cut to the required dimensions in advance. The length of the FRP system should be long enough to exceed the effective length in order to develop the full bond strength. All the FRP used in this program were 60 in. long so that it covered the majority of the wallette height. The ends of the FRP were not clamped by the boundary supports while testing. When cutting the dry fibers, a piece of plastic sheet was used to prevent dust from getting on the fibers, which will also affect the quality of the bond. It should be noted that the fiber at the edge of the fabric was pulled out, in order to get a clean boundary.

The unidirectional FRP systems used in the strengthening system were Velacarb 600U (CFRP) and Velaglass 875 (GFRP), both of which are from EDGE Structural Composites. The glass and carbon fiber sheets are shown in Figure 3.5. Further, the typical material properties of the CFRP and GFRP, as provided by the manufacturer, are summarized in Table 3.1.

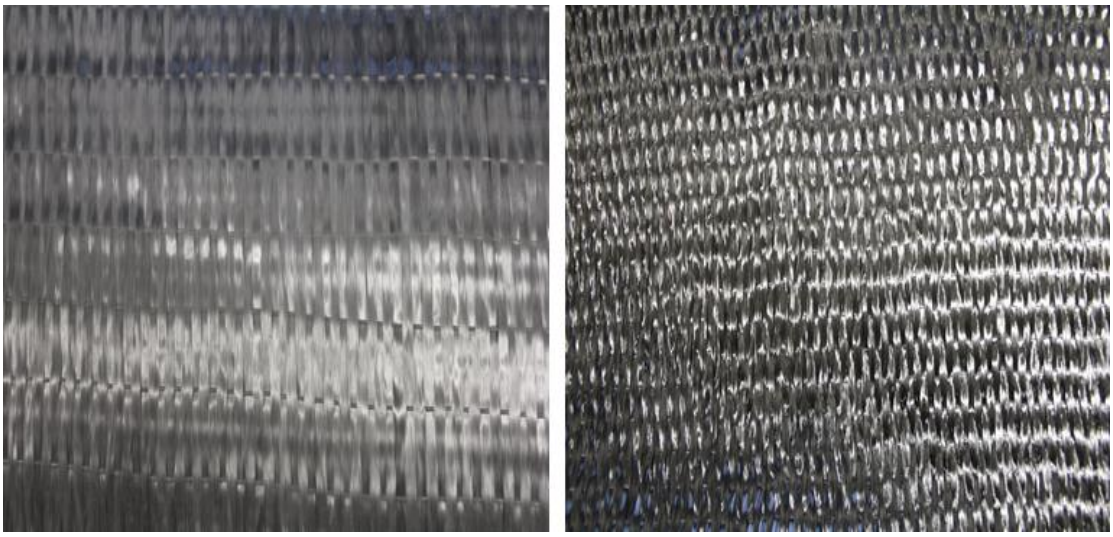

(a) Glass **(b) Carbon**

Figure 3.5 - Fiber Sheets

Table 3.1 - Manufacturer's properties of fibers and laminates

CFRP		GFRP	
Fiber Properties		Fiber Properties	
Areal weight density	17.7 oz/yd^2	Areal weight density	26.0 oz/yd^2
Fabric thickness	0.013 in.	Fabric thickness	0.0136 in.
Tensile strength	650,000 psi	Tensile strength	330,000 psi
Modulus of Elasticity	34 x 10^6 psi	Modulus of Elasticity	10.5 x 10^6 psi
Elongation at Break	1.9%	Elongation at Break	4.0%
Laminate Properties		Laminate Properties	
Average thickness	0.050 in.	Average thickness	0.043 in.
Tensile Strength	140,000 psi	Tensile Strength	80,000 psi
Modulus of Elasticity	10.1 x 10^6 psi	Modulus of Elasticity	4 x 10^6 psi
Elongation at Break	1.2%	Elongation at Break	2.2%
Strength per unit width	7.0 kips/in.	Strength per unit width	3.5 kips/in.

The epoxy used in this experimental program was Veloxx LR, which is a two-component, 100% solids, two-phase epoxy from EDGE Structural Composites. The mix ratio is 100A: 62B by weight in accordance with the manufacturer's instructions. The properties of the epoxy, provided by the manufacturer, are shown in Table 3.2.

Table 3.2 - Manufacturer's property of epoxy

Material	Tensile Strength (psi)	Tensile Modulus (psi)	Elongation at Failure
Veloxx LR	6,500	300,000	5.5%

In a typical wet lay-up strengthening procedure, the pre-cut fabric was saturated by the following steps:

- Mixing epoxy using a mixing drill bit;
- Pouring mixed epoxy on a horizontal surface, which was protected by plastic sheet
- Lay the pre-cut fabric onto the epoxy ;
- Press the fibers down into the epoxy using a plastic putty knife until the epoxy completely penetrates the dry fibers;
- Apply more epoxy to the fibers and spread it evenly until it is fully saturated.

In the meantime, another batch of epoxy was mixed and thickened using TS-720 Cab-o-sil. The saturated fabric was then applied to the wallettes according to the following steps:

- Apply the thickened epoxy to the prepared wallette in order to prime the surface and fill all voids;
- Lay the saturated fabric to the primed surface;
- Align the fabric and remove air bubbles at the interfaces using a roller, until the

fabric is taut and fully attached to the surface;

- Apply additional epoxy onto the saturated fabric surface.

It should be noted that for the wallettes strengthened with two layers of FRP, the second saturated fabric layer was immediately applied directly to the first layer in a similar manner. After strengthening, the wallettes were fully covered using a plastic sheet to protect the FRP from rain and dust during curing. All of the strengthened wallettes were allowed to cure for at least 10 days prior to moving them for testing. Figure 3.6 illustrates the strengthening procedure of a GFRP strengthened wallette. It should be noted that the CFRP system was applied in the same manner.

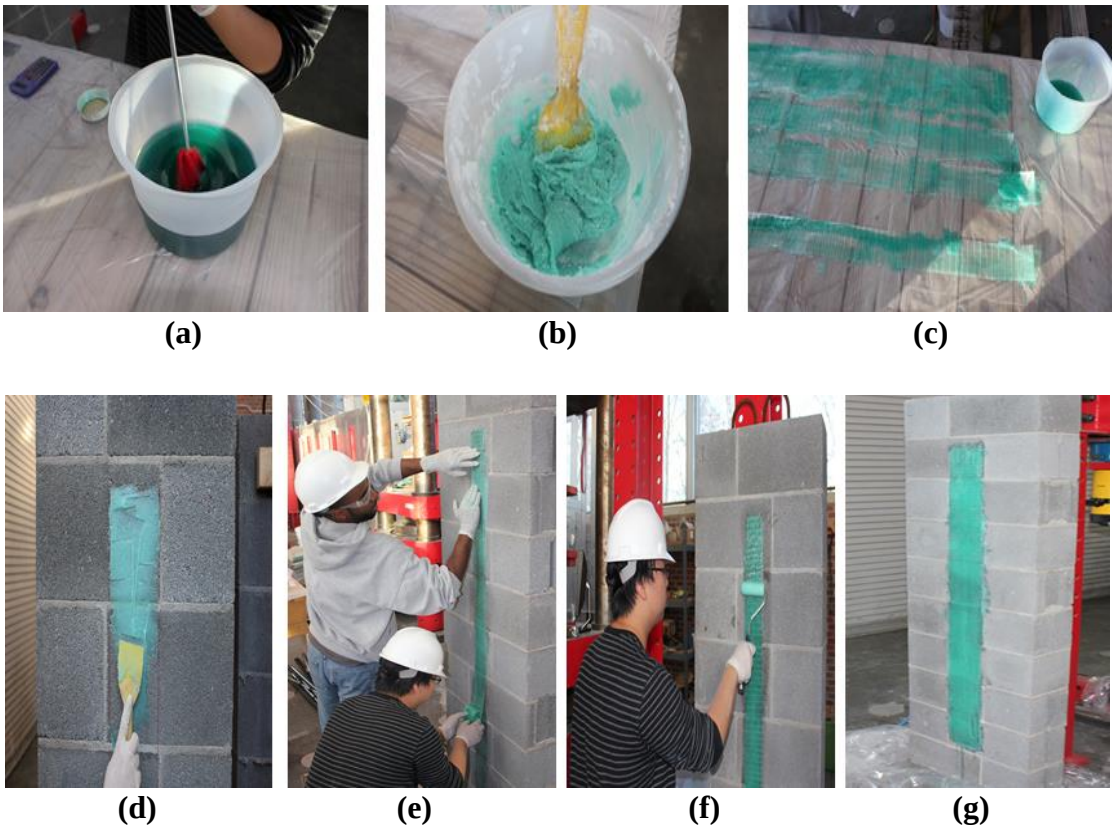

Figure 3.6 - Illustrative Strengthening Procedure: (a) mixing epoxy, (b) thickened epoxy, (c) saturated GFRP, (d) surface priming, (e) GFRP application, (f) alignment of GFRP, (g) strengthened wallette

3.3. Material Tests

Six materials were investigated in this experimental program, including the mortar and grouted concrete, steel reinforcement and FRP composites, CMU prism and the individual CMU. The properties of these materials are very important in calculating the theoretical capacity and the comparison of the test result with existing models. As a result, several supplementary material tests were conducted at the CFL to experimentally define the actual material properties. The test methods and results are given in the following sections.

3.3.1. Material Properties of Grouted Concrete

Eight 4 in. x 8 in. concrete cylinders were cast when the masonry wallettes were constructed. The cylinders were then placed beside the wallettes to be subjected to the same environmental conditions. The concrete cylinders were tested using a 500 kips capacity Forney compressive testing machine at the CFL in accordance with ASTM C39-12a. The load rate was approximately 28 kips/min. Figure 3.7 and Figure 3.8 show the test setup and the typical failure of concrete cylinders, respectively. The measured concrete compressive strengths are shown in Table 3.3.

Figure 3.7 - Compressive Test Setup for Concrete Cylinders

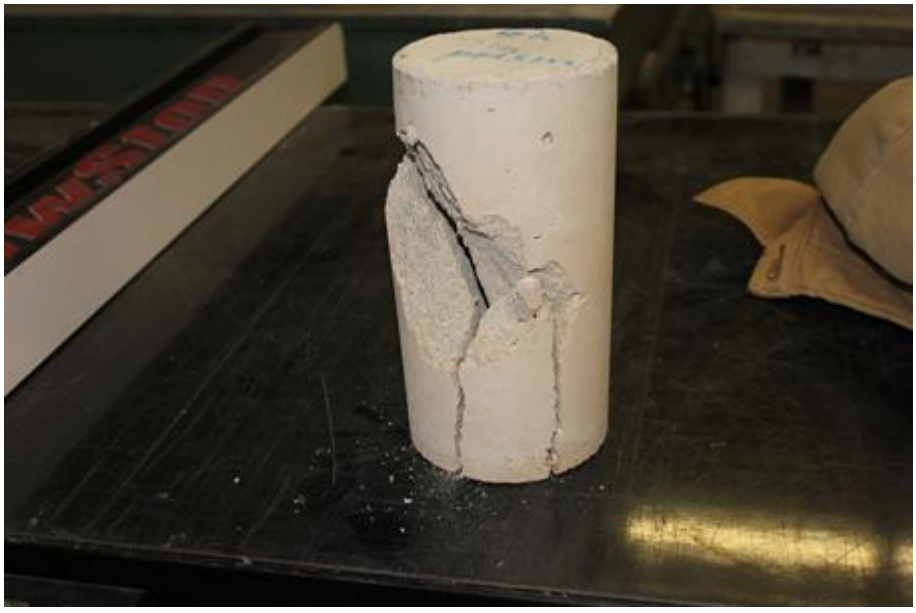

Figure 3.8 - Failed Concrete Cylinders

Table 3.3 - Measured compressive strength of concrete cylinders

Batch Number	Area (in^2)	Compressive Load (lbs)	Compressive Strength (psi)
1	12.57	52500	4180
2	12.57	56900	4530
3	12.57	44300	3520
3	12.57	47300	3770
4	12.57	61700	4920
5	12.57	49200	3920
5	12.57	50400	4010
5	12.57	54900	4370
Average strength			**4150**
Standard deviation			**450**

3.3.2. Tension tests of steel reinforcements

The material properties of steel reinforcement, such as the yield strain and stress, play a critical role in calculating the flexural capacity of both strengthened and unstrengthened wallettes. In order to define these properties, as well as the stress-strain relationship of the steel reinforcement, tension tests were conducted on the No. 5 bars in accordance to ASTM A370-12a. Three 20 in. long steel bars were tested using a 220 kips servo-hydraulic universal testing machine at the CFL. During testing, an MTS extensometer was attached to the bar, with a gauge length of 2 in., to measure the strain. The load was recorded directly by the testing machine. The test data can be seen in Table 3.4. The test setup and failed steel bars

are shown in Figure 3.9 and 3.10, respectively. For illustrative purpose, Figure 3.11 gives the stress-strain relationship of the bars.

Table 3.4 - Measured tensile strength of steel reinforcement

Specimen Number	Yield Strain (με)	Yield Stress (ksi)	Elastic Modulus (ksi)
1	2444	66.6	27300
2	2608	66.0	25300
3	2377	66.1	27800
Average	**2476**	**66.2**	**26800**

Figure 3.9 - Tension Test Setup for Steel Reinforcement

Figure 3.10 - Ruptured Steel Reinforcing Bars

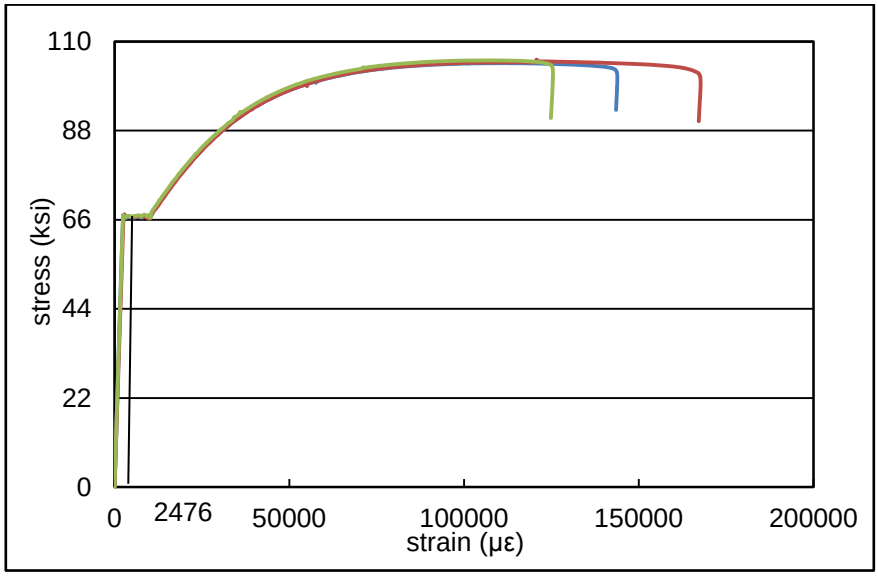

Figure 3.11 - Stress-Strain Relationship of Steel Reinforcement

3.3.3. Tension tests of FRP composites

The existing FRP debonding strain models require the tensile properties of the FRP composites, such as the ultimate tensile strength and rupture strain. In order to experimentally define these tensile properties, several coupon tests were conducted on both the CFRP and GFRP composites at the CFL.

Four 1 ft. x 1 ft. witness panels were constructed, on a clean plastic plate, for both one-layer and two-layers of the CFRP and GFRP composites. The fabric was previously cut to the desired size and the epoxy was prepared as described previously. Before pouring the epoxy onto the plastic plate, the plate surface was coated with a layer of paste finishing wax to prevent the FRP composites from bonding to the plate. The fabric was fully saturated as described for the wallette strengthening procedure. A plastic putty knife and a roller were used to align the fibers and remove extra epoxy. The plastic putty knife should be moved in the direction of fiber, in order to make the fiber taut and flat. The witness panels were then stored in the lab at room temperature. After 3 days, the witness panels were removed from the plastic using a metal trowel. Figure 3.12 shows the cured witness panels.

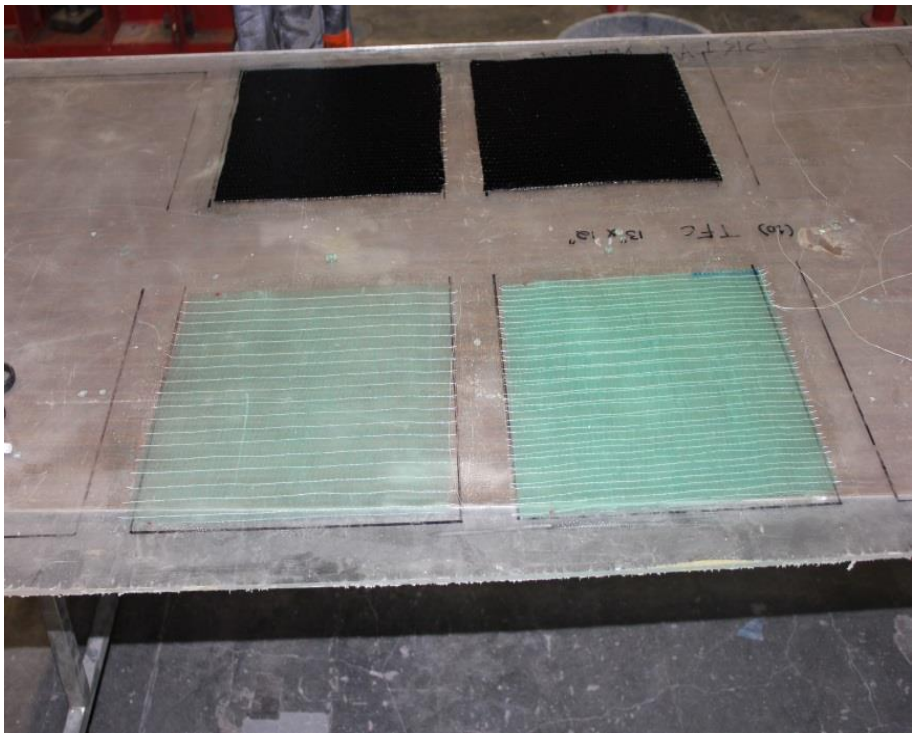

Figure 3.12 - Cured Witness Panels

After 7 days, when the epoxy was fully cured, the witness panels were cut using an electric bandsaw into 1 in. wide coupons for the tensile tests. According to ASTM D3039-08, 3 in. long and 0.25 in. thick aluminum tabs were used for gripping the ends. The edges of the tabs were grinded, using a steel brush, to prevent the tabs from cutting the FRP coupons while gripping. The surface of the FRP coupons and aluminum tabs were sanded using sandpaper and a dry sand blast machine, respectively, in order to ensure a good bond quality between the tabs and FRP composites.

A 15 kips servo mechanical universal test frame testing machine was used to perform the coupon tests. A 2 in. MTS extensometer was placed at the center of the coupon during testing to record the strain. The load was controlled by the speed of the cross-head. According to ASTM D3039-08, the cross-head was moved at a constant displacement rate of 0.05 in./min. Figures 3.13 and 3.14 show the CFRP coupon test setup and the ruptured coupons, respectively.

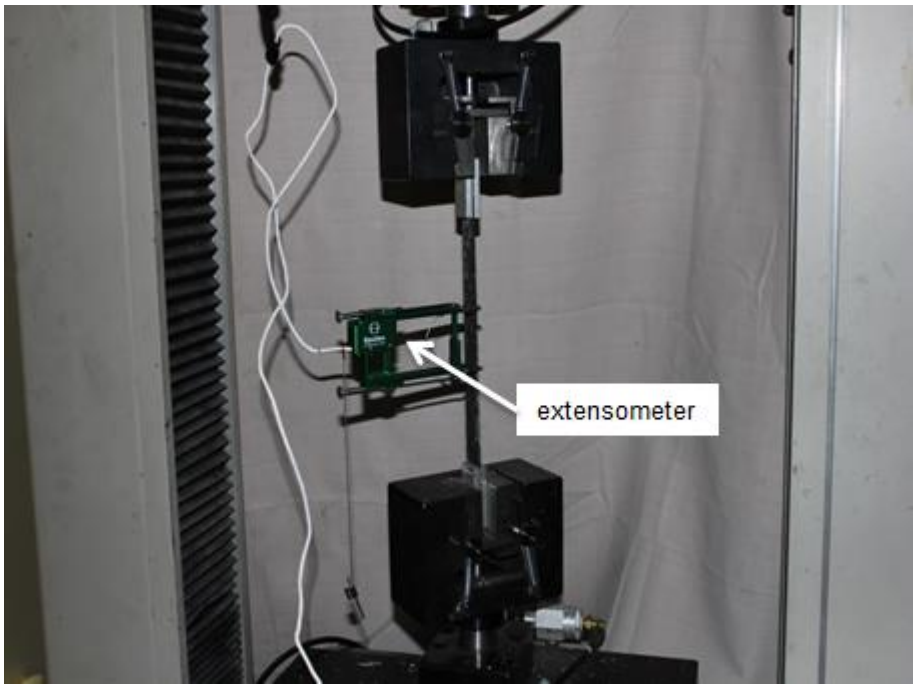

Figure 3.13 - FRP Coupon Test Setup

(a) One-layer Coupons **(b) Two-layers Coupons**

Figure 3.14 - Ruptured CFRP Coupons

The test results of the one-layer and two-layer CFRP coupons are summarized in Table 3.5 and Table 3.6, respectively. The width and thickness of each CFRP coupon were measured using a Westward digital caliper with a minimum scale of 0.00005 in. It should be noted that the elastic modulus in Tables 3.5 and 3.6 is the chord modulus calculated within the strain range from 1000 με to 3000 με, in accordance with ASTM D3039-08. In addition, the axial stress-strain relationships of one-layer and two-layer CFRP coupons are shown in Figure 3.15 and Figure 3.16, respectively.

Table 3.5 - Result of one-layer CFRP coupon tests

Coupon ID	Area (in^2)	Rupture Load (lb.)	Tensile Strength (ksi)	Rupture Strain ($\mu\varepsilon$)	Elastic Modulus (ksi)
1L-CFRP-1	0.032	5409	167	15880	11060
1L-CFRP-2	0.032	5933	184	14170	14280
1L-CFRP-3	0.033	5385	166	13420	13440
1L-CFRP-4	0.032	6881	215	17660	11490
1L-CFRP-5	0.032	6421	198	16270	12560
1L-CFRP-6	0.033	6219	191	14990	11450
AVERAGE	**0.032**	**6099**	**187**	**15400**	**12380**
S.D.	**0.0005**	**587**	**19**	**1530**	**1280**

Table 3.6 - Result of two-layer CFRP coupon tests

Coupon ID	Area (in^2)	Rupture Load (lb.)	Tensile Strength (ksi)	Rupture Strain ($\mu\varepsilon$)	Elastic Modulus (ksi)
2L-CFRP-1	0.0539	13322	247	16080	14490
2L-CFRP-2	0.0536	11172	208	14190	14310
2L-CFRP-3	0.0546	12615	231	14430	15020
2L-CFRP-4	0.0544	12207	224	14570	14600
2L-CFRP-5	0.0529	13928	263	16700	15260
2L-CFRP-6	0.0537	10187	190	12640	14170
2L-CFRP-7	0.0541	11430	211	13490	14340
AVERAGE	**0.0539**	**12123**	**225**	**14590**	**14600**
S.D.	**0.0006**	**1296**	**25**	**1400**	**400**

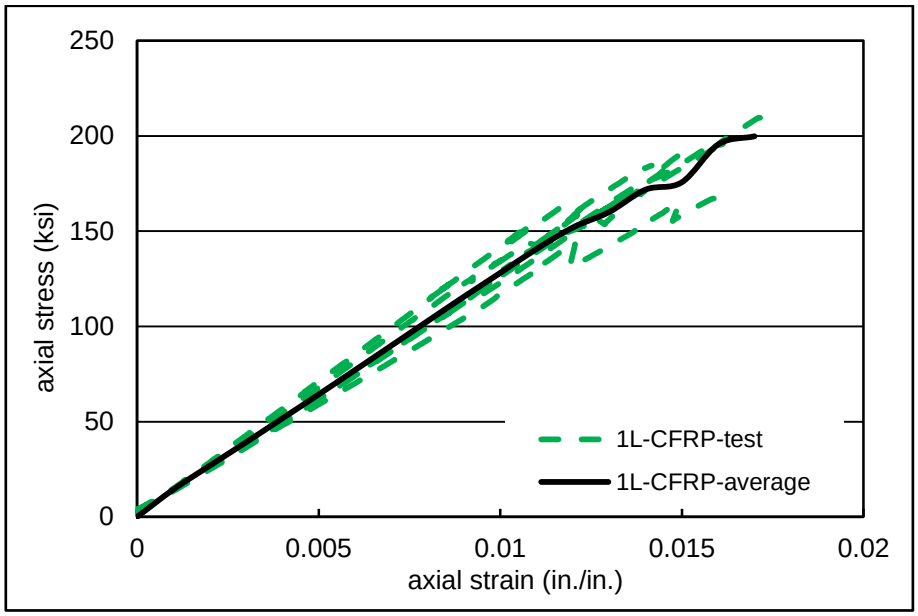

Figure 3.15 - Axial Stress-Strain Curves of 1-layer CFRP Coupons

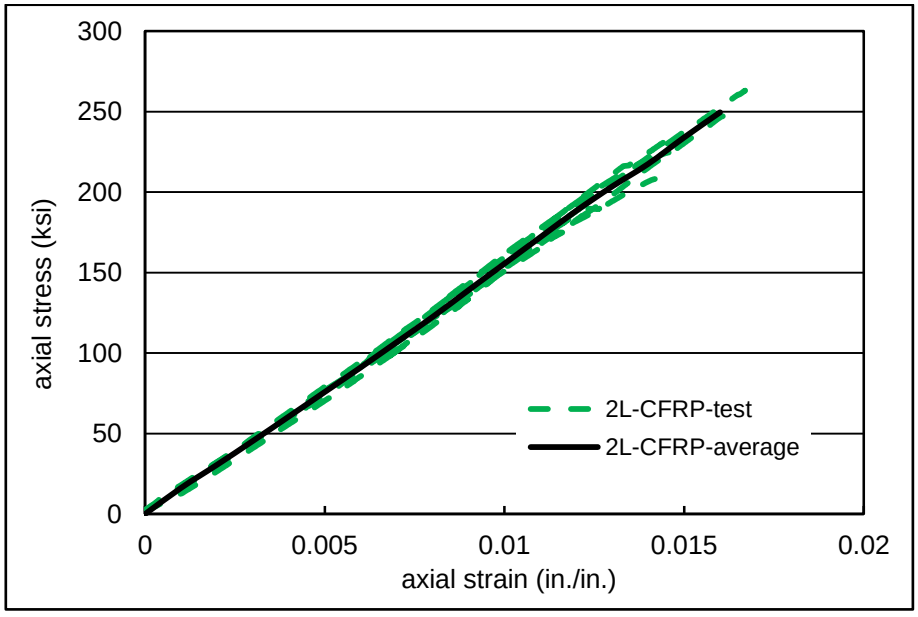

Figure 3.16 - Axial Stress-Strain Curves of 2-layer CFRP Coupons

The GFRP coupons were tested in the same way as the CFRP coupons. Contrary to the CFRP which had a flat surface, the GFRP had a wavy surface. For the one-layer GFRP coupons, the thickness varied between 0.04 in. and 0.02 in. for the thick and thin regions, respectively. As a result, it is hard to use digital calipers, whose measuring surface is flat, to measure the nominal thickness of the GFRP coupons. The cross-sectional area of the GFRP coupons was then measured using a water displacement method. GFRP coupons were immersed into water. By measuring the volume change of water and the length of the coupon immersed in the water, the cross-sectional area of GFRP coupons can be calculated. The width of GFRP coupons were measured using the Westward digital calipers. The nominal thickness of the GFRP coupon can then be computed. The tensile test setup of the GFRP coupons is the same as that of the CFRP coupons. Figure 3.17 shows the failed GFRP coupon specimens. The test results of the one-layer and two-layer GFRP coupons are summarized in Table 3.7 and Table 3.8, respectively. The elastic modulus shown in Table 3.7 and 3.8 is the chord modulus calculated within the strain range from 1000 με to 3000 με, in accordance with ASTM D3039-08. In addition, the axial stress-strain relationships of one-layer and two-layer GFRP coupons are shown in Figure 3.18 and Figure 3.19, respectively.

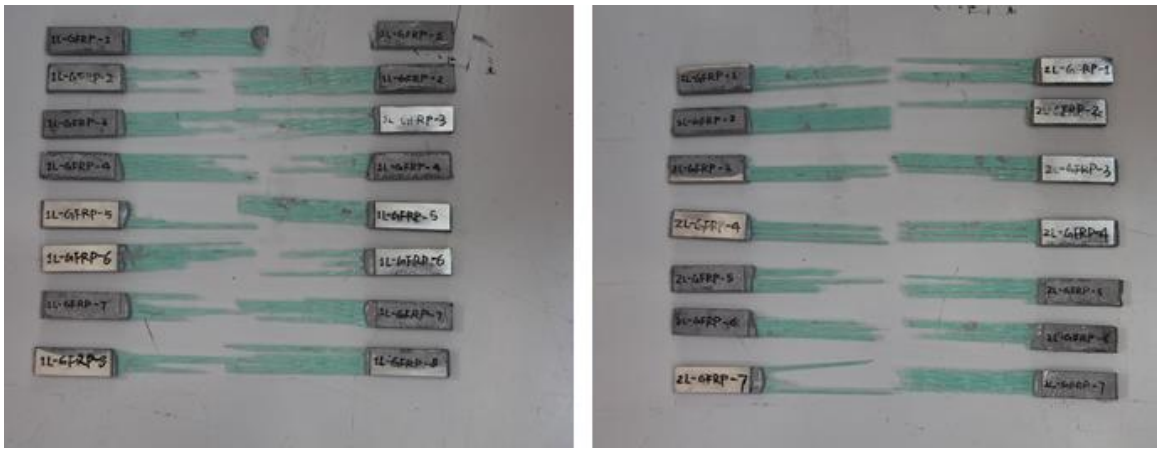

(a) One-layer GFRP Coupons **(b) Two-layers GFRP Coupons**

Figure 3.17 - Ruptured GFRP Coupons

Table 3.7 - Result of one-layer GFRP coupon tests

Coupon ID	Area (in^2)	Rupture Load (lb.)	Tensile Strength (ksi)	Rupture Strain (με)	Elastic Modulus (ksi)
1L-GFRP-1	0.0330	1572	48	19540	2440
1L-GFRP-2	0.0337	1527	45	19650	2280
1L-GFRP-3	0.0326	1537	47	19240	2450
1L-GFRP-4	0.0323	1528	47	20380	2360
1L-GFRP-5	0.0323	1333	41	17030	2400
1L-GFRP-6	0.0328	1667	51	21550	2460
1L-GFRP-7	0.0325	1430	44	18650	2540
1L-GFRP-8	0.0328	1542	47	19650	2460
AVERAGE	**0.0328**	**1517**	**46**	**19460**	**2420**
S.D.	**0.0005**	**99**	**3**	**1300**	**80**

Table 3.8 - Result of two-layer GFRP coupon tests

Coupon ID	Area (in^2)	Rupture Load (lb.)	Tensile Strength (ksi)	Rupture Strain ($\mu\varepsilon$)	Elastic Modulus (ksi)
2L-GFRP-1	0.0559	2826	51	19210	2700
2L-GFRP-2	0.0557	2828	51	19890	2830
2L-GFRP-3	0.0558	2998	54	20340	2720
2L-GFRP-4	0.0556	2629	47	18420	2510
2L-GFRP-5	0.0555	2813	51	19550	2520
2L-GFRP-6	0.0560	3386	60	23570	2710
2L-GFRP-7	0.0560	2885	52	20640	2592
AVERAGE	**0.0558**	**2909**	**52**	**20230**	**2650**
S.D.	**0.0002**	**237**	**4**	**1640**	**120**

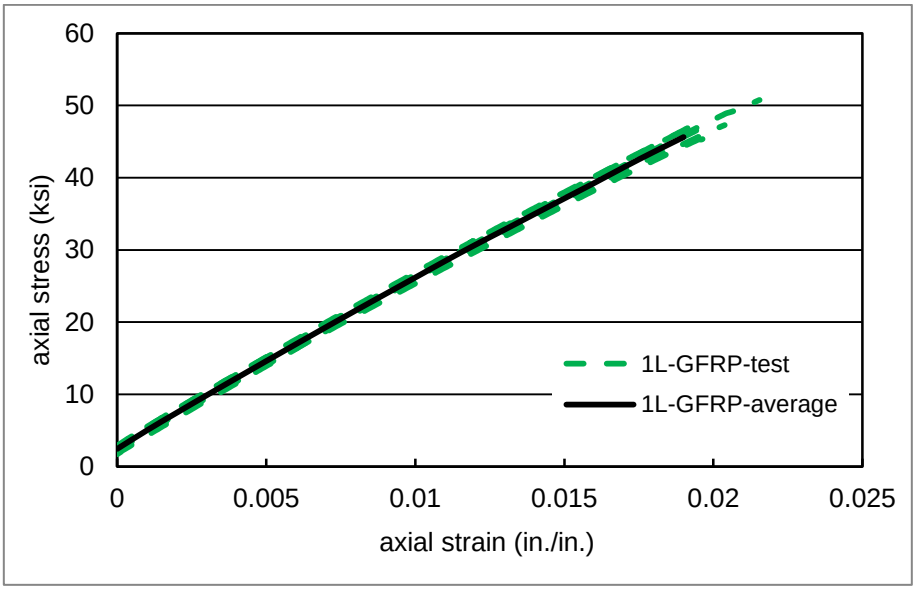

Figure 3.18 - Axial Stress-Strain Curves of 1-layer GFRP Coupons

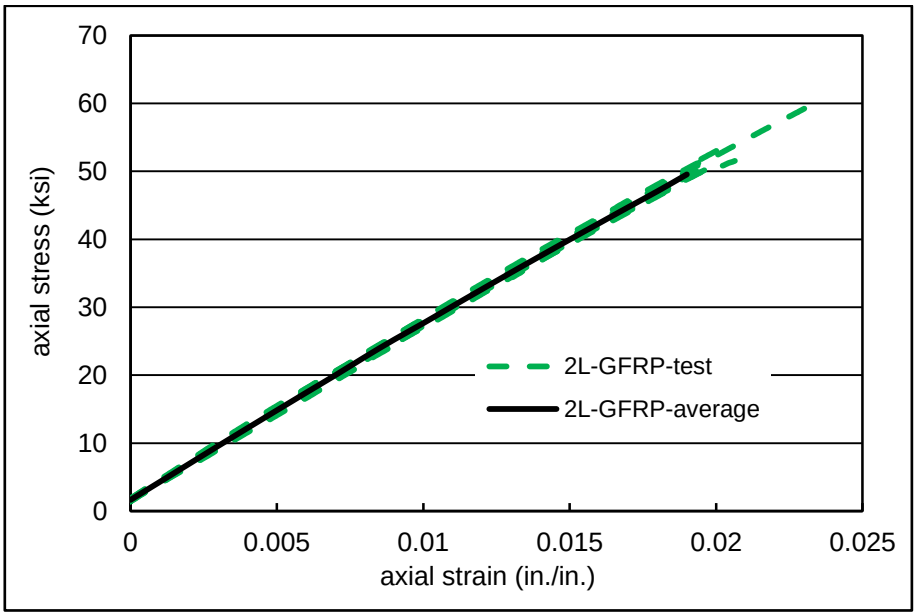

Figure 3.19 - Axial Stress-Strain Curves of 2-layer GFRP Coupons

3.3.4. Compressive tests of mortar cubes

For quality assurance, three 2-in. mortar cubes were sampled for each batch of mortar used during the construction of the wallettes. The mortar was tamped by hand and field cured beside the wallettes to be subjected to the same environmental conditions. The mortar cubes were later tested using a 500 kips capacity Forney compressive testing machine at the CFL. In accordance with ASTM C109-12, the load was applied at a load rate of 15 kips/min. Figure 3.20 shows the test setup. In addition, the measured mortar compressive strengths are shown in Table 3.9.

Figure 3.20 - Compressive Test Setup for Mortar Cubes

Table 3.9 - Measured compressive strength of mortar cubes

Area (in^2)	Compressive Load (kips)	Compressive Strength (ksi)
Mortar used in 1st – 3rd courses		
4	14.2	3.6
4	14.0	3.5
4	16.3	4.1
Average	**14.8**	**3.7**
S.D.	**1.3**	**0.3**
Mortar used in 4th – 6th courses		
4	12.5	3.1
4	14.2	3.6
4	11.9	3.0
Average	**12.9**	**3.2**
S.D.	**1.2**	**0.3**

Table 3.9 – Measured compressive strength of mortar cubes (continued)

Mortar used in 7th – 9th courses		
4	11.5	2.9
4	11.2	2.8
4	11.0	3.0
Average	**11.3**	**2.9**
S.D.	**0.3**	**0.1**

3.3.5. Compressive tests of CMU prisms

Four two-course masonry prisms, with nominal dimensions 16 in. x 16 in. x 8 in., were constructed with full mortar beds at the same time as the wallettes. The prisms were field cured beside the wallettes to be subjected to the same environmental conditions. Two of the prisms were fully grouted with the concrete used in the wallette construction, and the other two prisms were ungrouted. The prisms were later tested by a 2000 kips capacity servo-hydraulic press testing machine, in accordance with ASTM C1314-12, to determine the experimental compressive strength of the masonry, f'_m. Before placing the prisms in the testing machine, the prisms were capped with gypsum cement and steel plates to provide a flat surface on the top and bottom. The capping procedure was according to ASTM C1552-12. The prism test setup and failed prism are shown in Figure 3.21 and 3.22, respectively. And the measured compressive strength is summarized in Table 3.10.

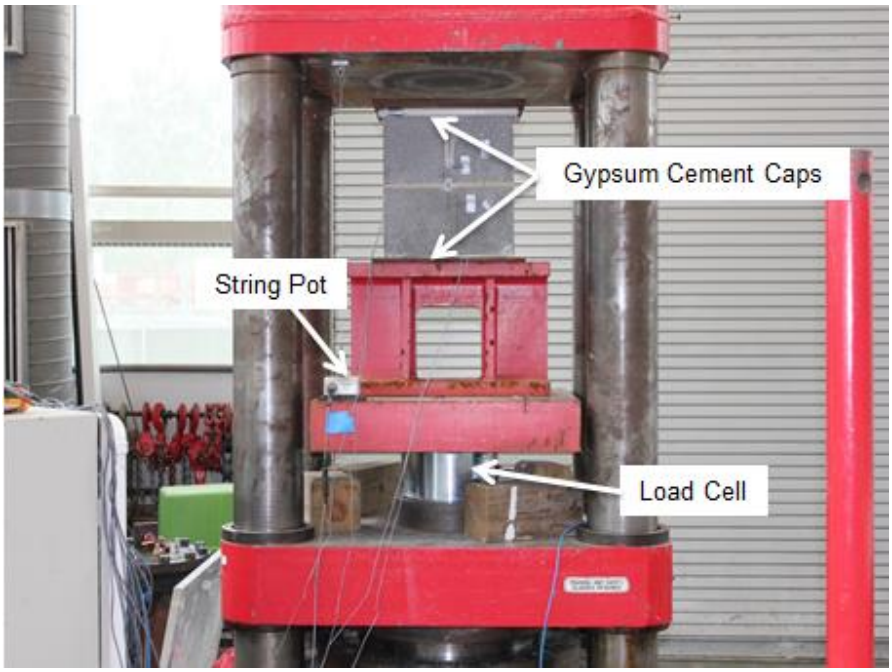

Figure 3.21 - Compressive Test Setup for CMU Prism

Figure 3.22 - Failed CMU Prism

It should be noted that the net cross-sectional area was used as the area of the ungrouted masonry prisms, and the gross cross-sectional area was used for the grouted masonry prisms. In accordance with ASTM C1314-12, the specified compressive strength, f'_m, was modified by the height to thickness correction factor which is determined by linear interpolation between the given values in Table 3.11.

Table 3.10 - Masonry prism compressive strength

Specimen Series	Area (in^2)	Maximum Load (kips.)	Correction Factor	Compressive Strength (ksi)	**Average (ksi)**
Grouted-1	116	303.6	1.004	2.62	**2.51**
Grouted-2	113	269.4	1.005	2.40	
Ungrouted-1	62.04	88.9	1.004	1.44	**1.39**
Ungrouted-2	62.04	83.1	1.004	1.34	

Table 3.11 - Height to thickness correction factor for masonry prism (ASTM C1314-12)

h_p/t_p	1.3	1.5	2.0	2.5	3.0	4.0	5.0
Correction Factor	0.75	0.86	1.0	1.04	1.07	1.15	1.22

For illustrative purposes, the compressive stress-strain curves of each CMU prism is shown in Figure 3.23. It should be noted that the testing machine crosshead displacement was measured by a string pot. The string pot started recording when the crosshead and the prism are fully contacted, with a frequency of 2 Hz. The strain shown in Figure 3.23 is calculated using the measured displacement by the string pot.

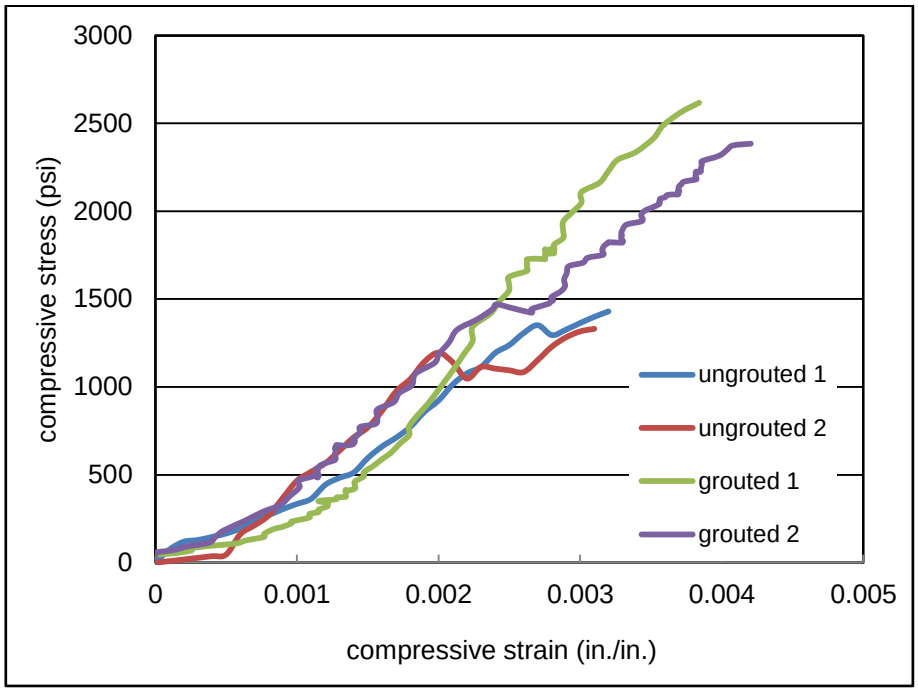

Figure 3.23 - Compressive Stress-Strain Curves of CMU Prisms

3.3.6. Compressive tests of individual CMU

Compressive tests of individual CMU were conducted using the 220 kips servo-hydraulic universal testing machine according to ASTM C140-13a. Since the length of the CMU is larger than the diameter of the crosshead plate, two 2 in. thick steel plates were used for capping, in order to transfer the compressive load. As the masonry surface was level, no gypsum cement was used in this test. The top steel plate was tied to the crosshead using belt straps to protect the MTS machine when failure occurred. Before starting each test, the top plate was put in full contact with the masonry. The load and displacement of the crosshead was measured directly by the MTS machine. Figure 3.24 and Figure 3.25 show the compressive test setup and the failed masonry unit, respectively. The test results are summarized in Table 3.12.

Table 3.12 - Measured compressive strength of individual CMU

Specimen Series	Area (in^2)	Maximum Load (kips)	Maximum Deflection (in.)	Compressive Strength (ksi)
CMU-1	62.04	117.9	0.109	1.90
CMU-2	62.04	117.6	0.101	1.90
CMU-3	64.76	146.3	0.114	2.26
CMU-4	62.04	126.1	0.149	2.03
Average	**62.72**	**127.0**	**0.118**	**2.02**
S.D.	**1.36**	**13.5**	**0.021**	**0.17**

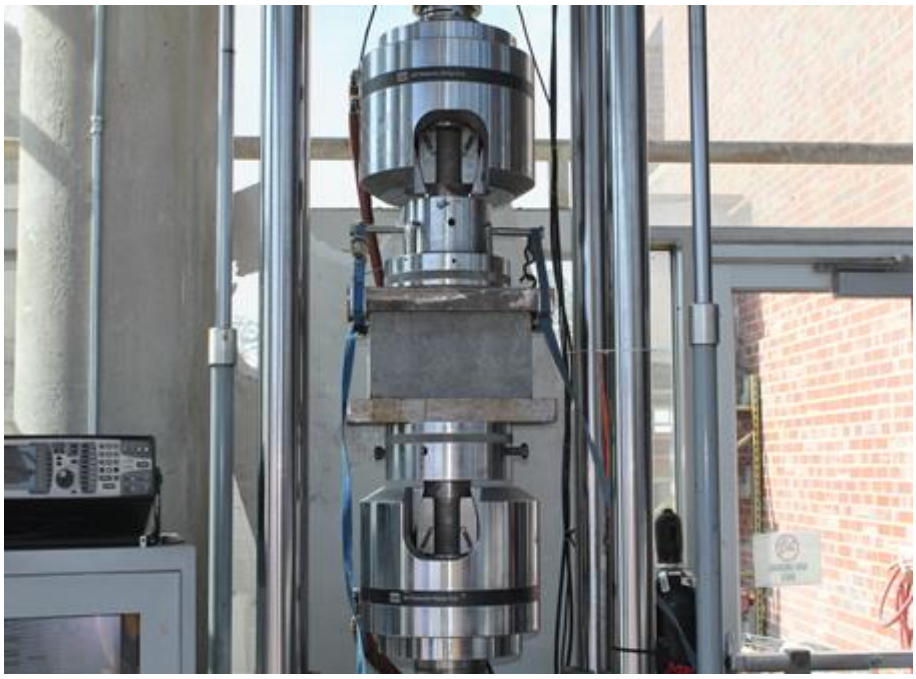

Figure 3.24 - Compressive Test Setup for Individual CMU

Figure 3.25 - Failed Individual CMU

3.4. Wallette Experimental Matrix

The experimental program consists of nine steel reinforced CMU wallettes, one of which serves as an unstrengthened control, while the other eight are strengthened with wet lay-up Carbon or Glass EB-FRP systems. For reference, the strengthened wallettes are designated with two letters followed by a number. The first letter represents the type of FRP: “C” for CFRP; and “G” for GFRP. The second letter represents the number of FRP layers: “S” for single layer; and “D” for double layers. The number represents the width of the FRP laminate in inches. Thus, CS6 represents a wallette strengthened with one layer of 6 in. wide CFRP. It should be noted that the wallette strengthened with one layer of 3 in. wide GFRP, GS3, was repeated, so these two wallettes are designated as GS3-1 and GS3-2. These characteristics of the wallettes are given in Table 3.13.

Table 3.13 - Test matrix of the wallette experimental program

Wallette ID	FRP system	Number of layers	FRP width (in.)
Control	N.A.	N.A.	N.A.
CS3	CFRP	Single	3
CS6	CFRP	Single	6
CS8	CFRP	Single	8
CD3	CFRP	Double	3
GS3-1	GFRP	Single	3
GS3-2	GFRP	Single	3
GS6	GFRP	Single	6
GD3	GFRP	Double	3

3.5. Wallette Test Setup

All the wallettes were simply supported over a vertical span of 66 in. and tested in three-point out-of-plane bending. Two 6 in. x 6 in. steel tubes were fixed to the strong reaction wall by steel tension bars, vertically spaced 72 in. on center, to provide the boundary supports. The FRP was 60 in. long so that the ends were not clamped by the supports. The bottom steel tension bars were supported by wood blocks and the top steel tension bars were tied to the reaction wall by lifting belts, in order to prevent the steel bars from bending due to the self-weight of boundary steel tubes. A 60 kips capacity hydraulic jack was located horizontally at the mid-height of the wallettes to apply the concentrated load, which was increased

monotonically to failure. A 4 in. x 4 in. steel tube was placed between the hydraulic jack and the wallette to distribute the load over the full width. A piece of 0.25 in. thick rubber sheet was inserted at all of the interfaces between the steel tubes and the wallette to evenly distribute the load along the full width of the wallette and minimize any stress concentration due to unevenness of the wallette surface. In addition, a steel roller was used at the bottom of the wallette specimen so that it may rotate freely during testing while providing the necessary vertical reactive force. The whole wallette system was supported by a 15 in. high concrete block to align with the holes in the reaction wall. Figure 3.26 shows a schematic of the test setup.

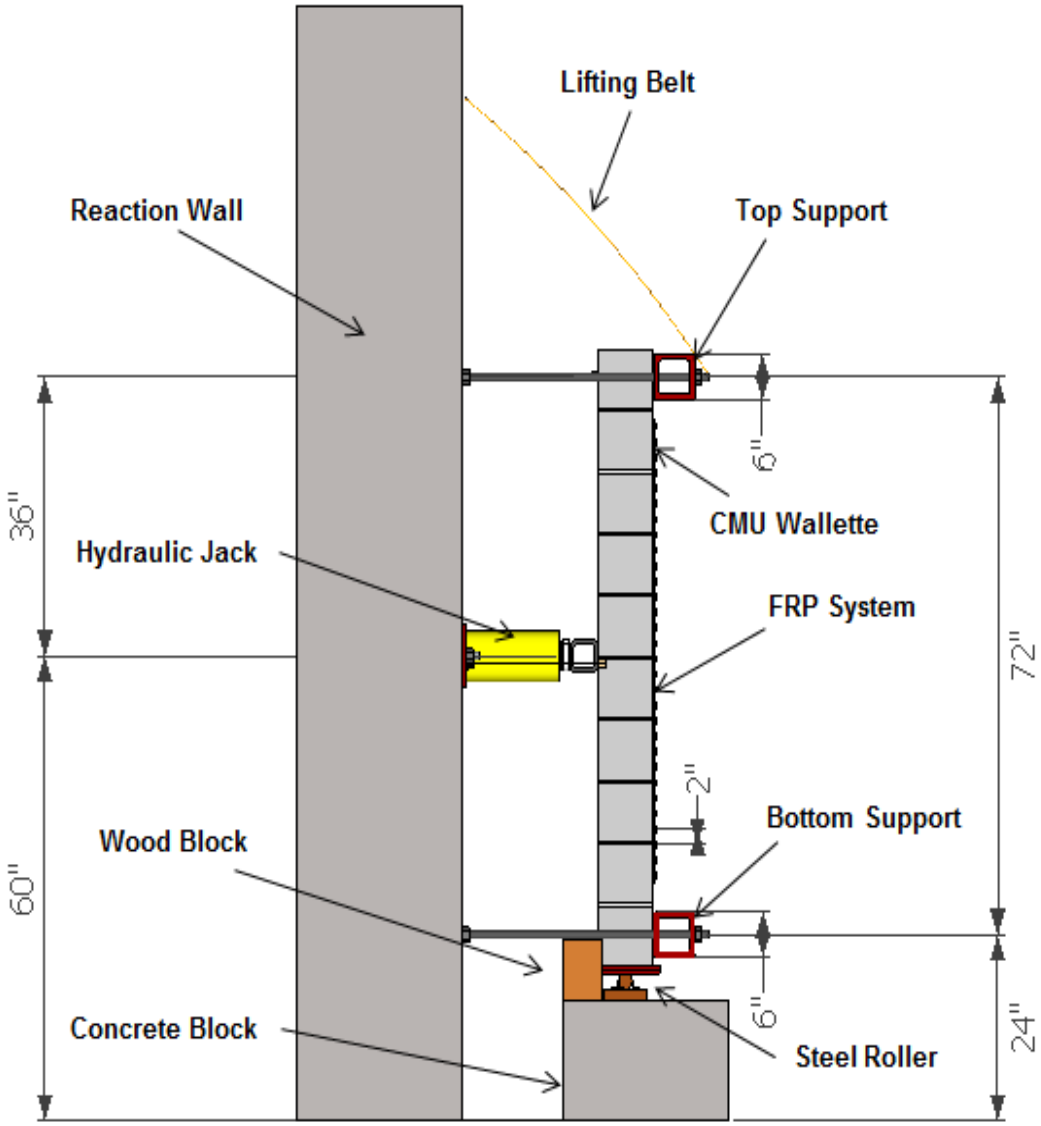

Figure 3.26 - Schematic of Wallette Test Setup

3.6. Instrumentation

A 25 kips capacity load cell was attached to the hydraulic jack to record the concentrated load continuously during testing. Two 15 in. capacity string pots were located at mid-height at both vertical edges of the wallette to measure the maximum out-of-plane displacement. A 2 in. capacity string pot was also located at each top and bottom support to monitor the displacement of the supports due to the elongation of steel bars, so that the rigid body movement of the wallette may be subtracted from the measured mid-height displacement. Since the out-of-plane displacement at the boundary supports is much smaller than that at mid-height, the string pots used at boundary have a smaller displacement capacity to ensure accurate data is collected. The load cell and string pots were used in the same location for all CMU wallettes, including the strengthened wallettes and the control wallette. Details of the location of these instrumentations are shown in Figure 3.27.

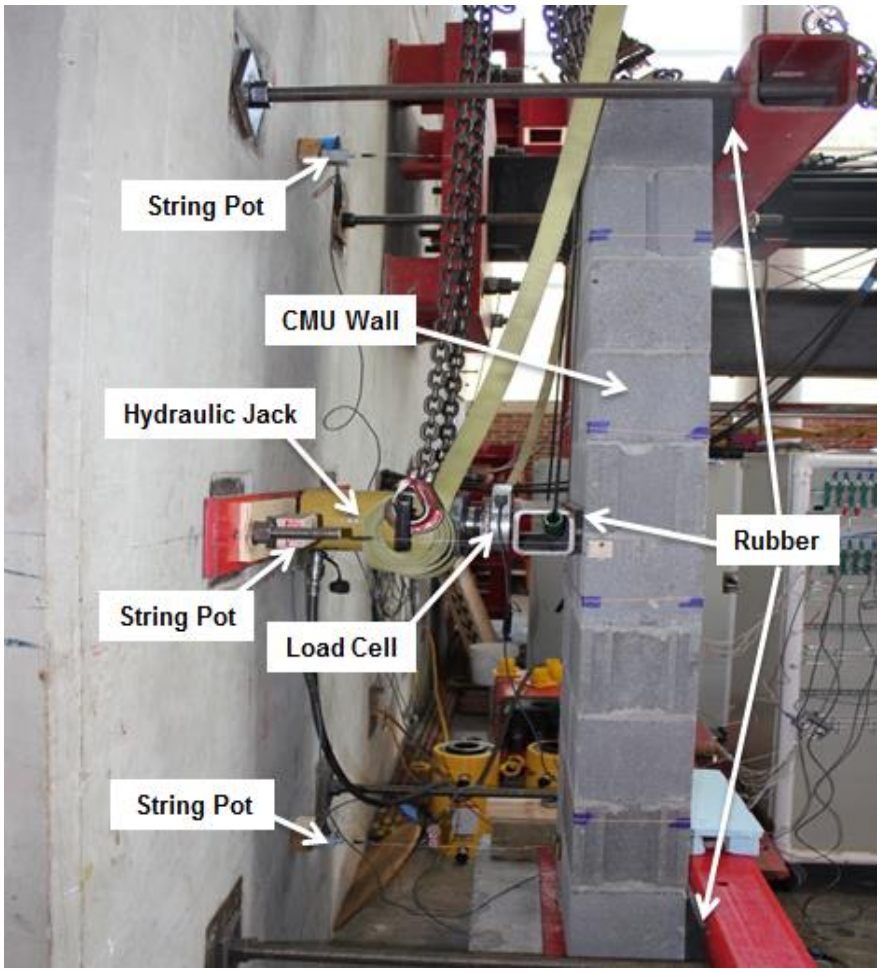

Figure 3.27 - Over View of Test Instrumentation

An advanced non-contact 3D position measurement system, OPTOTRAK Certus HD Dynamic Measuring Machine (DMM), was used to measure both FRP strain and out-of-plane displacement distribution along the wallette. In addition, a 0.25 in. long linear electrical resistance strain gage was bonded vertically on the surface of the FRP laminate at the mid-height bed joint, the position of the maximum bending moment, to validate the data recorded from the OPTOTRAK system. Figure 3.28 shows the setup of the OPTOTRAK system prior to testing. As illustrated in Figure 3.28, 30 LED targets were located uniformly along the height of the FRP composite with a center-to-center spacing (gage length) of 2 in. The OPTOTRAK camera tracks the LED targets during testing and records 3D position data from each LED target. The continuous out-of-plane displacement along the whole height of each CMU wallette and the FRP tension strain distribution along the length of FRP laminate can then be calculated using the position data. A Vishay System 5000 data acquisition system was used to record test data of the load cell, string pots and strain gage. The 3D OPTOTRAK position data was recorded by NDI computer software. Both data acquisition machines started recording at the same time, with the same frequency of 2 Hz during the whole testing period.

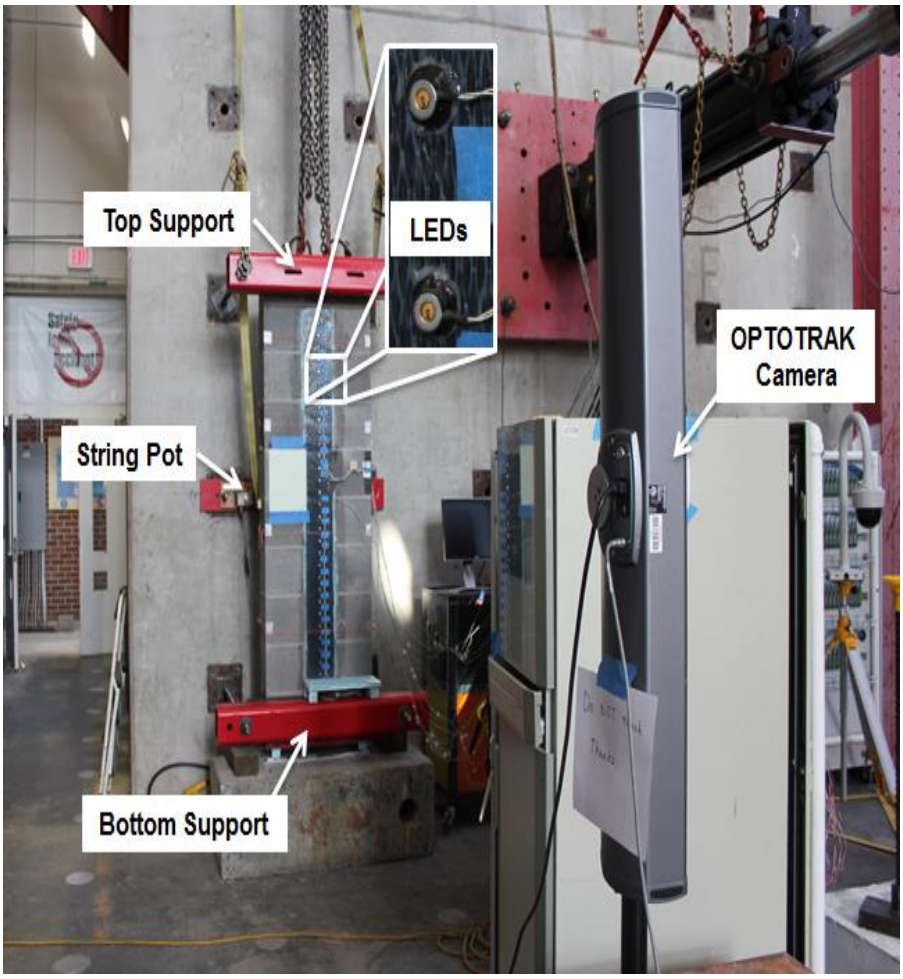

Figure 3.28 - Overview of OPTOTRAK System Setup

Chapter 4 EXPERIMENTAL RESULT

This chapter presents the test results of all nine steel reinforced CMU wallettes, including both strengthened and unstrengthened specimens. The FRP tension strain was measured by both a linear strain gage and the OPTOTRAK system. The continuous FRP strain distributions are those given by the OPTOTRAK system. The mid-height displacement was measured by string pots and the OPTOTRAK system. Both systems started recording data at the same time, with the same frequency of 2 Hz during the test. The failure mode of each specimen is briefly described, and the load-deflection and strain distribution at different load levels are also given in this chapter.

4.1. Control Wallette

The control wallette failed in a ductile tension controlled flexural mode and the test was stopped prior to complete collapse. The compression zone crushed and a significant horizontal flexural crack was observed at the mid-height joint. The majority of the cracks were located at the mortar joints in the middle zone of the wallette. Some vertical splitting cracks were also observed on the front tension surface due to the internal steel reinforcement. No cracks were observed at the area near supports. Figure 4.1 shows the front and profile views at failure. Figure 4.2 shows the crushed CMU on compression side at failure.

(a) Front View **(b) Profile View**

Figure 4.1 - Control Wallette at Failure

Figure 4.2 - Crushed CMU at Compression Face of Control Wallette at Failure

The maximum applied load was 4.5 kips with a corresponding mid-height out-of-plane displacement of 2.82 in. It should be noted that neither strain gage nor OPTOTRAK system was used in the control testing. The load – mid-height deflection curve is shown in Figure 4.3. The rigid body movement of the wallette was subtracted from the measured out-of-plane displacement. It should also be noted that the part of curve after maximum load is not shown in Figure 4.3.

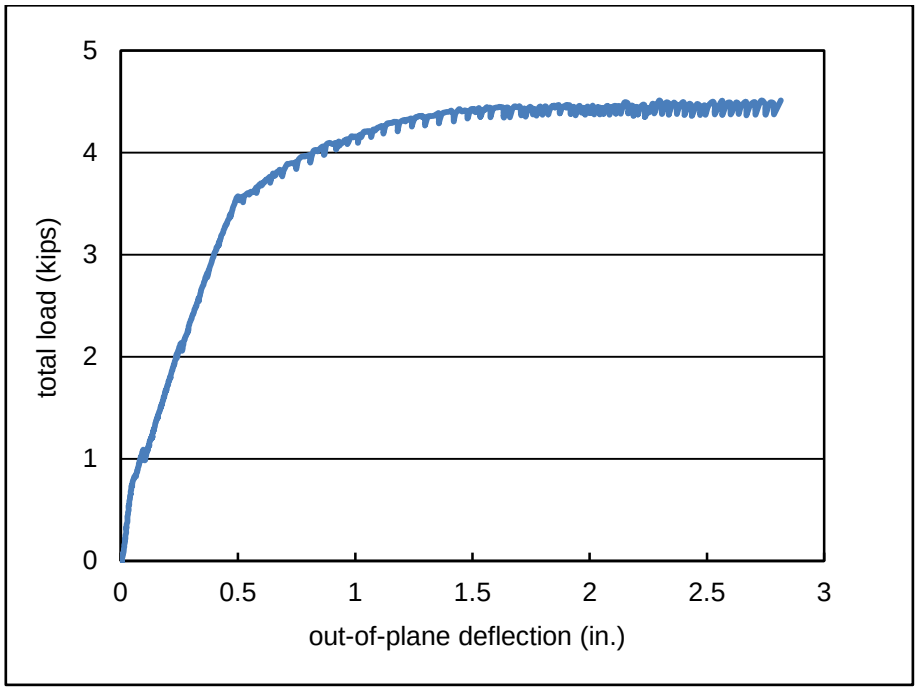

Figure 4.3 - Load – Mid-height Deflection Curve of Control Wallette

4.2. CFRP Strengthened Wallettes

All the CFRP strengthened wallettes failed by IC debonding. The detailed failure mode of each CFRP strengthened wallette is described in this section.

4.2.1. Wallette CS3

Wallette CS3 was strengthened by a 3 in. wide single layer of CFRP, which failed by IC debonding. Debonding started at the mid-height and then propagated rapidly to the bottom of the wallette. The widest horizontal crack occurred at the 5^{th} mortar joint (mid-height). It should be noted that the mortar joints were numbered from the bottom to top. And the numbering method is consistent in the rest of this chapter. A thin layer of masonry remained attached to the CFRP laminate. Diagonal cracks on the wallette surface propagated from the edge of FRP towards the mortar joints. No cracks were observed at the area near supports. Figure 4.4 shows CS3 at failure.

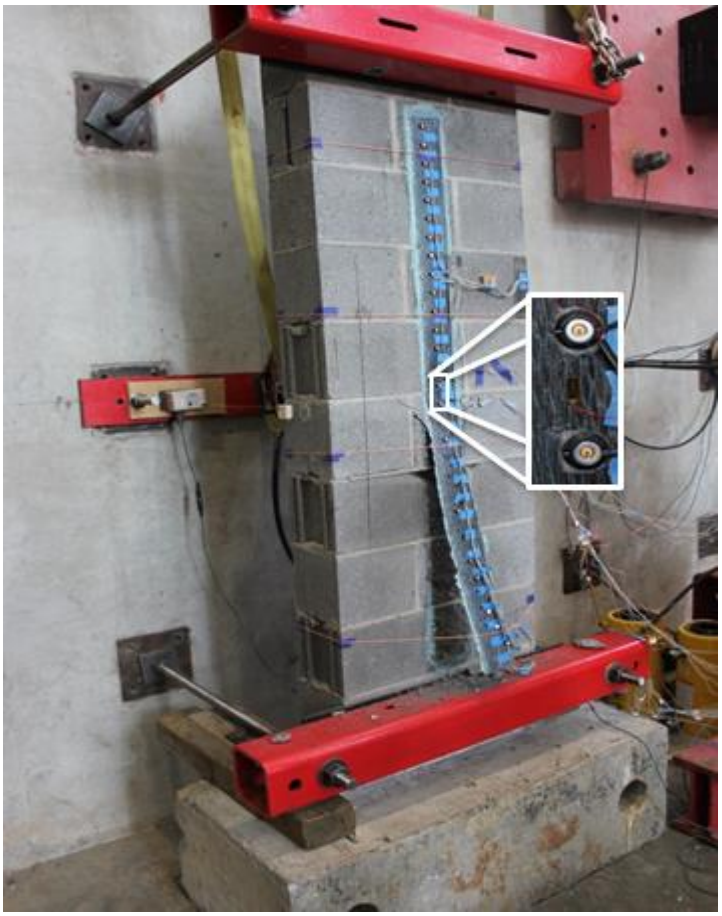

Figure 4.4 - CS3 at Failure

A diagonal crack, which started from the 4th mortar joint and propagated to the edge of the 4 in. x 4 in. steel tube on the compressive side, was observed on the side face. The diagonal crack is shown in Figure 4.5.

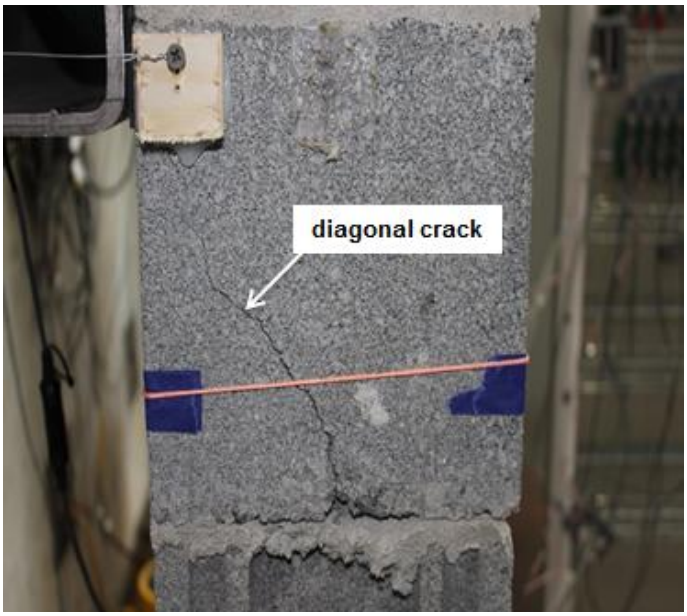

Figure 4.5 - Diagonal Crack on Side Face of CS3

The maximum applied load was 8.8 kips with a corresponding mid-height out-of-plane displacement of 0.75 in. A comparison of measured mid-height strain between the strain gage and the OPTOTRAK system is shown in Figure 4.6. It should be noted that the difference in the measured data is due to the different gage length, which is shown in the insert of Figure 4.4. The strain gage is 0.25 in. long, while the OPTOTRAK system measured the average strain over a 2 in. gage length. Although OPTOTRAK provides a lower strain than the strain gage, the tendency of the two curves is similar. Thus, the strain measured by OPTOTRAK system is reliable. All the strain data shown in the remainder of this chapter is that measured by the OPTOTRAK system.

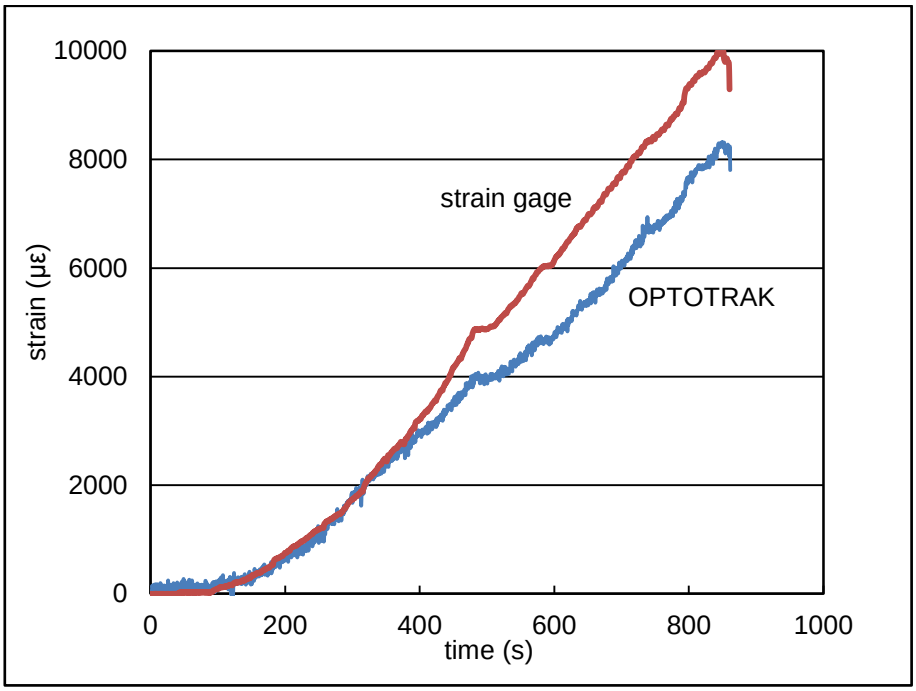

Figure 4.6 - Measured FRP Strain of CS3

The mid-height deflection was measured by both the OPTOTRAK system and string pots. Figure 4.7 shows the comparison of the measured mid-height out-of-plane deflection between the two measuring methods. It can be seen clearly in Figure 4.7 that the deflection measured by OPTOTRAK is almost the same as that of the string pots. Thus, all the out-of-plane deflection shown in the remainder of this chapter is that measured by the OPTOTRAK system. It should be noted that the rigid body movement of CS3, as well as that of the other wallettes, was subtracted from the measured out-of-plane displacement. The load – strain curves and the load – mid-height deflection curves are given in Figure 4.8 and Figure 4.9, respectively.

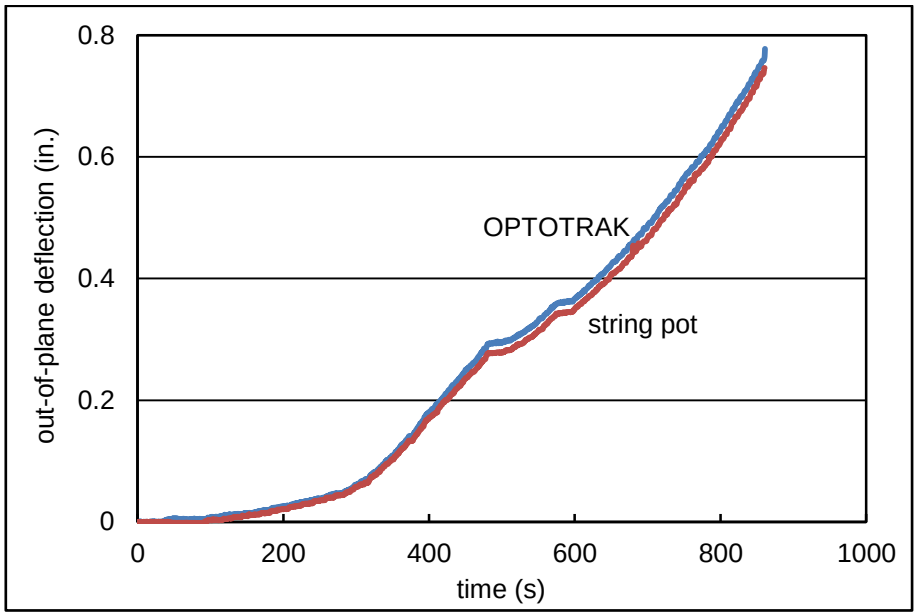

Figure 4.7 - Mid-height Out-of-plane Deflection of CS3

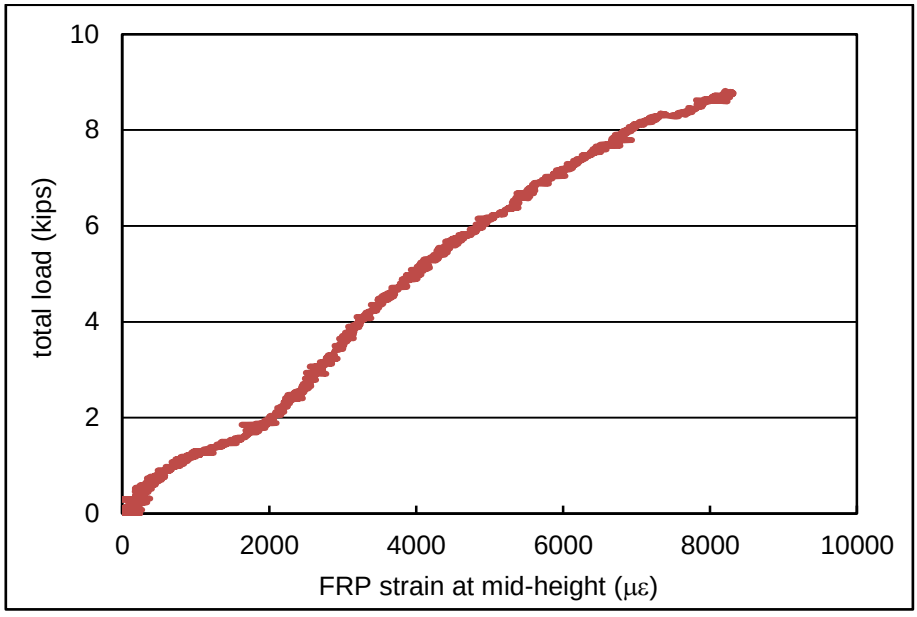

Figure 4.8 - Load – Mid-height Strain Curve of CS3

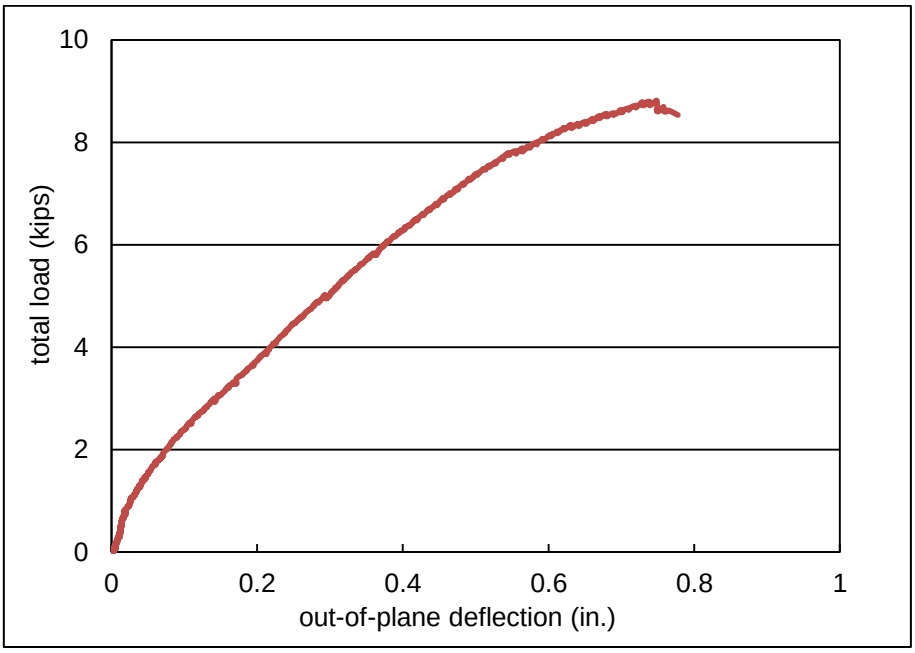

Figure 4.9 - Load – Mid-height Deflection Curve of CS3

The FRP strain distribution and the out-of-plane deflection profile at selected applied loads are shown in Figure 4.10 and Figure 4.11, respectively. It should be noted that the horizontal grid lines in Figure 4.10 show the location of mortar joints. As shown in Figure 4.10, the increase in FRP strain below mid-height as the ultimate load was reached is an indication of the rapid propagation of the IC debonding crack from the location of maximum moment towards the bottom of the wallette. The maximum measured strain of FRP occurred at the location between the 13th and 14th LED targets, which is the same location as the diagonal crack on the wallette surface. For reference, the LED targets were numbered from the bottom to top. The numbering method is consistent in the rest part of this chapter.

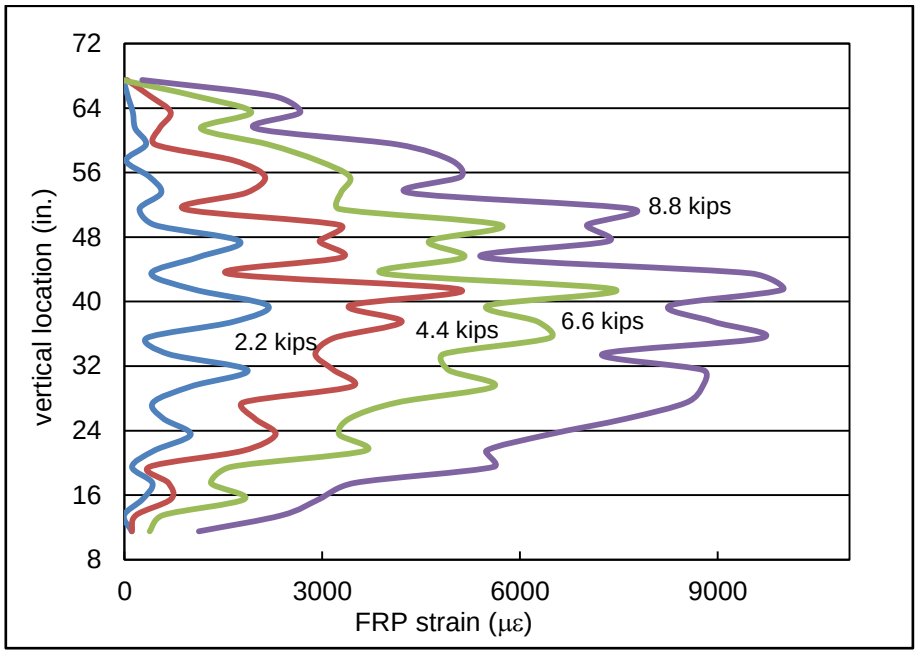

Figure 4.10 - FRP Strain Distribution of CS3

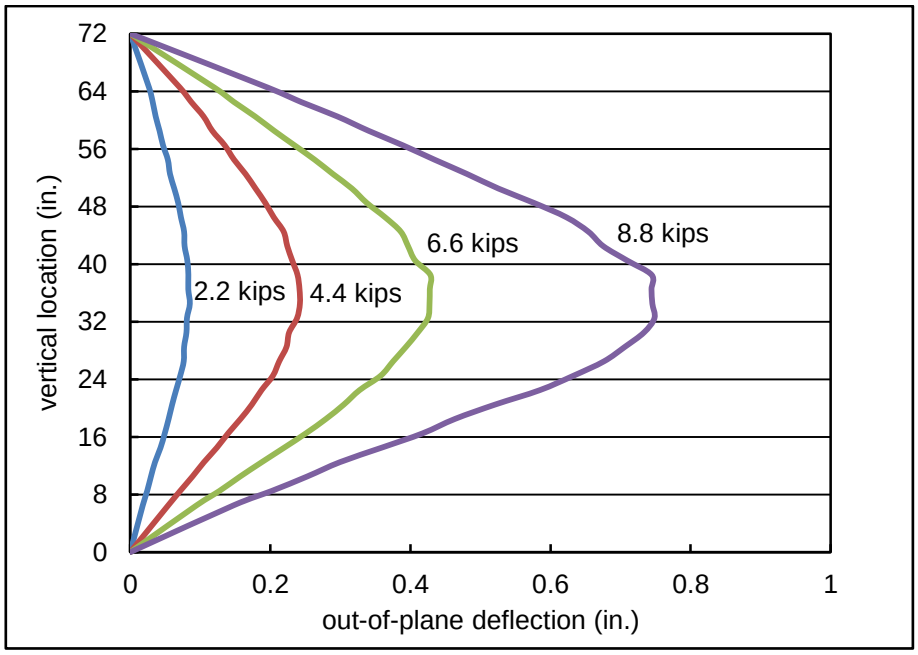

Figure 4.11 - Out-of-Plane Deflection of CS3

4.2.2. Wallette CS6

Wallette CS6 was strengthened by a 6 in. wide single layer of CFRP, which failed by IC debonding. Debonding started at the location between the 17th and 18th LED targets, and then propagated rapidly to the top of the wallette. A thin layer of masonry remained attached to the FRP laminate. Diagonal cracks on the wallette surface propagated from the edge of FRP towards the 6th mortar joints. The widest horizontal crack occurred at the 6th mortar joint instead of the 5th mortar joint (mid-height). No cracks were observed at the area near supports. Figure 4.12 shows CS6 at failure.

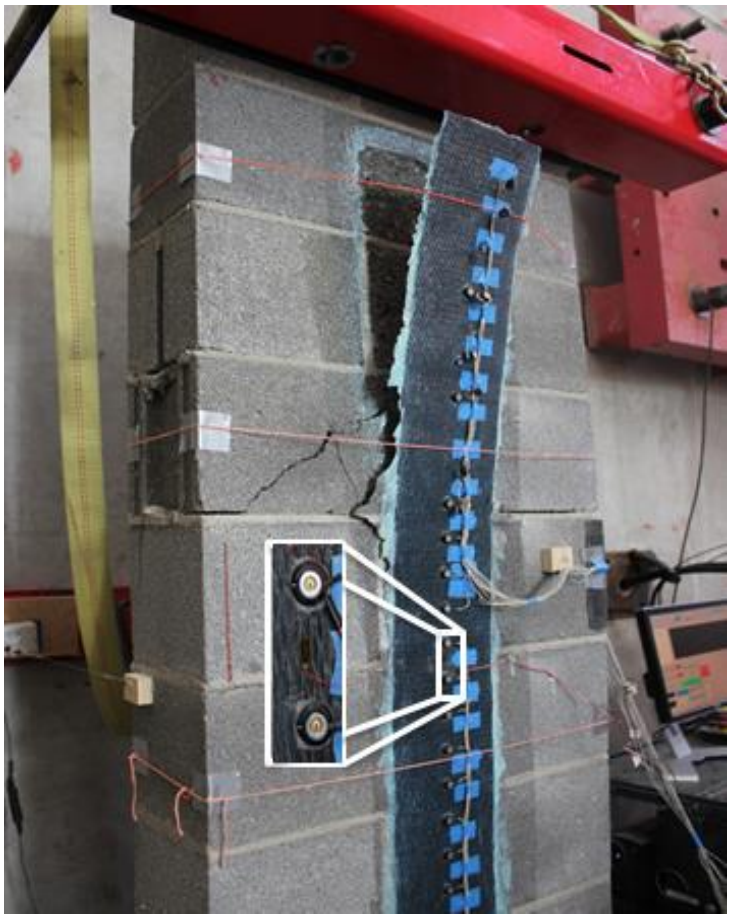

Figure 4.12 - CS6 at Failure

A diagonal crack, which started from the 6th mortar joint and propagated to the edge of the 4 in. x 4 in. steel tube on the compressive side, was observed on the side face. A small joint sliding was observed at the 6th mortar joint. The diagonal crack and the joint sliding are shown in Figure 4.13.

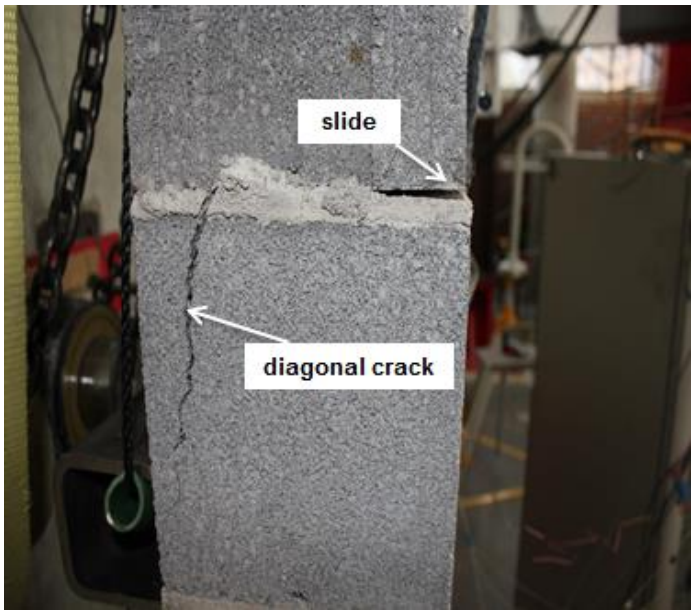

Figure 4.13 - Diagonal Crack on Side Surface of CS6

The maximum applied load was 11.0 kips with a corresponding mid-height out-of-plane displacement of 0.64 in. The load – strain curve and the load – mid-height deflection curve of CS6 are shown in Figure 4.14 and Figure 4.15, respectively.

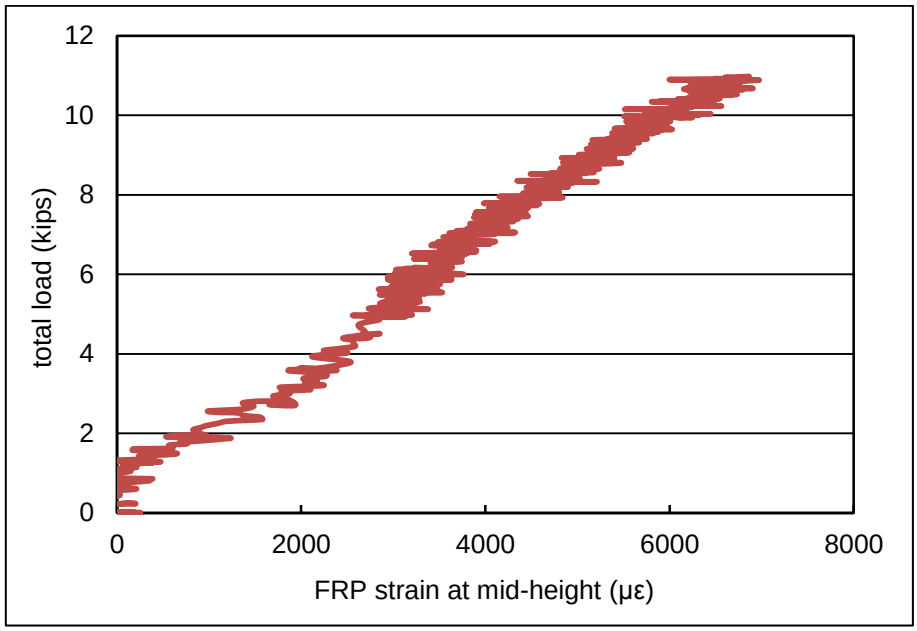

Figure 4.14 - Load – Mid-height Strain Curve of CS6

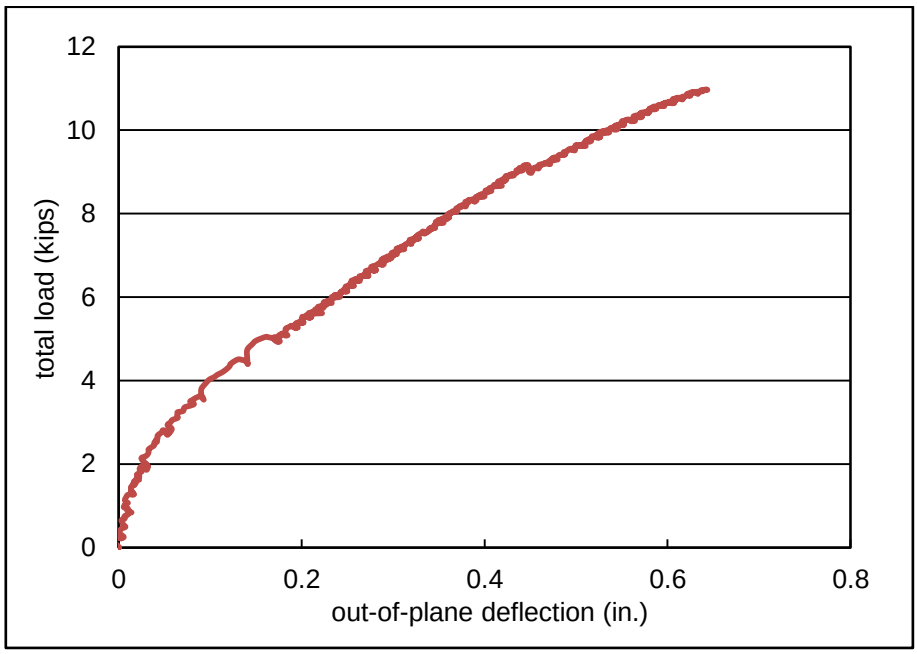

Figure 4.15 - Load – Mid-height Deflection Curve of CS6

For illustrative purposes, the FRP strain distribution and the out-of-plane deflection at selected applied loads are shown in Figure 4.16 and Figure 4.17, respectively. At failure, the strain at 6th and 7th mortar joints is higher than the mid-height strain. During testing, the horizontal crack was originally observed at the mid-height mortar joint at low load levels. As the load increased, a significant horizontal crack was observed at the 6th mortar joint, which was wider than the mid-height mortar joint crack and caused the joint to slide at failure. This caused a significant FRP strain at the 6th mortar joint. A diagonal crack started at the 6th mortar joint and propagated rapidly to the 7th mortar joint, which caused the maximum FRP strain to occur at the 7th mortar joint, as can be seen in Figure 4.16.

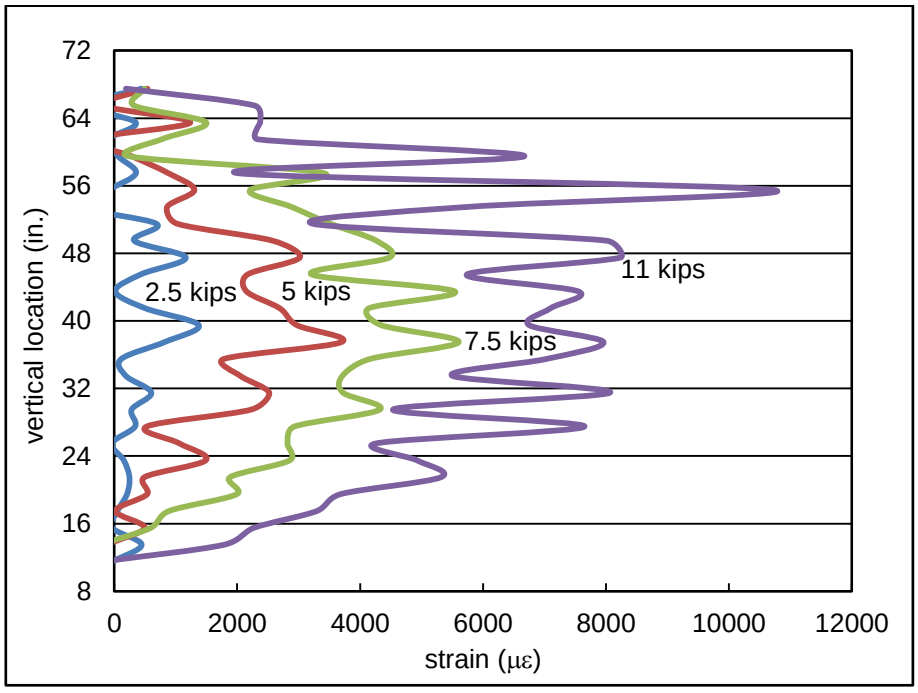

Figure 4.16 - FRP Strain Distribution of CS6

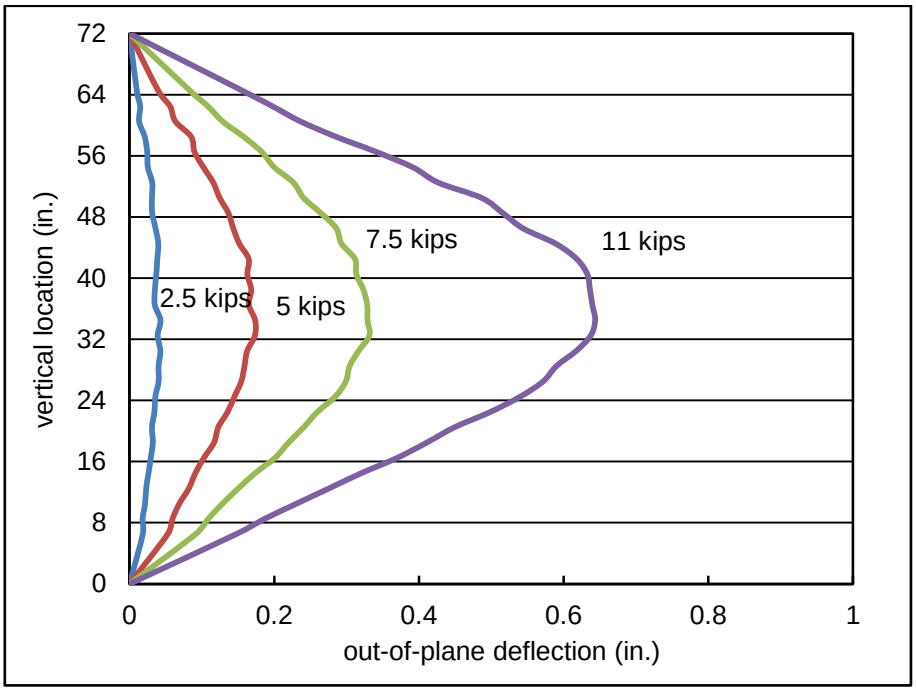

Figure 4.17 - Out-of-Plane Deflection of CS6

4.2.3. Wallette CS8

Wallette CS8 was strengthened by an 8 in. wide single layer CFRP, which failed by IC debonding. Debonding started at the location of 20th and 21st LED targets, and then propagated rapidly to the top of the wallette. A thin layer of masonry remained attached to the FRP laminate. Two significant diagonal cracks on the wallette surface propagated from the edge of the FRP towards the 5th and 6th mortar joints, at the left and right sides, respectively. Another two small diagonal cracks propagated from the edge zone of 5th mortar joint to the location between the 18th and 19th LED targets. Small horizontal cracks were

observed at the mid-height mortar joint and no cracks were observed at the area near supports. Figure 4.18 shows CS8 at failure.

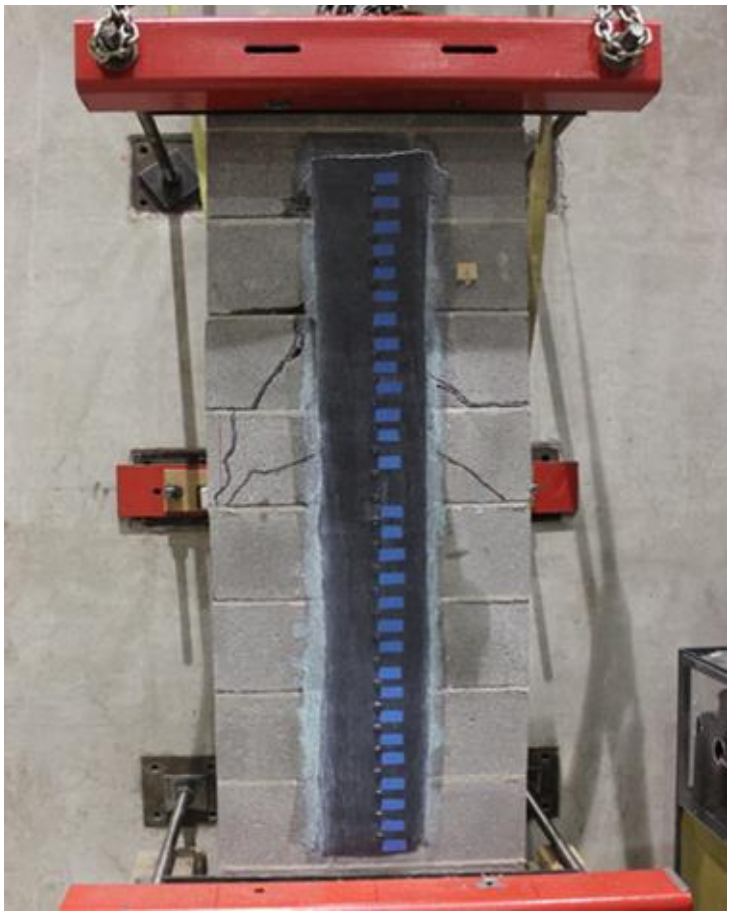

Figure 4.18 - CS8 at Failure

Diagonal cracks, which started from the mortar joints and propagated to the edge of the 4 in. x 4 in. steel tube on the compressive side, were observed on both the left and right side

faces. The diagonal cracks on left face started at the 7th mortar joint and the cracks on right face started at the 6th mortar joint. Both diagonal cracks are shown in Figure 4.19. Joint sliding was observed along the 7th mortar joint which is shown in Figure 4.20. When debonding occurred, a piece of the CMU at the 7th mortar joint remained attached to the FRP laminate, which can be seen in Figure 4.20.

(a) Left Side **(b) Right Side**

Figure 4.19 - Diagonal Cracks on Side Faces of CS8

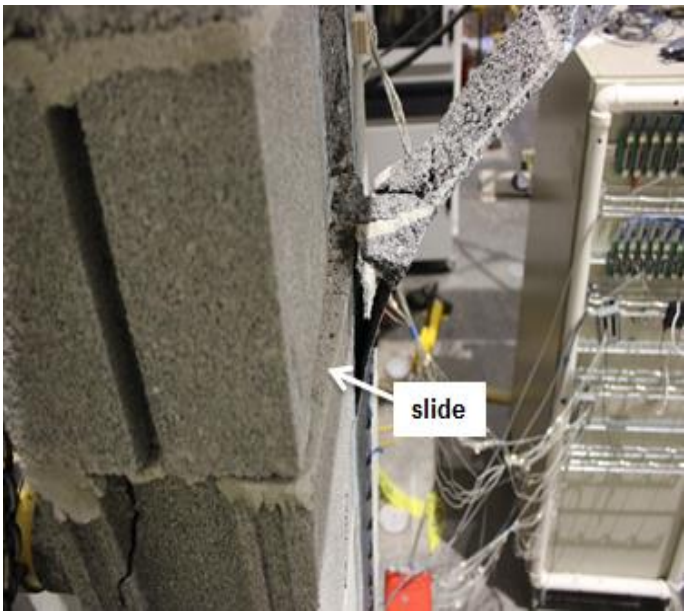

Figure 4.20 - Sliding of Mortar Joint of CS8

The maximum applied load was 13.0 kips with a corresponding mid-height out-of-plane displacement of 0.61 in. The load – strain curve and the load – mid-height deflection curve of CS8 are shown in Figure 4.21 and Figure 4.22, respectively.

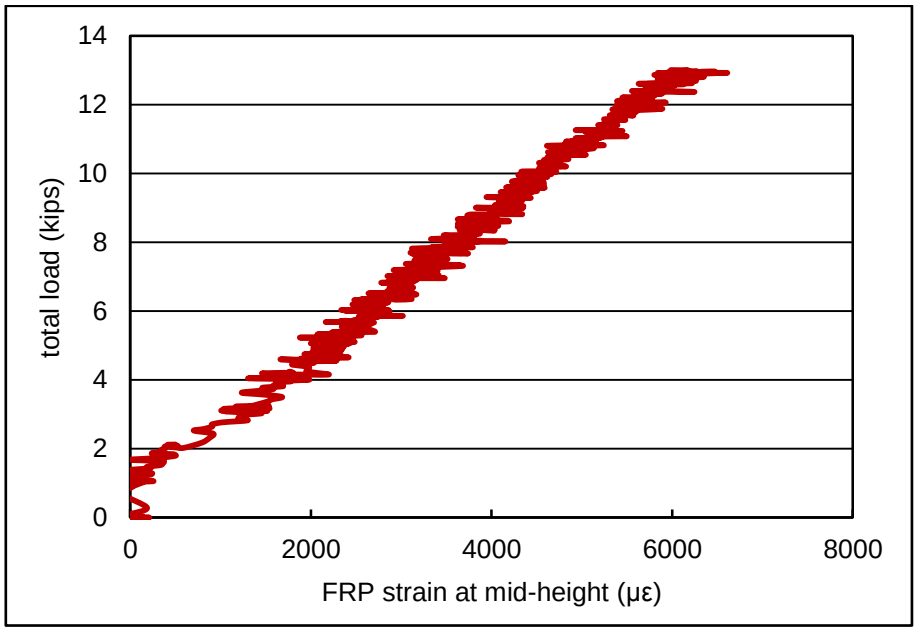

Figure 4.21 - Load – Mid-height Strain Curve of CS8

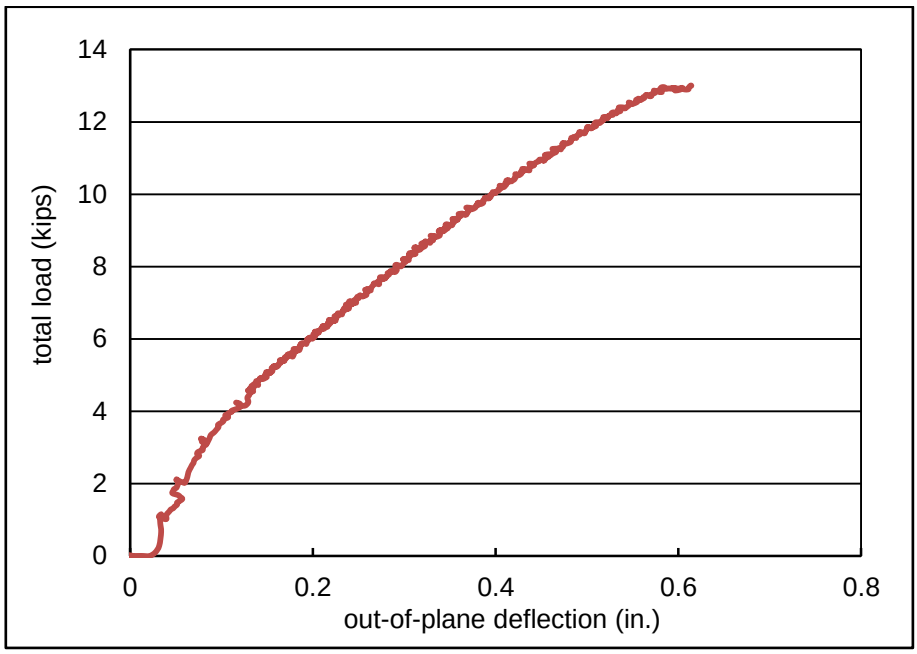

Figure 4.22 - Load – Mid-height Deflection Curve of CS8

For illustrative purposes, the FRP strain distribution and the out-of-plane deflection at selected applied loads are shown in Figure 4.23 and Figure 4.24, respectively. The maximum FRP strain occurred between 18th and 19th LED targets, where the diagonal cracks converged. It should be noted that the strain increased most at the 7th mortar joint, where the joint sliding occurred.

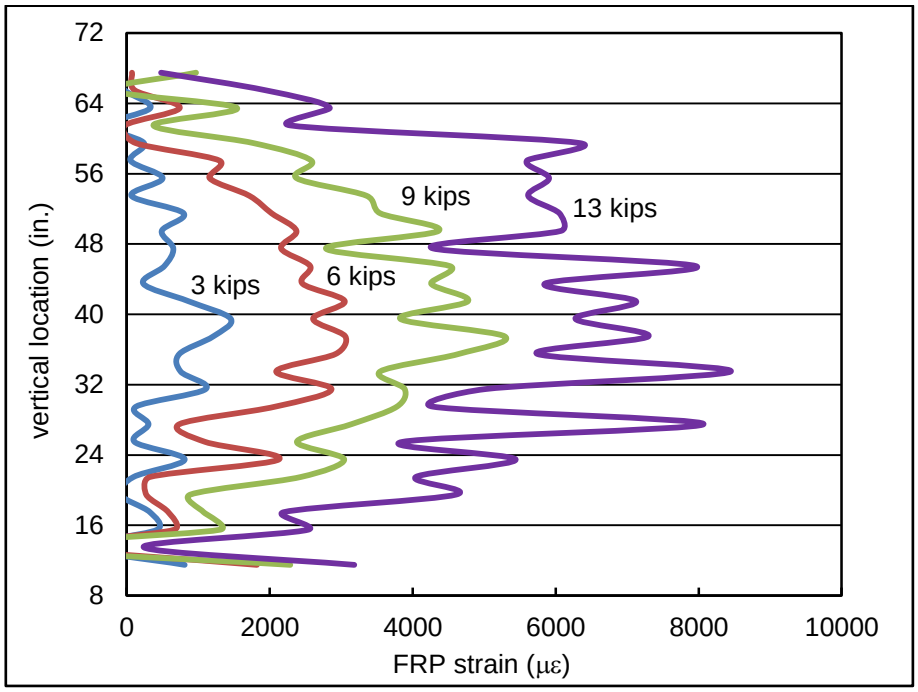

Figure 4.23 - FRP Strain Distribution of CS8

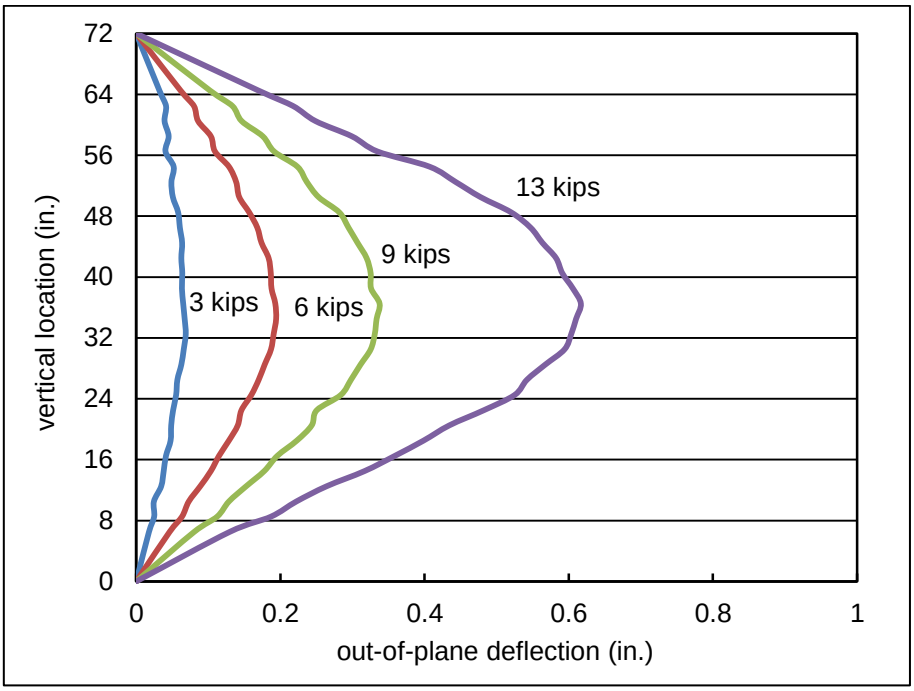

Figure 4.24 - Out-of-Plane Deflection of CS8

4.2.4. Wallette CD3

Wallette CD3 was strengthened by two layers of 3 in. wide CFRP, which failed by IC debonding. The debonding started at the mid-height and then propagated rapidly to the bottom of the wallette. A thin layer of masonry remained attached to the FRP laminate. Two diagonal cracks were observed on the wallette surface. The first one propagated from the 5th mortar joint to the location between 14th and 15th LED targets. The second propagated from the 4th mortar joint to the location between 10th and 11th LED targets. Horizontal cracks were

observed at the 3rd, 4th and 5th mortar joints. No cracks were observed at the area near supports. Figure 4.25 shows CD3 at failure.

Diagonal cracks, which started from the 4th mortar joint and propagated to the edge of the 4 in. x 4 in. steel tube on the compressive side, were observed on both the left and right side faces. The diagonal cracks are shown in Figure 4.26. No joint sliding was observed at failure.

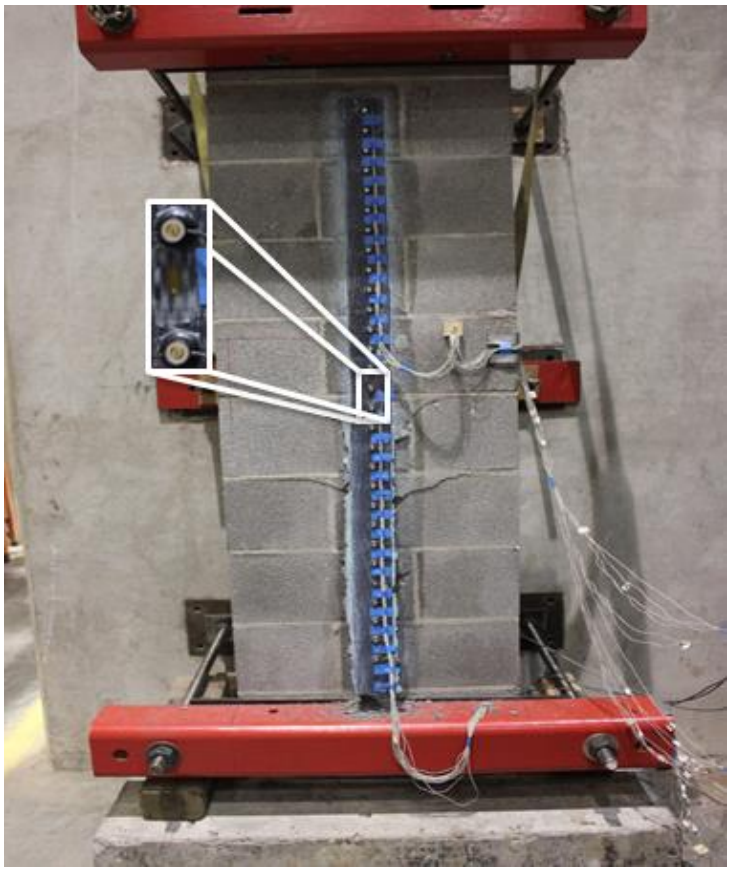

Figure 4.25 - CD3 at Failure

(a) Left Side **(b) Right Side**

Figure 4.26 - Diagonal Cracks on Side Faces of CD3

The maximum applied load was 10.1 kips with a corresponding mid-height out-of-plane displacement of 0.50 in. The load – strain curve and the load – mid-height deflection curve of CS8 are shown in Figure 4.27 and Figure 4.28, respectively.

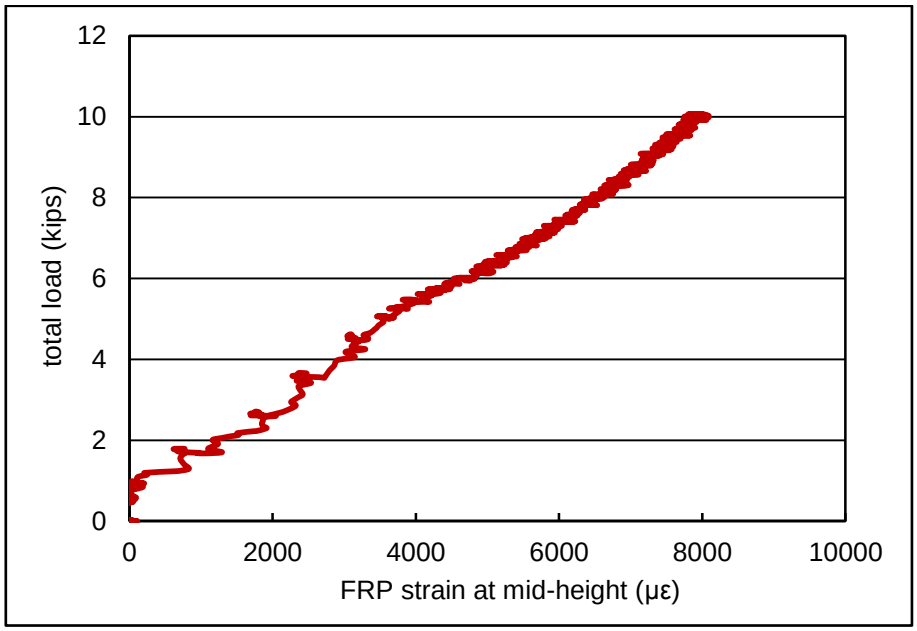

Figure 4.27 - Load – Mid-height Strain Curve of CD3

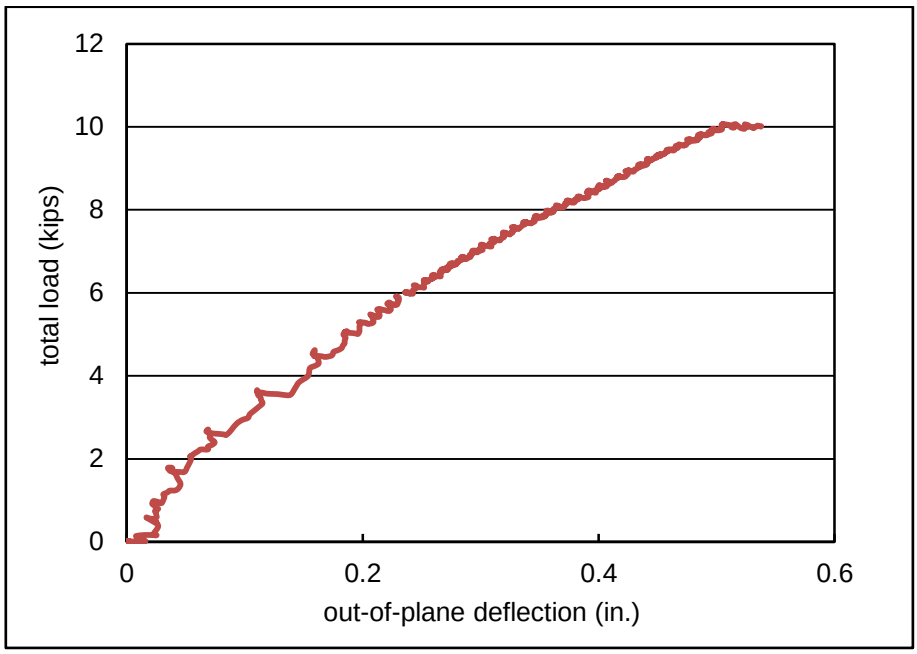

Figure 4.28 - Load – Mid-height Deflection Curve of CD3

For illustrative purposes, the FRP strain distribution and the out-of-plane deflection at selected applied loads are shown in Figure 4.29 and Figure 4.30, respectively. As can be seen in Figure 4.29, the maximum strain occurred at the mid-height mortar joint. The increase in FRP strain below mid-height as the ultimate load was reached is an indication of the rapid propagation of the IC debonding crack from the location of maximum moment towards the bottom of the wallette. On the debonded part of the FRP laminate, the local maximum measured FRP strain occurred at the location of the mortar joints where the masonry flexural cracks developed.

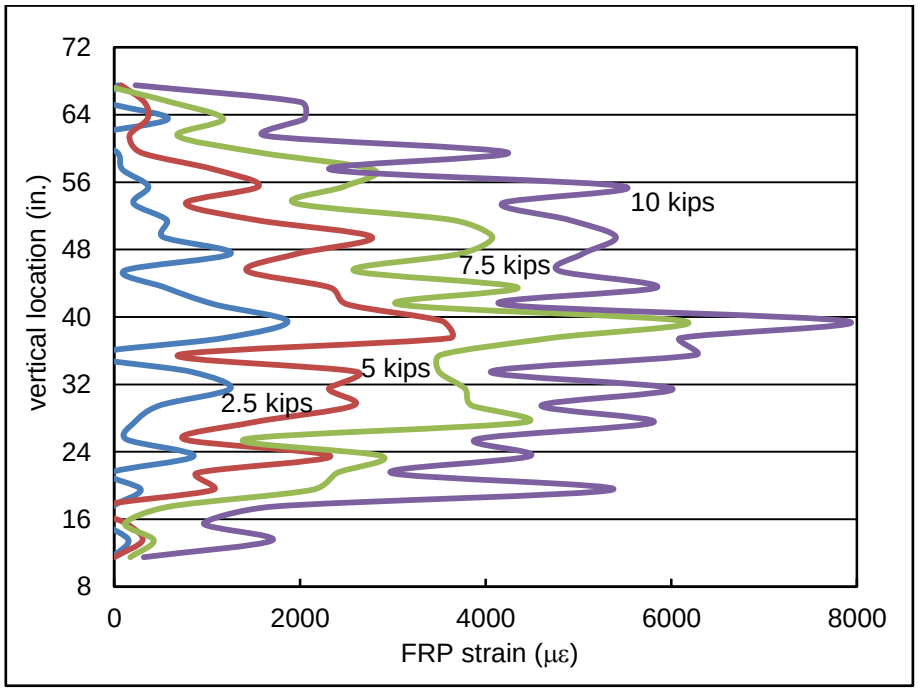

Figure 4.29 - FRP Strain Distribution of CD3

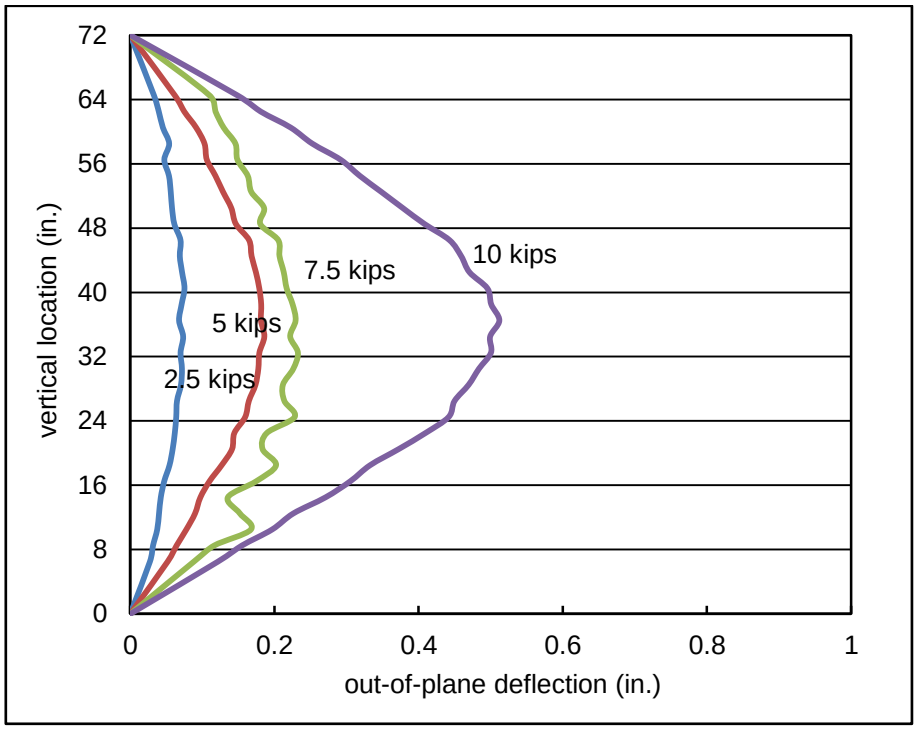

Figure 4.30 - Out-of-Plane Deflection of CD3

4.3. GFRP Strengthened Wallettes

Two failure modes were observed for the GFRP strengthened wallettes: (1) IC debonding of the FRP; and (2) FRP rupture. The detailed failure mode of each wallette is described in this section.

4.3.1. Wallette GS3-1

Wallette GS3-1 was strengthened by a 3 in. wide single layer of GFRP, which failed by FRP rupture below the mid-height. The rupture started at the left edge of FRP and then propagated rapidly to the right edge of FRP. The FRP laminate remained fully attached to the masonry surface and no sign of debonding was observed. The widest horizontal crack occurred at the 5^{th} mortar joint (mid-height). Small cracks were observed at the 4^{th} and 6^{th} mortar joints. Since GS3-1 failed at low load, less damage was observed on the Wallette. No cracks were found at other mortar joints. In addition, no diagonal cracks were observed on the side faces. Figure 4.31 shows GS3-1 at failure.

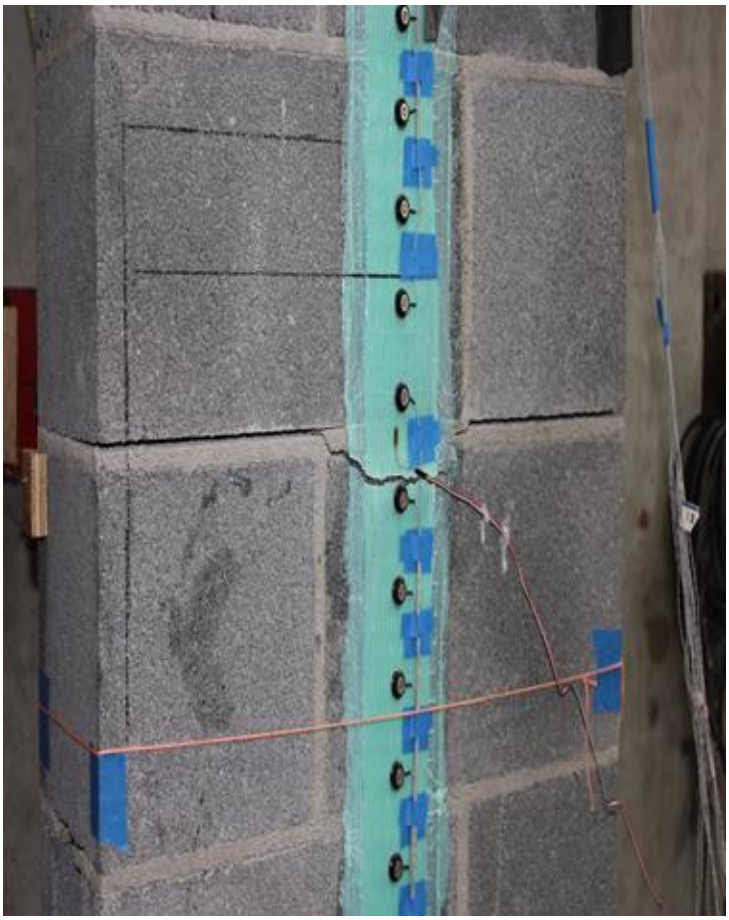

Figure 4.31 - GS3-1 at Failure

The maximum applied load was 6.0 kips with a corresponding mid-height out-of-plane displacement of 0.35 in. The load – strain curve and the load – mid-height deflection curve of GS3-1 are shown in Figure 4.32 and Figure 4.33, respectively. As can be seen in Figure 4.33, the load capacity dropped to 5 kips after rupture occurred, which is higher than the capacity of the control wallette.

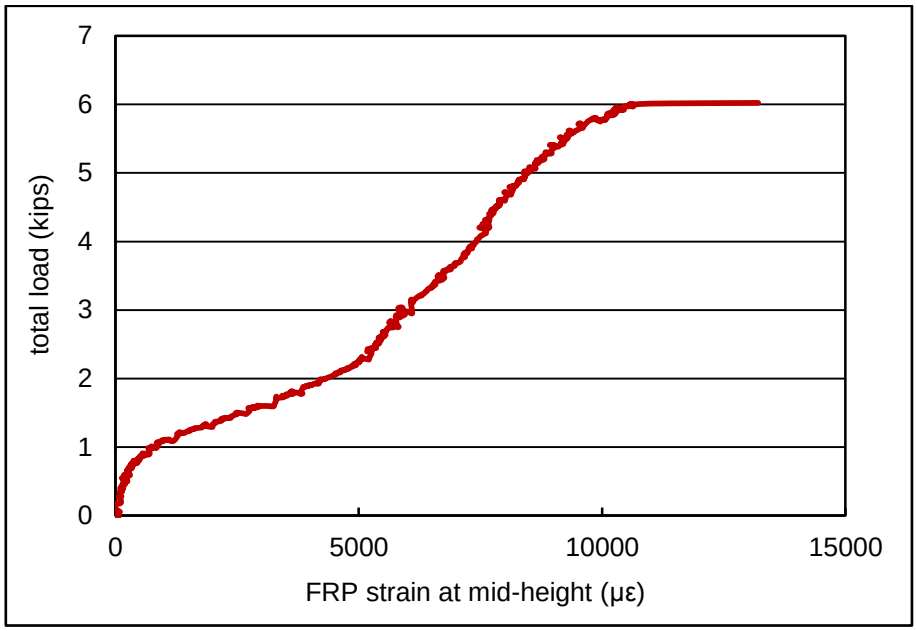

Figure 4.32 - Load – Mid-height Strain Curve of GS3-1

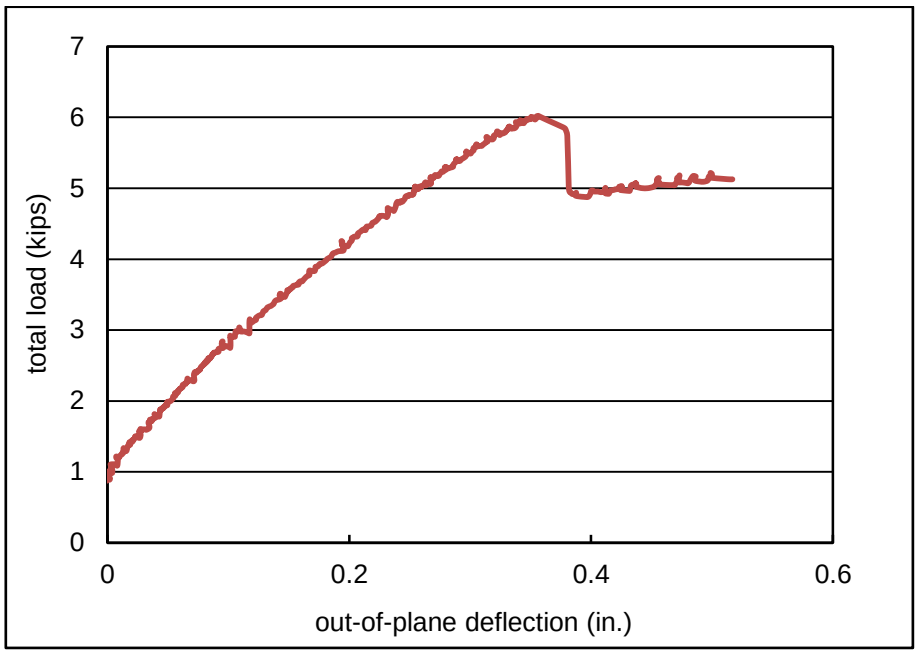

Figure 4.33 - Load – Mid-height Deflection Curve of GS3-1

For illustrative purposes, the FRP strain distribution and the out-of-plane deflection at selected applied loads are shown in Figure 4.34 and Figure 4.35, respectively. As can be seen in Figure 4.34, the strain decreases from the mid-height to the end of FRP and the maximum strain occurred at the mid-height mortar joint. Interestingly, the strain distribution shows extreme concentration at the mortar joints. And there is almost no strain developing between the mortar joints, indicating that there is no debonding between the FRP and the masonry surface.

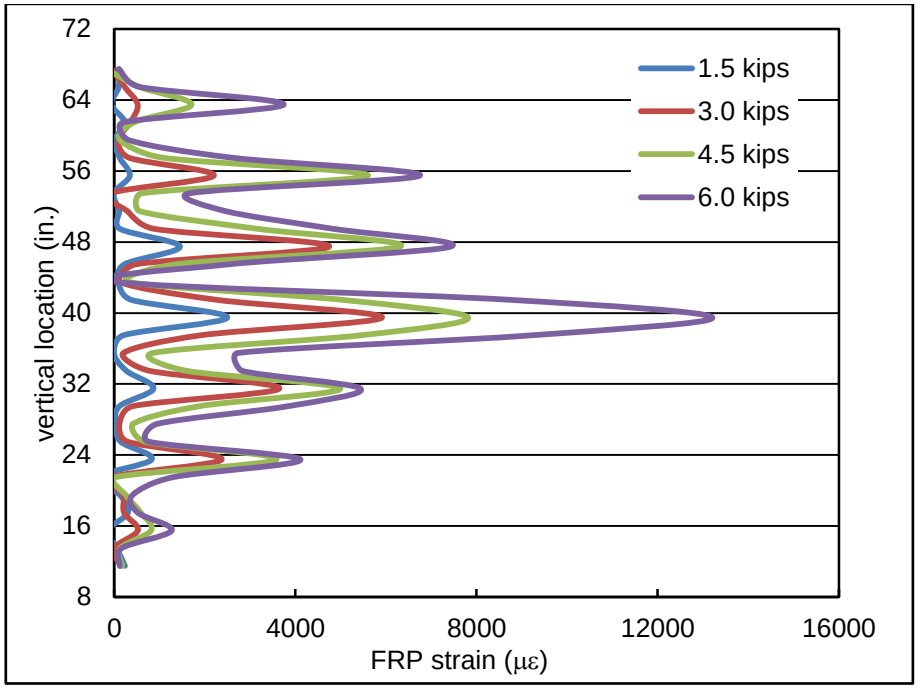

Figure 4.34 - FRP Strain Distribution of GS3-1

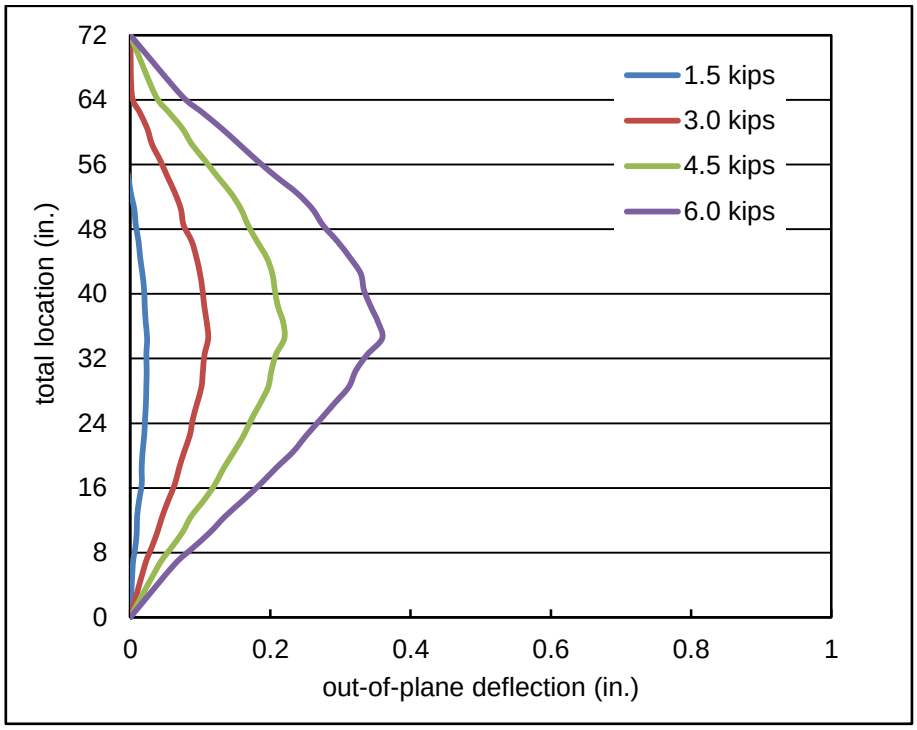

Figure 4.35 - Out-of-Plane Deflection of GS3-1

4.3.2. Wallette GS3-2

Since GS3-1 failed by FRP rupture, which was not initially expected, this test was repeated and designated as GS3-2. Wallette GS3-2 also failed by FRP rupture at the 5th mortar joint (mid-height). The rupture crack started at the left edge and then propagated rapidly to the right edge of the FRP. The FRP fully remained attached to the wallette surface and no debonding was observed. Small cracks were observed at the other mortar joints. No cracks were found at the area near supports. In addition, no diagonal cracks were observed on the side faces. Figure 4.36 shows GS3-2 at failure.

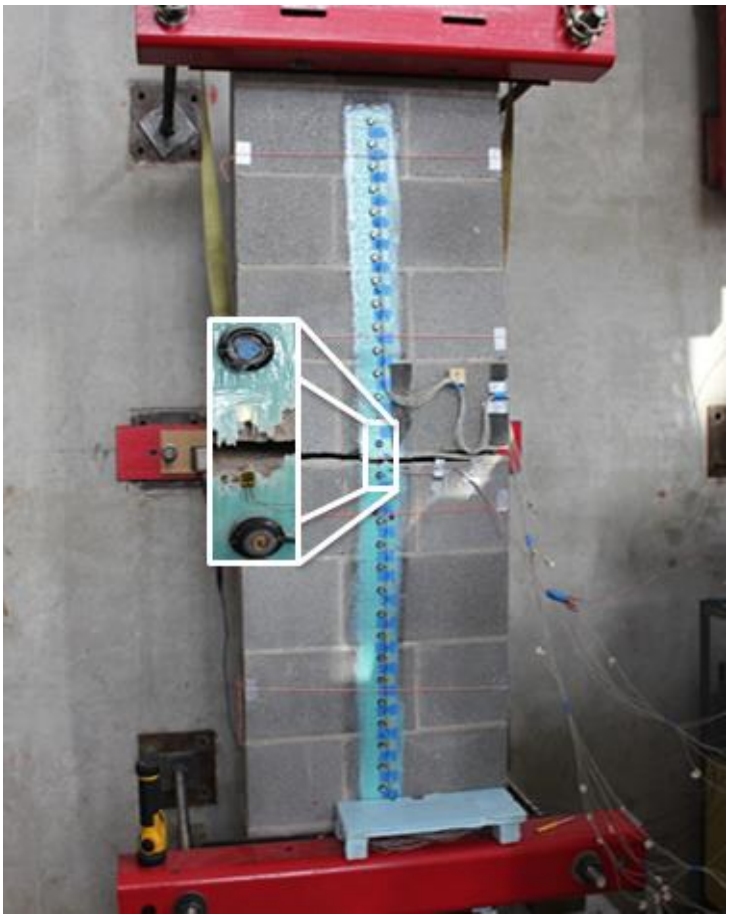

Figure 4.36 - GS3-2 at Failure

The maximum applied load was 5.2 kips with a corresponding mid-height out-of-plane displacement of 0.55 in. The load – strain curve and the load – mid-height deflection curve of GS3-1 are shown in Figure 4.37 and Figure 4.38, respectively. As can be seen in Figure 4.38, the load capacity dropped to 4.5 kips after rupture occurred, which is almost the same as the capacity of the control wallette.

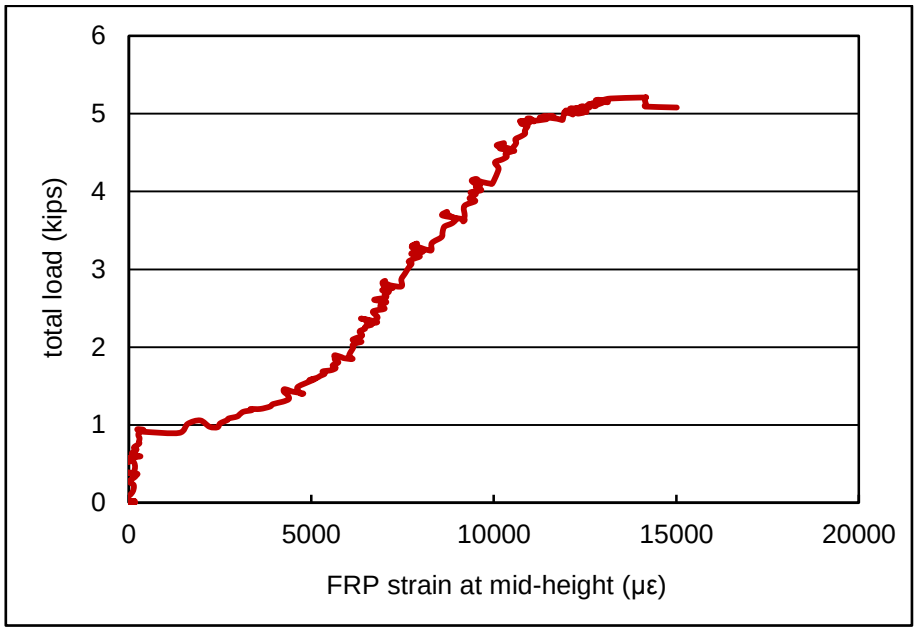

Figure 4.37 - Load – Mid-height Strain Curve of GS3-2

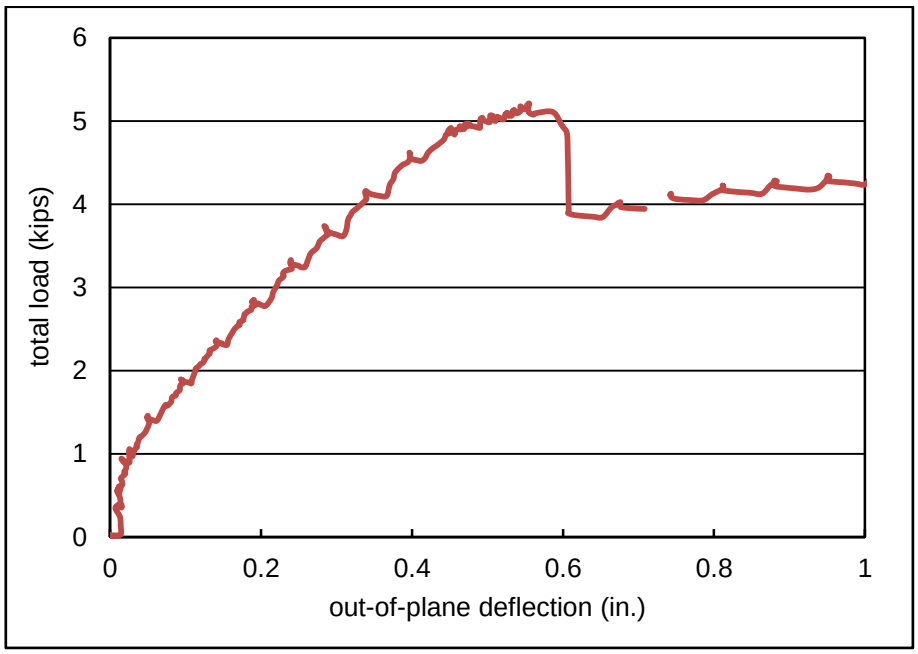

Figure 4.38 - Load – Mid-height Deflection Curve of GS3-2

The FRP strain distribution and the out-of-plane deflection at selected applied loads are shown in Figure 4.39 and Figure 4.40, respectively. As can be seen in Figure 4.39, the strain decreases from the mid-height to the ends of FRP and the maximum strain occurred at the mid-height mortar joint. All the local FRP strain maxima occurred at mortar joints. Similarly to GS3-1, the strain concentrated at the mortar joints.

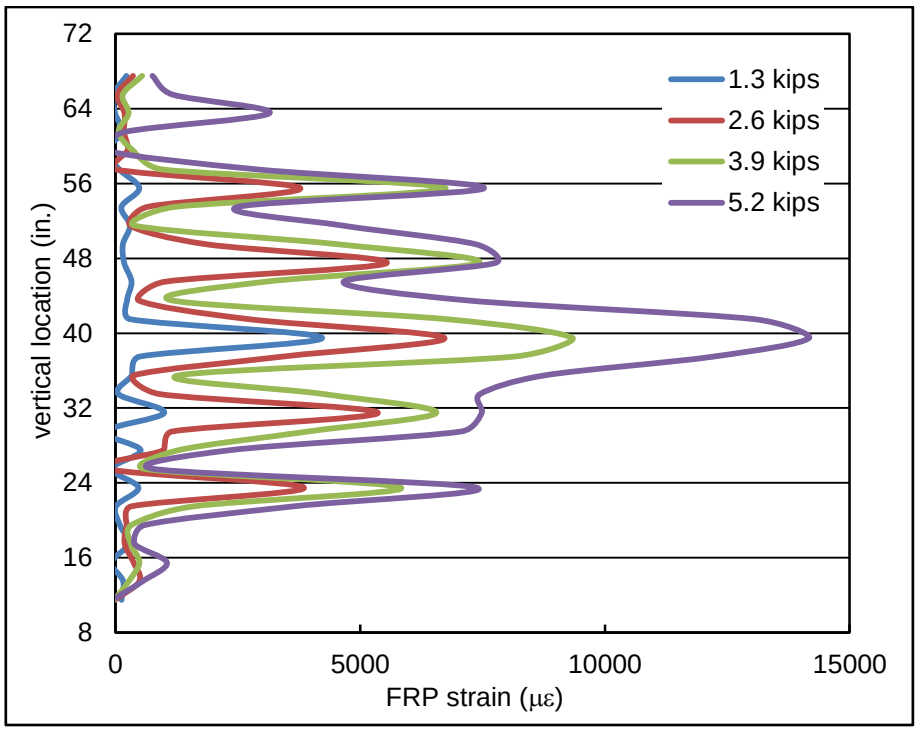

Figure 4.39 - FRP Strain Distribution of GS3-2

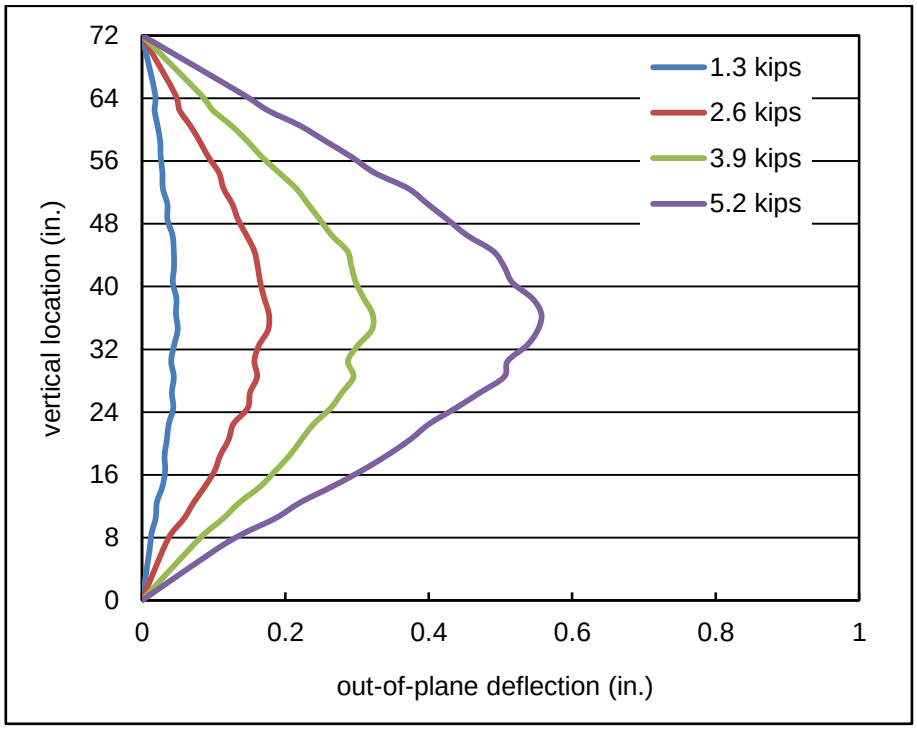

Figure 4.40 - Out-of-Plane Deflection of GS3-2

4.3.3. Wallette GS6

Wallette GS6 was strengthened by a 6 in. wide single layer of GFRP, which failed by FRP rupture at the 5th mortar joint (mid-height). The rupture started at the left edge of the FRP and then propagated rapidly to the right edge. No sign of debonding was observed. Horizontal cracks were observed at the 4th and 6th mortar joints. No cracks were found at the area near supports and other mortar joints. In addition, no diagonal cracks were observed on the side faces. Figure 4.41 shows GS6 at failure.

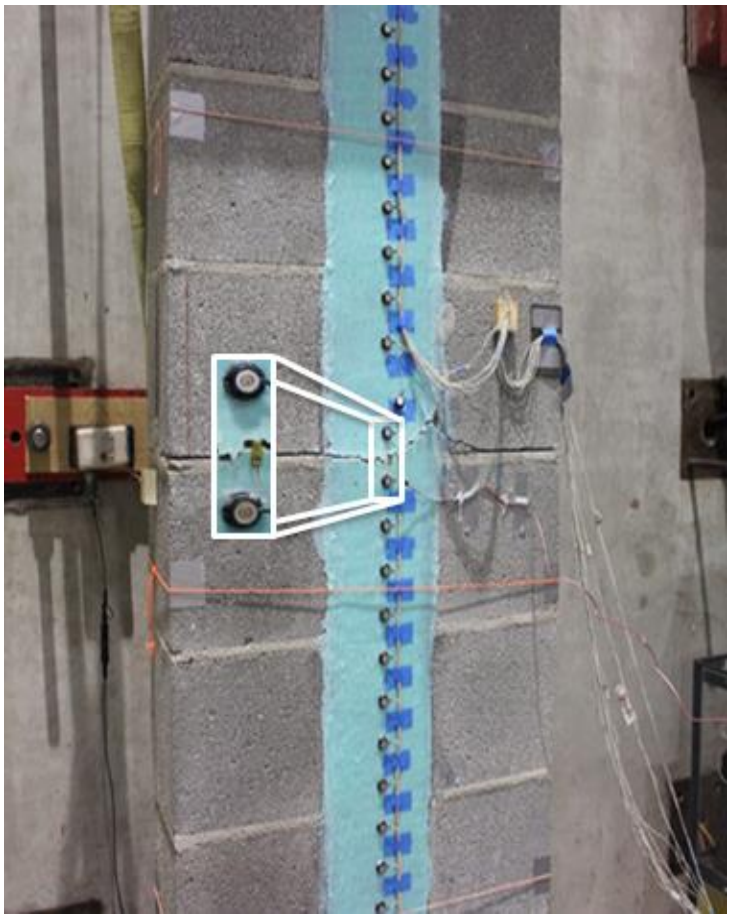

Figure 4.41 - GS6 at Failure

The maximum applied load was 6.5 kips with a corresponding mid-height out-of-plane displacement of 0.48 in. The load – strain curve and the load – mid-height deflection curve of GS3-1 are shown in Figure 4.42 and Figure 4.43, respectively.

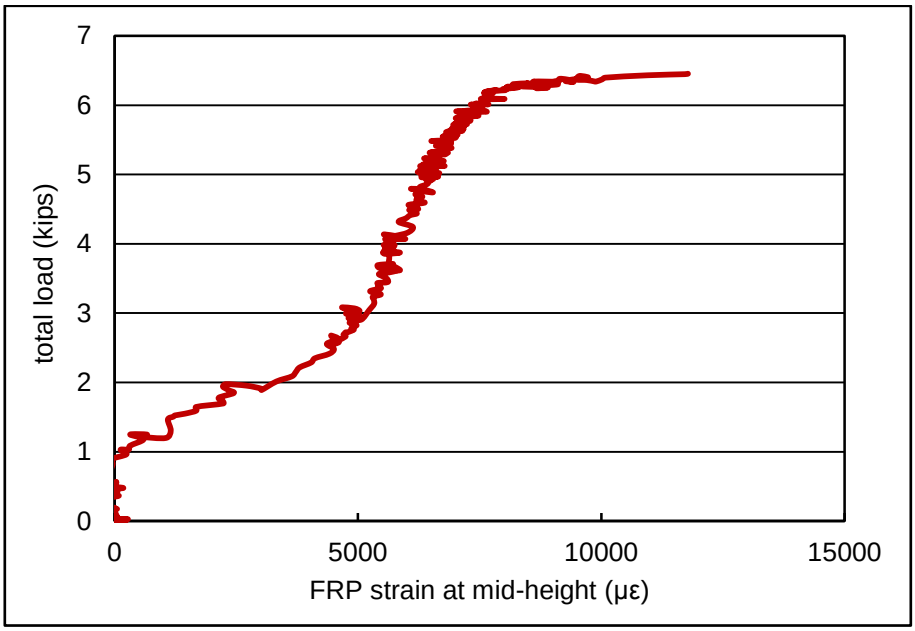

Figure 4.42 - Load – Mid-height Strain Curve of GS6

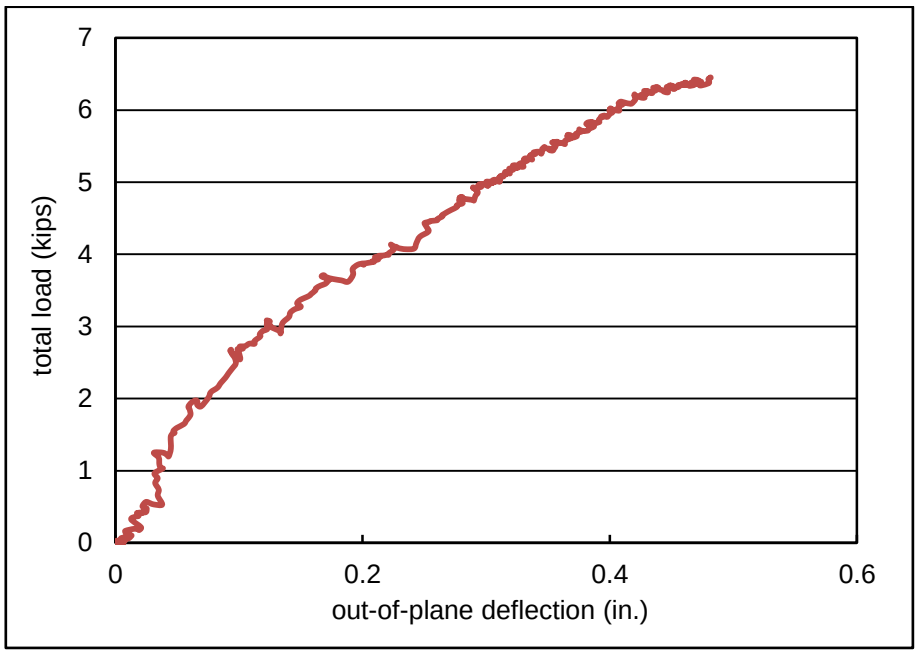

Figure 4.43 - Load – Mid-height Deflection Curve of GS6

The FRP strain distribution and the out-of-plane deflection at selected applied loads are shown in Figure 4.44 and Figure 4.45, respectively. As can be seen in Figure 4.44, the maximum strain occurred at mid-height and the strain decreases from the mid-height to the ends of FRP. Interestingly, although GS6 also failed by FRP rupture, the strain concentration at the mortar joints is not as previous wallettes.

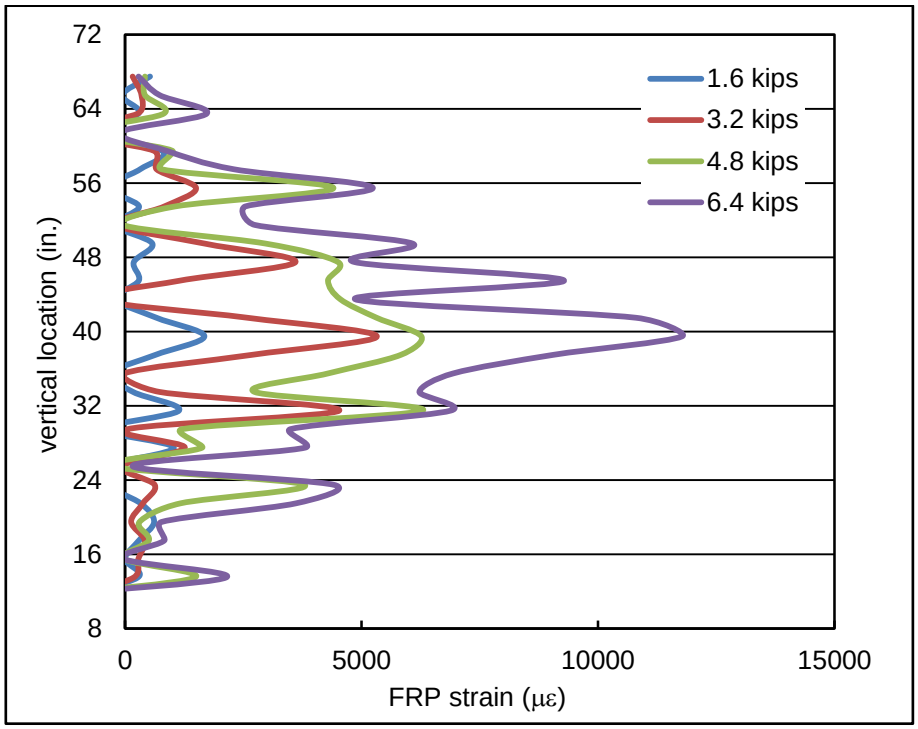

Figure 4.44 - FRP Strain Distribution of GS6

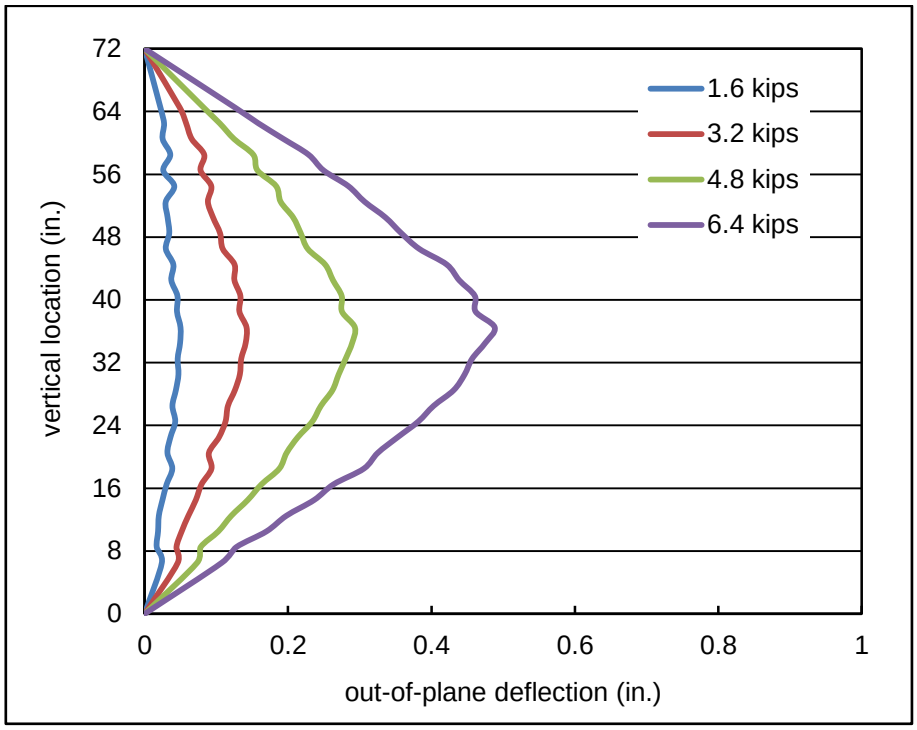

Figure 4.45 - Out-of-Plane Deflection of GS6

4.3.4. Wallette GD3

Wallette GD3 was strengthened by two layers of 3 in. wide GFRP, which failed by IC debonding. Two diagonal cracks, propagating from the edge of the GFRP to the full width of the wallette, were observed on the masonry surface before debonding occurred. Debonding started at the mid-height and started to propagate to both ends of the GFRP. However, complete debonding ultimately occurred by rapid propagation to the bottom end of the GFRP. No cracks were observed at the area near supports. No joint sliding was observed at failure. Figure 4.46 shows GD3 at failure.

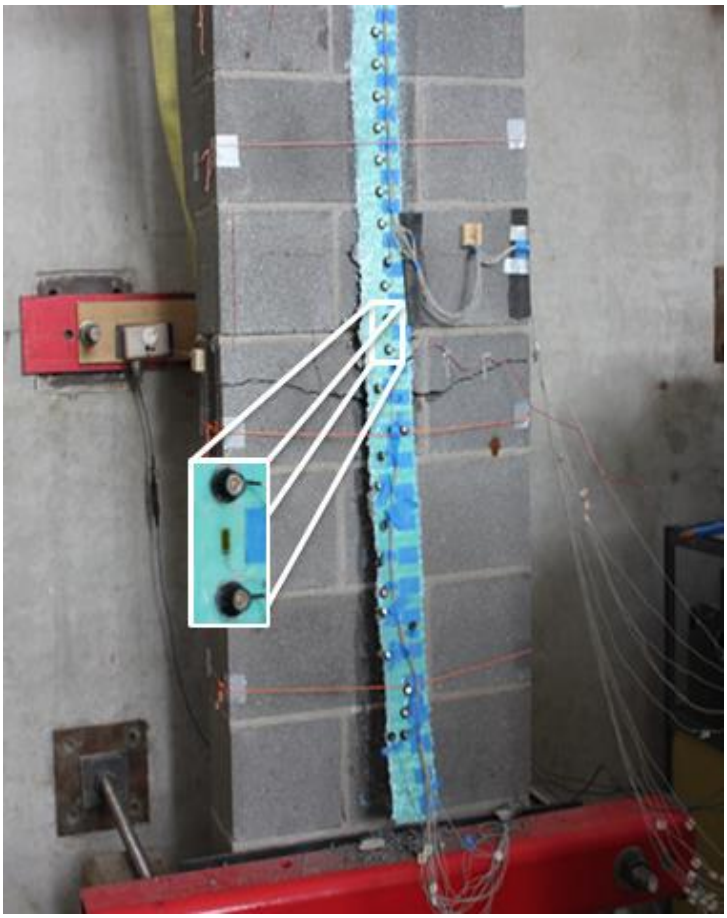

Figure 4.46 - GD3 at Failure

Horizontal and vertical cracks were observed on both the left and right side faces. Interestingly, the horizontal crack occurred on the masonry surface rather than the mortar joints. The horizontal cracks connected with the side diagonal cracks located near the edge of the 4 in. x 4 in. steel tube. The cracks on the side faces are shown in Figure 4.47. These cracks on the side faces resulted in a piece of CMU remaining attached to the GFRP when debonding occurred.

(a) Left Side **(b) Right Side**

Figure 4.47 - Cracks on Side Faces of GD3

The maximum applied load was 7.9 kips with a corresponding mid-height out-of-plane displacement of 0.95 in. The load – strain curve and the load – mid-height deflection curve of GS3-1 are shown in Figure 4.48 and Figure 4.49, respectively.

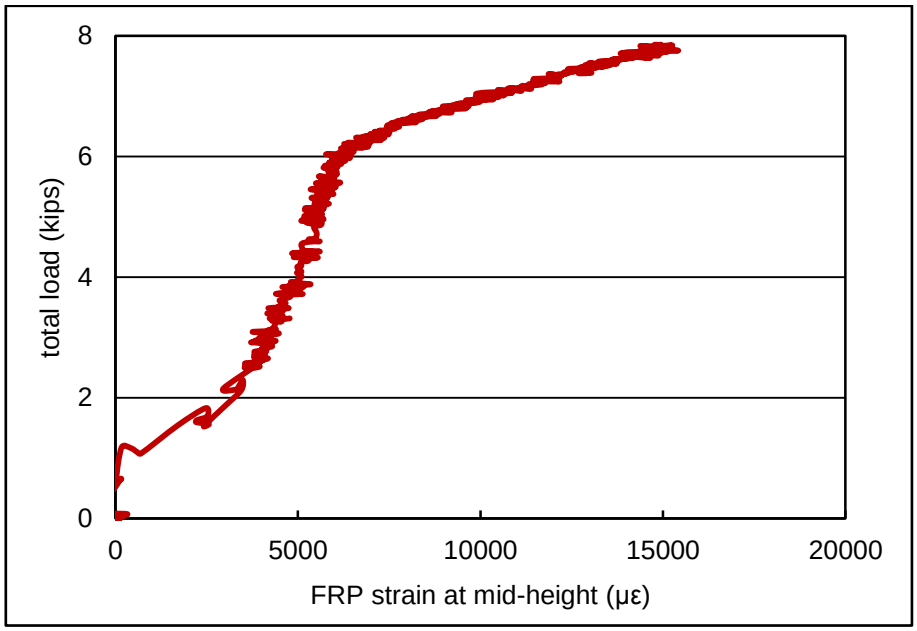

Figure 4.48 - Load – Mid-height Strain Curve of GD3

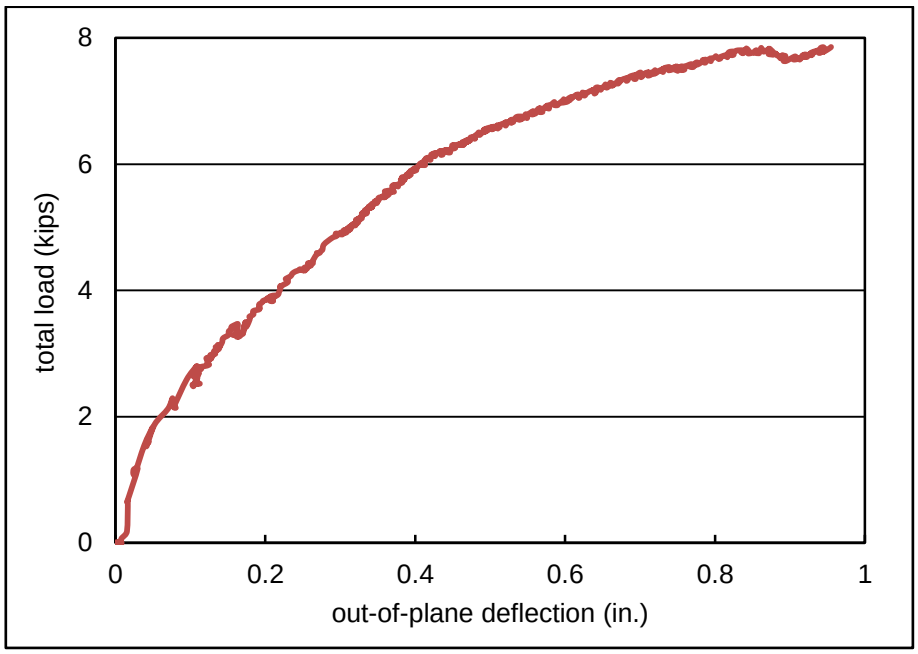

Figure 4.49 - Load – Mid-height Deflection Curve of GD3

The FRP strain distribution and the out-of-plane deflection at selected applied loads are shown in Figure 4.50 and Figure 4.51, respectively. As can be seen in Figure 4.50, the maximum strain occurred at the location between the 16th and 17th LED targets, which is the location of the top edge of the 4 in. x 4 in. steel loading tube. The local FRP strain maxima tend to occur at or near the mortar joints where the masonry flexural cracks develop. The increase in strain below mid-height as the ultimate load reached is an indication of the rapid propagation of the IC debonding crack from the location of maximum moment towards the bottom of the wallette.

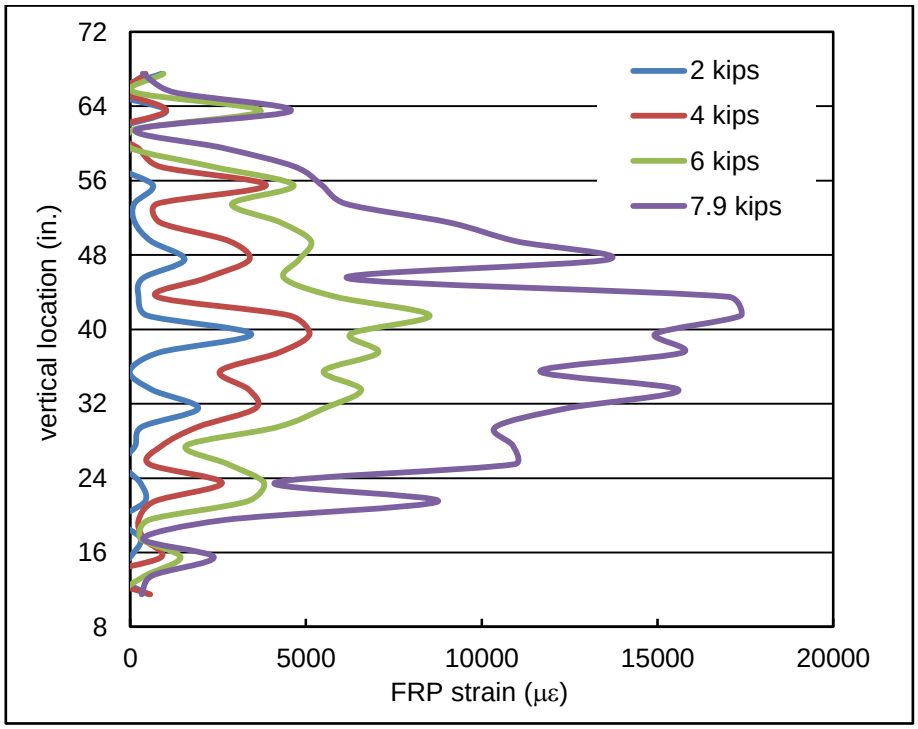

Figure 4.50 - FRP Strain Distribution of GD3

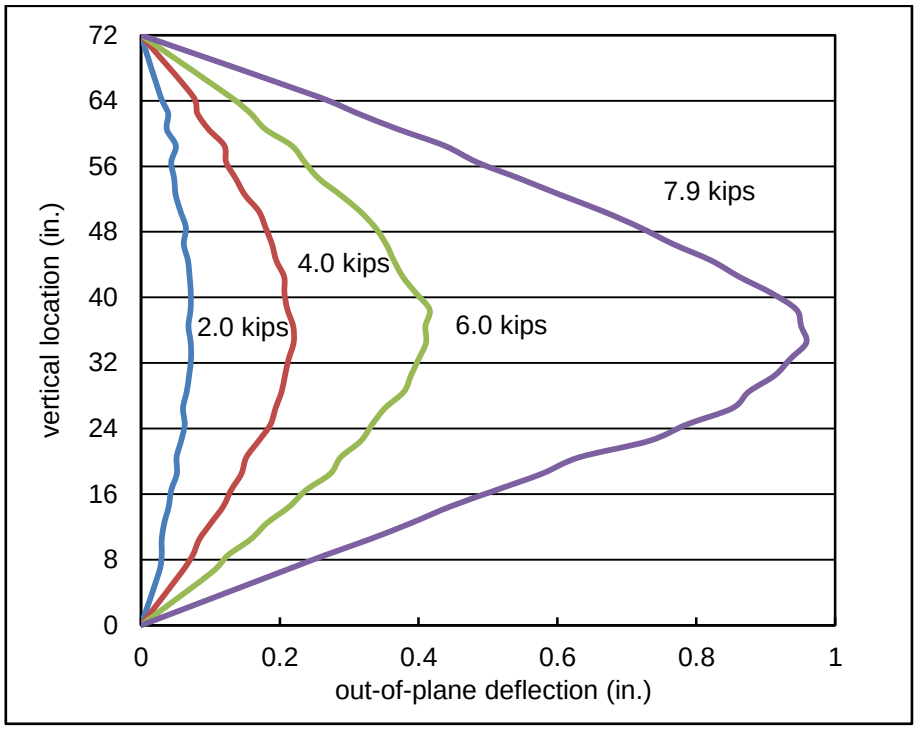

Figure 4.51 - Out-of-Plane Deflection of GD3

4.4. Summary of Experimental Results

All of the CFRP strengthened wallettes and GD3 failed by IC debonding, and the overall behavior was as expected. All of the single layer GFRP strengthened wallettes failed by FRP rupture, which is not expected. As described in Section 3.3.3, the one-layer GFRP laminate used in this experimental program has a wavy surface. The thickness of the thin part is just half of the thick part. As can be imagined, the thin part is very sensitive to the sharp edge of the cracks at mortar joints. While testing, stress will concentrate at the thin part, which consequently causes rupture for the one-layer GFRP strengthened wallettes. On the other hand, although the surface of two-layer GFRP laminate is also wavy, the thickness of the thin part is almost equal to the thick part of one-layer GFRP, which might be thick enough to prevent GFRP rupture. Table 4.1 summarizes the primary experimental results of each wallette.

Table 4.1 - Experimental results

Specimen	FRP Reinforcement Ratio (%)	Ultimate load (kips)	Maximum FRP strain (με)	Mid-Height Deflection (in.)	Failure Mode
Control	N.A.	4.5	N.A.	2.82	Flexure
CS3	0.077	8.8	8313	0.75	IC Debonding
CS6	0.154	11.0	6751	0.64	IC Debonding
CS8	0.204	13.0	5984	0.61	IC Debonding
CD3	0.154	10.1	7751	0.50	IC Debonding
GS3-1	0.066	6.0	13479	0.35	FRP Rupture
GS3-2	0.066	5.2	14172	0.55	FRP Rupture
GS6	0.133	6.5	11782	0.48	FRP Rupture
GD3	0.133	7.9	14936	0.95	IC Debonding

It should be noted that the FRP strain values given in Table 4.1 are the maximum recorded strain calculated using the OPTOTRAK data, which is the average strain over the 2 in. gage length, and the deflection is that corresponding to the maximum load. Also shown for reference in Table 4.1 is the FRP reinforcement ratio for each strengthened wallette, which is defined as the cross-sectional gross area ratio of the FRP and the wallette as given by the following

$$\rho_f = \frac{t_f b_f}{t_m b_m} \tag{4.1}$$

Although the load – mid-height deflection curve of each wallette is given individually in previous sections, Figure 4.52 shows a comparison of the load – mid-height deflection curves for all of the wallettes, including the control wall. As can be seen in Figure 4.52, the out-of-plane flexural capacity and post-cracking stiffness increased for all of the strengthening alternatives considered, with that of the CFRP strengthened wallettes being higher than the GFRP strengthened wallettes.

Further, the load carrying capacity and post-cracking stiffness of the strengthened wallettes are related to the reinforcement ratio of each FRP strengthening alternative. As shown in Figure 4.52, the wallette strengthened by a higher reinforcement ratio has a higher load carrying capacity and post-crack stiffness. It is also interesting to note that the wallettes strengthened by the same reinforcement ratio, CS6 and CD3, GS6 and GD3, have the same post-crack stiffness. Both CS6 and CD3 failed by FRP debonding, and the load carrying capacity of CS6 is a little higher than that of CD3. On the other hand, GS6 and GD3 showed different failure modes. GS6 failed by FRP rupture and GD3 failed by FRP debonding. Interestingly, the load carrying capacity of GD3 is 20% higher than that of GS6. The different failure mode was considered to be the main reason causing the variation of load carrying capacity.

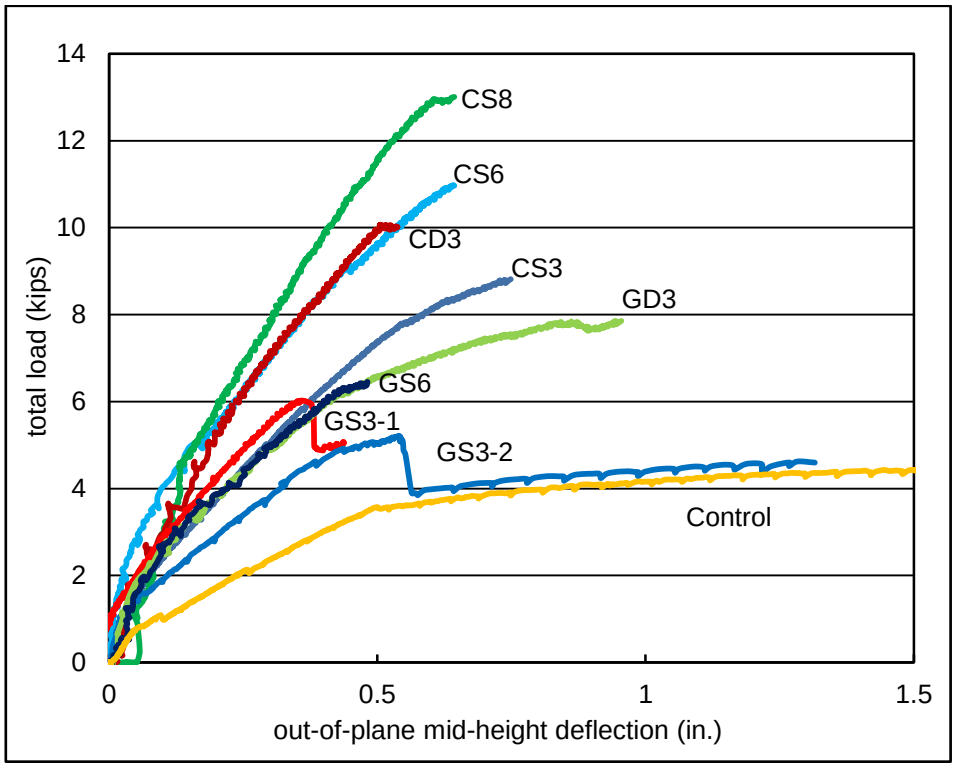

Figure 4.52 - Comparison of Load – Mid-height Deflection Curves

It can also be seen in Figure 4.52, although GS3-1 and GS3-2 were strengthened by same GFRP strengthening alternative, they show different behaviors in load carrying capacity. While the maximum recorded FRP strain is slightly less for GS3-1 compared to that of GS3-2, the load carrying capacity and the initial stiffness of GS3-1 is much higher. In addition, the post-rupture load carrying capacity of GS3-1 and GS3-2 should be equal to the load carrying capacity of the control wallette. However, the flexural strength of GS3-1 after FRP rupture is higher than that of GS3-2 and the control wallette, while the flexural strength of GS3-2 after FRP rupture is the same as the control wallette. The location of the internal

steel reinforcing bar was considered as the main reason causing the difference in load carrying capacity.

After testing, some of the masonry and grouted concrete core were removed from the wallettes to observe the condition of the cross-section at the maximum moment region and to measure the actual location of the internal steel reinforcing bar. The location of the steel reinforcing bar for GS3-1 is shown in Figure 4.53.

Figure 4.53 - Location of Steel Reinforcing Bar in GS3-1

Although the steel reinforcing bar was intended to be located at the center of the cross-section, it was observed that the reinforcing bar was closer to the tension face in GS3-1 and was closer to the compression face in GS3-2. This was considered to be the main reason for the variation in load carrying capacity and the initial stiffness. The measured location of the steel reinforcing bar at the mid-height for each wallette, from the center of the steel reinforcing bar to the tension face, is shown in Table 4.2. It should be noted that the design location was intended to be 4 in.

Table 4.2 - Measured Location of steel reinforcing bar from tension face

specimen	**location (in.)**
Control	4.44
CS3	4.44
CS6	4.81
CS8	4.38
CD3	4.56
GS3-1	***3.06***
GS3-2	***4.31***
GS6	4.19
GD3	4.06

4.5. Comparison of Strain Distribution

In order to determine the effects of different parameters, comparisons of strain distribution at failure of selected strengthened wallettes are discussed in this section. The following parameters are considered in the comparison: (1) width of the FRP laminate; (2) number of layers (FRP thickness).

4.5.1 Comparison of One Layer Strengthened Wallettes

For illustrative purposes, a comparison of the strain distribution at failure of the single layer CFRP strengthened wallettes is shown in Figure 4.54. All of the three wallettes failed by FRP IC debonding, and the strain distribution shows similar shape at the mid-height region. These three wallettes generally exhibit a decrease in strain near mid-height with a corresponding increase of FRP width, which is consistent with Chen & Teng (2001).

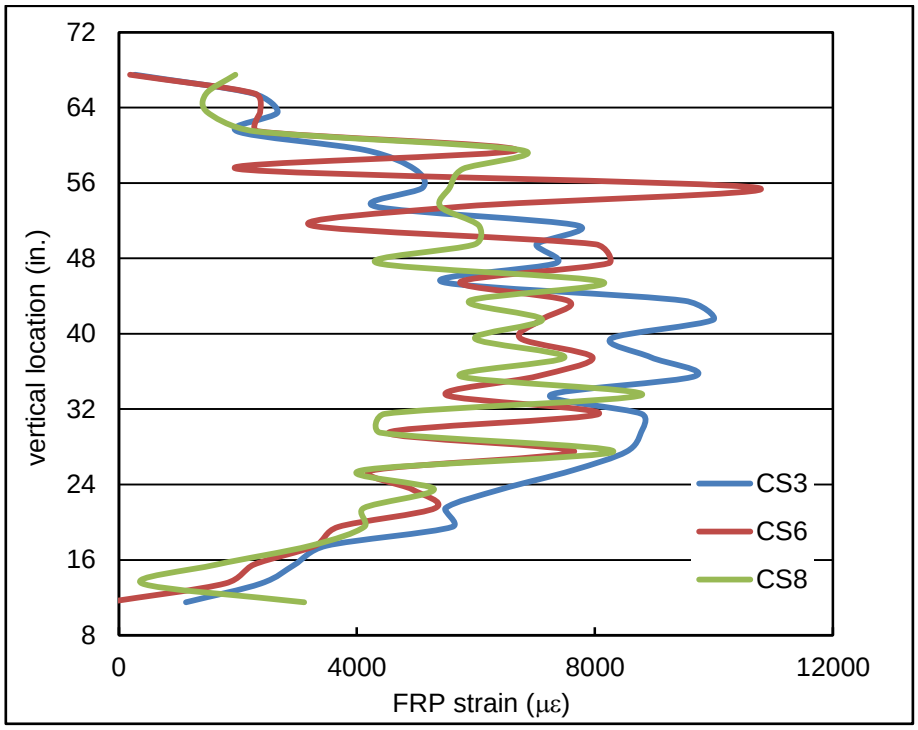

Figure 4.54 - Comparison of Strain Distribution of Single Layer CFRP

Figure 4.55 shows the comparison of strain distribution of single layer GFRP strengthened wallettes. All of the three wallettes failed by GFRP rupture at mid-height. The maximum strain of each wallette occurred at the mid-height mortar joint, and the maximum strain is much higher than the strain at other areas. Further, the strain distribution generally shows a decrease in strain at mid-height with a corresponding increase of FRP width. The strain distribution of GS3-1 and GS3-2 is similar, both of which exhibit an extreme concentration at mortar joints.

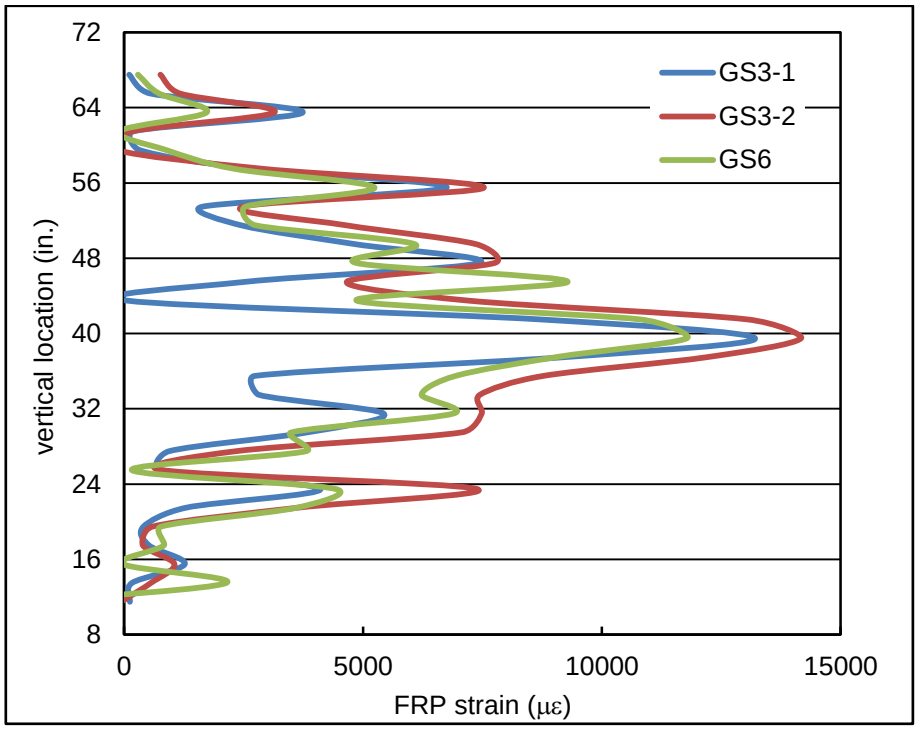

Figure 4.55 - Comparison of Strain Distribution of Single Layer GFRP

4.5.2. Influence of number of FRP layers

The influence of CFRP width on strain distribution can be seen by the comparison between CS3 and CD3, which is shown in Figure 4.56. Both CS3 and CD3 failed by FRP debonding. As can be seen in Figure 4.54, both wallettes exhibit a typical strain distribution associated with debonding. The maximum strain occurred at the location of maximum moment. The strain of CS3 is higher than that of CD3 at the same location, which is also consistent with most existing models, such as Chen & Teng (2001), CNR_200 (2004), Said & Wu (2008) and ACI 440.2R-08.

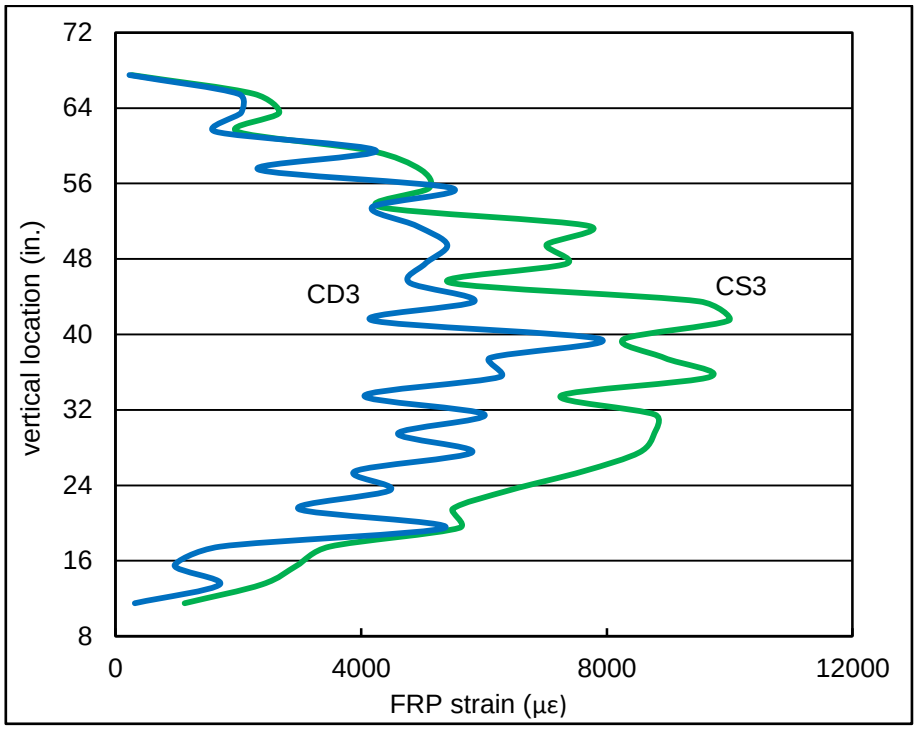

Figure 4.56 - Comparison of Strain Distribution of CS3 and CD3

The influence of GFRP thickness on strain distribution can be seen by the comparison of GS3-1, GS3-2 and GD3, which is shown in Figure 4.57. The strain distribution shows two different shapes due to the different failure modes. GS3-1 and GS3-2 exhibit extreme strain concentration at mortar joints, while GD3 has a more uniform strain distribution between mortar joints. The maximum strain occurred at the location of maximum moment. The mid-height strain of GD3 is slightly higher than GS3-1 and GS3-2. Typically, GD3 has a higher strain than GS3-1 and GS3-2.

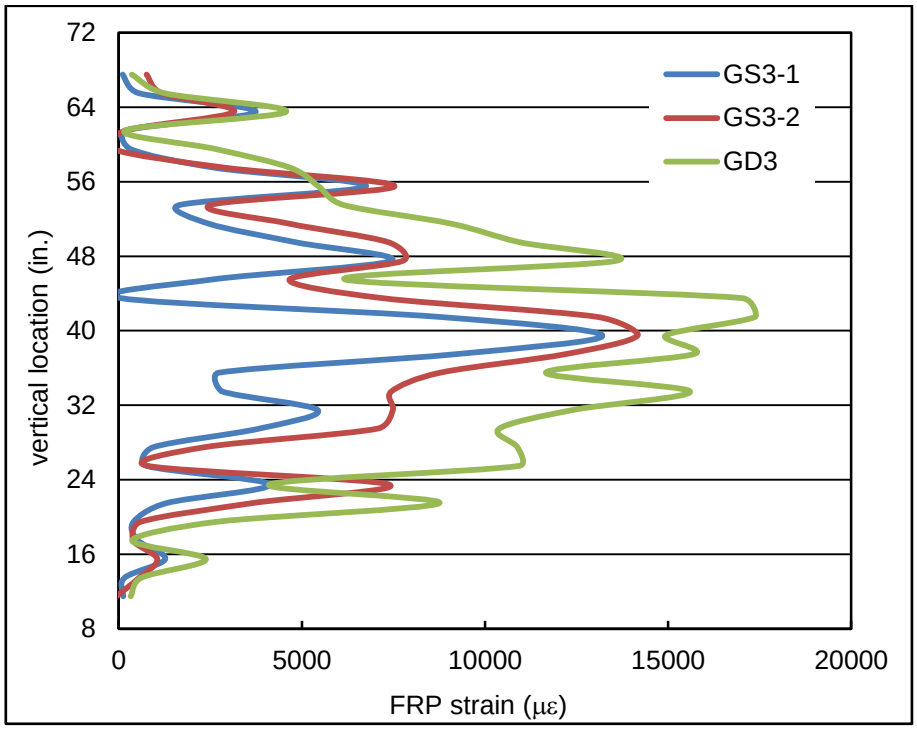

Figure 4.57 - Comparison of Strain Distribution of 3 in. wide GFRP

Chapter 5 SECTIONAL ANALYSIS

This chapter presents the debonding strain predicted by five different models, which were shown in Chapter 2. The prediction of each model is then compared with the experimental data measured. In addition, the layer-sectional analysis approach is used to calculate the theoretical moment capacity and moment-curvature relationship of each strengthened wallette. All the material properties used in the calculation are from the material tests presented in Chapter 3. The comparison between the theoretical and experimental moment capacity is shown, and finally, simplified design recommendations are presented.

5.1. Comparison of Existing IC Debonding Models

According to the experimental results, IC debonding is the dominate failure mode for the 2-layer GFRP strengthened and all CFRP strengthened CMU wallettes. Consequently, the accuracy of IC debonding strain predictions is critical to calculate the moment capacity of FRP strengthened wallettes in a design procedure. To predict the IC debonding strain, five existing models are considered. All five models are previously described in Chapter 2, including ACI 440.7R (2010), CNR_200 (2004), Said & Wu (2008), Chen & Teng (2001) and ACI 440.2R (2008). Table 5.1 summarizes the ratio of predicted debonding strain to the experimental debonding strain, which is previously shown in Table 4.1. It should be noted

that the experimental debonding strain is the maximum strain measured by the OPTOTRAK system. Values greater than 100% indicate an over-prediction of the debonding strain.

Table 5.1 - Ratio of predicted to experimental debonding strain

	$\varepsilon_{IC\_predicted} / \varepsilon_{IC\_experimental}$				
	ACI 440.7R (2010)	CNR_200 (2004)	Chen & Teng (2001)	Said & Wu (2008)	ACI 440.2R (2008)
CS3	65.0%	16.0%	68.7%	92.4%	68.9%
CS6	80.0%	19.7%	84.6%	**113.8%**	84.8%
CS8	90.2%	22.3%	95.5%	**128.4%**	95.7%
CD3	70.0%	12.3%	52.9%	78.6%	48.1%
GS3-1	73.4%	22.5%	96.6%	**101.5%**	96.8%
GS3-2	69.9%	21.4%	91.9%	96.5%	92.1%
GS6	84.0%	25.8%	**110.6%**	**116.1%**	**110.8%**
GD3	66.3%	14.6%	62.5%	72.5%	59.0%
AVG.	**74.8%**	**19.3%**	**82.9%**	**100.0%**	**82.0%**
S.D.	**9.0%**	**4.6%**	**19.7%**	**19.1%**	**21.4%**

As described in Chapter 2, among the five selected existing models, Said & Wu (2008), Chen & Teng (2001) and ACI 440.2R (2008) are derived for concrete members. As a consequence, some modifications are needed in the calculation. As can be seen in Equations 2.20, 2.24, and 2.25, all three models use the compressive strength of concrete, f_c'. In

addition, it is well known that the FRP bonding strength is mainly affected by the tensile strength of the substrate, and that the tensile strength of concrete masonry is directly related to the compressive strength of individual CMU instead of that of the masonry prism. So in the current calculation, f_c' is replaced by the compressive strength of individual CMU. According to ACI 440.7R-10, the ultimate FRP rupture strain ε_{fu}^* used in Equation 2.12 is the value provided by the manufacturer, which are previously summarized in Table 3.1. As mentioned by the manufacturer, the provided FRP properties are statistically based and can be used for design without further reduction. Figure 5.1 shows the comparison of predicted and experimental debonding strain. The points below the equality line in Figure 5.1 indicate a safe prediction of debonding strain.

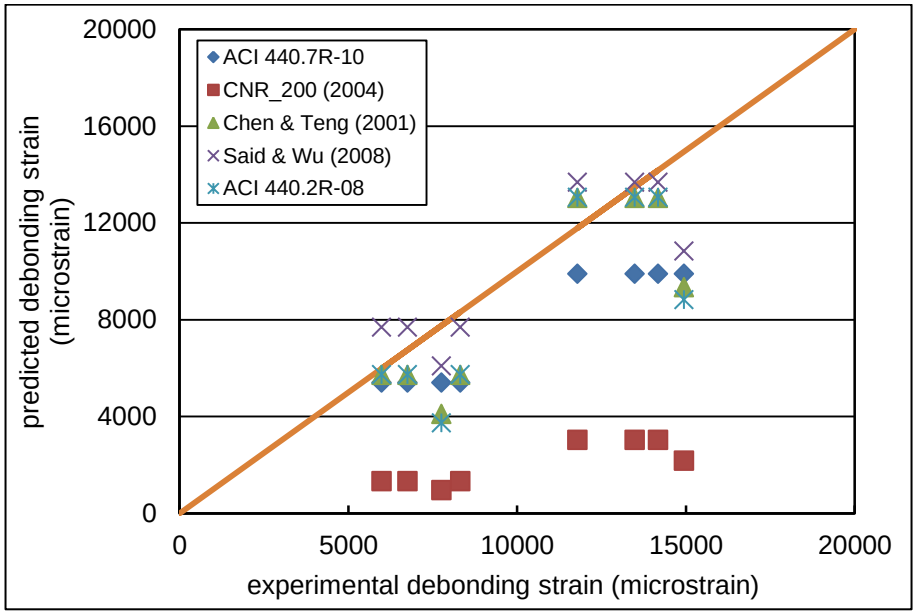

Figure 5.1 - Comparison of Predicted and Experimental Debonding Strain

As shown in the Table 5.1 and Figure 5.1, CNR_200 (2004) gives a much lower predicted strain than the other models. This is consistent with the observation in Chapter 2 that the CNR_200 (2004) is not suitable for CMU wallettes. Further, Chen & Teng (2001) and ACI 440.2R-08 give similar predicted debonding strain, both of which over-predict the ultimate strain of GS6, and both models provide excessively conservative predicted debonding strain of the two-layer FRP strengthened wallettes, CD3 and GD3. In addition, Said & Wu (2008) gives the highest predicted ultimate strain than the other models, and some of the predicted strain is much higher than the experimental result. So, Said & Wu (2008) is not safe for design. Conversely, ACI 440.7R-10 gives conservative predictions, all of which are lower than the experimental data. Hence, ACI 440.7R-10 is safe for design of the FRP strengthened wallettes. It should be noted that ACI 440.7R-10 provides a limit on the total force per unit width that the FRP system transfers to the CMU substrate, as described in Equation 2.14. The calculated P_{fm} are summarized in Table 5.2. As can be seen in Table 5.2, the transferred forces per unit width of CFRP and 2-layer GFRP are beyond the limit. Hence, the limit is very conservative and ACI 440.7R-10 is validated for CFRP strengthened steel reinforced CMU wallettes.

Table 5.2 – Transferred force per unit width

FRP system	Calculated P_{fm} (lb./in.)
1-layer CFRP	2160
2-layers CFRP	4320
1-layer GFRP	1220
2-layers GFRP	2160

As previously described for the Chen & Teng (2001) model, a lower limit of 0.33 is given for the width ratio, b_p/b_m. However the width ratio of all the strengthened wallettes is lower than this limit. Consequently, b_p/b_m is set equal to 0.33 for all the strengthened wallettes when using the Chen & Teng (2001) model, which provides lower values of the width ratio coefficient, β_p, and hence predicted debonding strain, ε_{IC}. Since for FRP-strengthened CMU walls the width ratio is commonly expected to be lower than 0.33, the limit is not enforced in this calculation of FRP strengthened steel reinforced CMU wallettes. Table 5.3 shows the ratio of predicted debonding strain, calculated using the Chen & Teng (2001) model without the limit of width ratio, to the experimental data.

Table 5.3 – Ratios of predicted to the experimental debonding strain using the Chen & Teng (2001) model without limit of width ratio

Wallette	$\varepsilon_{IC\_predictd}/\varepsilon_{IC\_experimental}$
CS3	79.3%
CS6	89.7%
CS8	95.7%
CD3	61.0%
GS3-1	**111.6%**
GS3-2	**106.1%**
GS6	**117.2%**
GD3	72.1%

As can be seen in Table 5.3, without considering the limit on the width ratio, the Chen & Teng (2001) model gives a better prediction which is still safe but more accurate for the wallettes that failed by IC debonding, while it over-predicts for the wallettes that failed by FRP rupture.

5.2. Layered-Sectional Analysis

To investigate the moment-curvature response of each wallette, a layered-sectional analysis was developed. The moment-curvature relationship is then compared with the test data to verify the effect of various parameters. The details of the analysis procedure, and the comparison of result, are shown in this section.

5.2.1. Layered-sectional analysis procedure

Strain compatibility and equilibrium of forces are used in the layered-sectional analysis to calculate the strengthened wallette flexural capacity and full moment-curvature relationship. The calculation follows a simple trial-and-error procedure. Figure 5.2 illustrates the typical strain and stress distributions, and the resultant forces along the height of a unit wide FRP-strengthened CMU section.

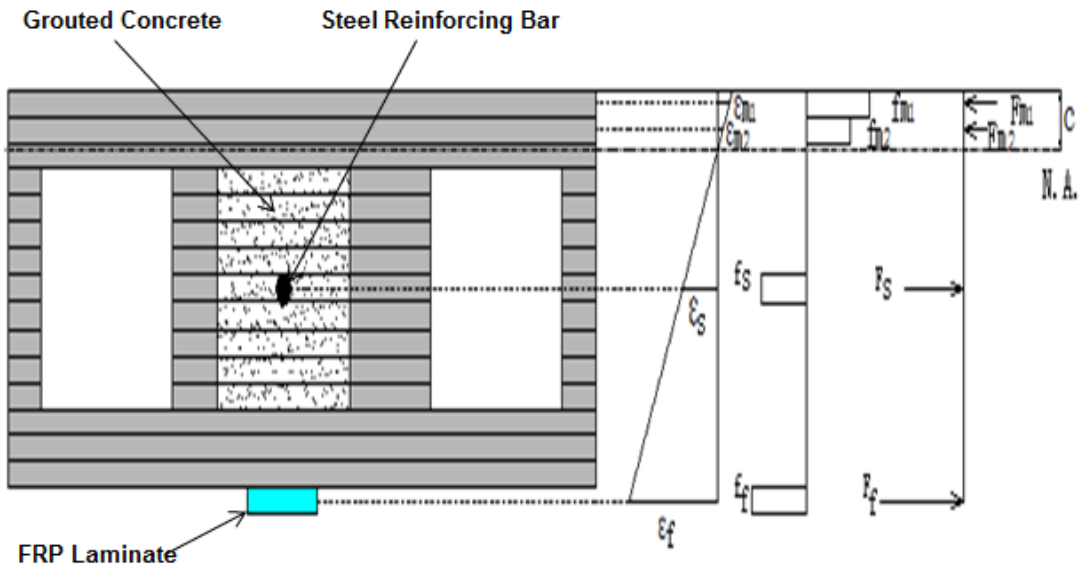

Figure 5.2 - Layered-Sectional Analysis

As can be seen in Figure 5.2, in a typical layered-sectional analysis procedure, the cross-section is firstly discretized into a number of thin layers. Similar to a finite element model,

the thinner the layers, the more accurate the analysis result is. It should be noted that the steel reinforcing bar and the FRP laminate are considered their own layer acting through the centroid of their cross-section, rather than coinciding with a particular CMU layer. According to the test results, all failure modes were governed by the FRP for all of the strengthened wallettes. So, the layered-sectional analysis starts by selecting a strain in the FRP laminate. Due to strain compatibility, the strains in the cross-section are directly proportional to the distance from the neutral axis. Consequently, by assuming the location of the neutral axis for a selected FRP strain, the strain profile along the cross-section can be obtained. Because of the wide width of the wallette, in most cases, the neutral axis is in the flange of the CMU. The analysis method also assumes that there is no relative slip between any two components before failure occurs, such as the FRP laminate and the CMU substrate, as well as the grouted concrete and the steel reinforcing bar. Hence, the strain in the steel reinforcing bar is the same as the strain in the concrete at that layer.

Once the strain profile is defined, the stress in each layer can be determined. Since the layers are very thin, the strain used in the calculation is the average strain corresponding to the centroid of that layer, and the stress is assumed to be constant over the depth of that layer. As shown in Figure 5.2, the stress distribution along the cross-section is a series of straight line segments. Since the depth of each layer is very small, this assumption is believed to be reasonable. By multiplying the stress of each layer with the cross-sectional area of that layer, the resultant force through the centroid of that layer can be calculated. It should be noted that the tensile strength of the CMU and grouted concrete is ignored in the analysis. Equilibrium

of internal forces can then be checked. The location of the neutral axis can be determined by trial-and-error until the summation of compressive and tensile forces is equal to zero, since there is no axial load in the wallettes tested. Once force equilibrium is satisfied, the moment and curvature can be determined at that selected strain in the FRP laminate. By incrementally increasing the level of FRP strain, the full moment-curvature relationship can be determined for the strengthened wallette.

It should be noted that several things must be checked carefully when equilibrium is checked. This includes the location of the neutral axis. Since the neutral axis is initially assumed to be in the CMU flange, the compressive stress in the grouted concrete core is zero. However, compressive forces will be distributed in the grouted concrete core if the neutral axis is located in the web. In addition, the strain in the steel reinforcing bar should also be check in order to determine if the steel reinforcement yields. The steel reinforcing bar may not yield at failure when FRP failure controls at a very low strain. In this case, the stress of the reinforcing bar is lower than the yield stress and should be calculated using an elastic stress-strain relationship. On the other hand, if the FRP system fails at a high strain and the steel reinforcing bar is located closer to the tension face of the wallette, the reinforcing bar strain might be in the strain hardening region. To illustrate the layered-sectional analysis process, a flow chart of the procedure is shown in Figure 5.3.

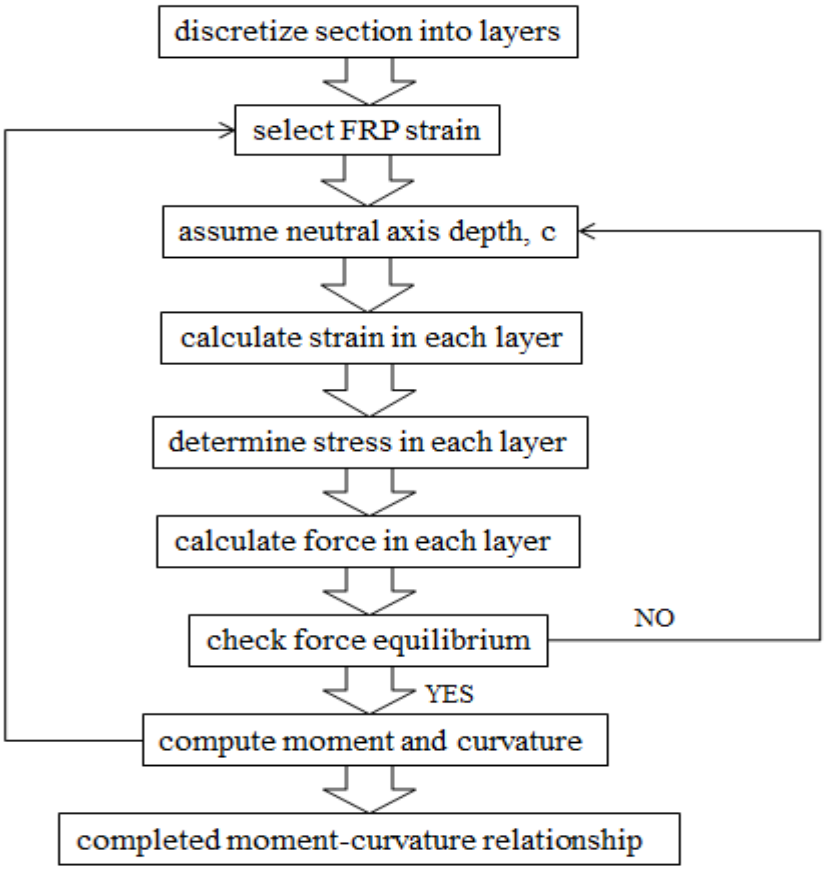

Figure 5.3 - Flow Chart of Layered-Sectional Analysis

5.2.2. Compressive stress – strain behavior of CMU

Since the neutral axis in the layered-sectional analysis is typically in the masonry flange, the compressive stress-strain curve of the CMU has a significant effect on the analysis results. As described in Chapter 2, there are two typical models to calculate compressive stress

distribution in CMU: linear elastic approach, and rectangular stress block approach. Hence, two different stress-strain models were taken into consideration in this research.

Priestley and Elder (1983) tested CMU prisms at a low strain rate of 0.000005/second, and presented a typical stress-strain relationship for CMU, which is derived from modified the Kent-Park model presented by Park and Priestley (1982). The stress-strain curve presented by Priestley and Elder (1983) is selected as Model 1. In addition, Velazquez-Dimas and Ehsani (2000) considered CMU as a linearly elastic material up to failure. The linear stress-strain relationship is expressed as Model 2. Since the CMU and grouted concrete are considered as two different materials and discretized into separate layers in the layered-sectional analysis, the specified compressive strength of CMU, f'_m, and the ultimate compressive strain of CMU, ε_{mu}, are measured by the ungrouted prism tests. The models are given from Equation 5.1 to Equation 5.3. Figure 5.4 shows the curves of the two models and the average stress-strain curve measured from the ungrouted CMU prisms which are previously shown in Figure 3.23.

Model 1:

$\varepsilon_m < 0.0015$

$$f_m = 1.067 \times f'_m \left[2\left(\frac{\varepsilon_m}{0.002}\right) - \left(\frac{\varepsilon_m}{0.002}\right)^2\right] \quad (5.1)$$

$\varepsilon_m \geq 0.0015$

$$f_m = f'_m \left[1 - \frac{\varepsilon_m - 0.0015}{0.003}\right] \quad (5.2)$$

Model 2:

$$f_m = \frac{f'_m}{\varepsilon_{mu}} \times \varepsilon_m \tag{5.3}$$

where f_m and ε_m are the compressive stress and strain in the CMU, respectively, f'_m and ε_{mu} are the ultimate compressive strength and strain of the CMU, which are taken as 1.39 ksi and 0.003 in./in., respectively, according to the ungrouted prism compression tests presented in Section 3.3.5.

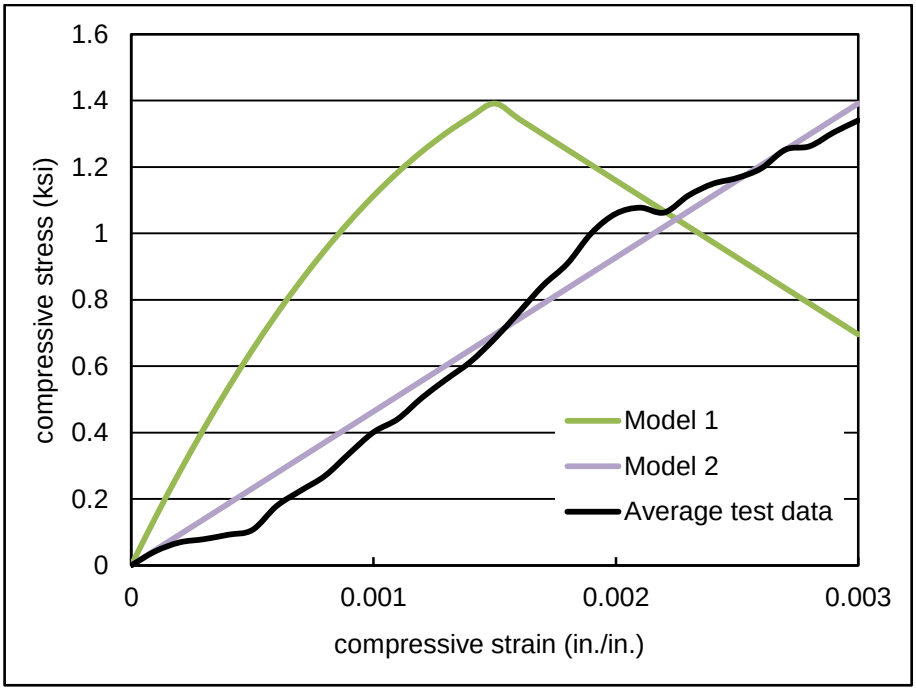

Figure 5.4 - Stress-Strain Relationship of the Selected Models

In addition, when the neutral axis is located in the web of the CMU, the grouted concrete core will also be in compression. For this case, a typical parabolic stress-strain curve for concrete was used, as shown in Equation 5.4.

$$\frac{f_c}{f_c'} = 2\left(\frac{\varepsilon_c}{\varepsilon_c'}\right) - \left(\frac{\varepsilon_c}{\varepsilon_c'}\right)^2 \tag{5.4}$$

where f_c' is the compressive strength of the grouted concrete, which is taken as 4150 psi according to concrete cylinder tests presented in Section 3.3.1, ε_c' is taken as 0.002, and f_c and ε_c is the compressive stress and strain in the grouted concrete, respectively.

Both of the CMU compressive stress-strain models were used in the layered-sectional analysis. Table 5.4 summarizes the ratio of predicted moment capacity to the experimental moment capacity. It should be noted that the FRP strain used in the calculation is the maximum FRP strain measured by the OPTOTRAK system, which are previously summarized in Table 4.1. As can be seen in Table 5.4, Model 1 and Model 2 give similar prediction of the moment capacity. Due to the limited number of wallettes, it is hard to determine which model is better.

Table 5.4 - Ratios of layered-sectional analysis predicted to the experimental moment capacity

Wallette Series	Model 1	Model 2
Control	79.1%	79.2%
CS3	91.7%	82.2%
CS6	86.1%	78.2%
CS8	86.3%	78.4%
CD3	**108.5%**	100.0%
GS3-1	**114.0%**	**112.4%**
GS3-2	**101.9%**	**100.6%**
GS6	99.1%	97.2%
GD3	89.9%	90.7%
Average	**97.2%**	**92.7%**
S.D.	**10.4%**	**12.5%**

The ultimate moment and corresponding curvature, which are calculated using Model 1, are summarized in Table 5.5. In addition, a comparison of the complete moment-curvature calculated using Model 1 curves of each wallette is shown in Figure 5.5. Further, Table 5.6 shows the ultimate moment and corresponding curvature calculated using Model 2. And the comparison of the complete moment-curvature curves calculated using Model 2 of each wallette is shown in Figure 5.6.

Table 5.5 - Ultimate moment and curvature calculated using Model 1

Wallette	predicted curvature (in^{-1})	predicted moment $(kips \cdot ft.)$	experimental moment $(kips \cdot ft.)$
Control	0.00335	4.75	6.02
CS3	0.00132	10.8	11.7
CS6	0.00109	12.6	14.7
CS8	0.00099	14.9	17.3
CD3	0.00127	14.6	13.5
GS3-1	0.00204	9.12	8.00
GS3-2	0.00214	7.07	6.93
GS6	0.00181	8.59	8.67
GD3	0.00231	9.47	10.5

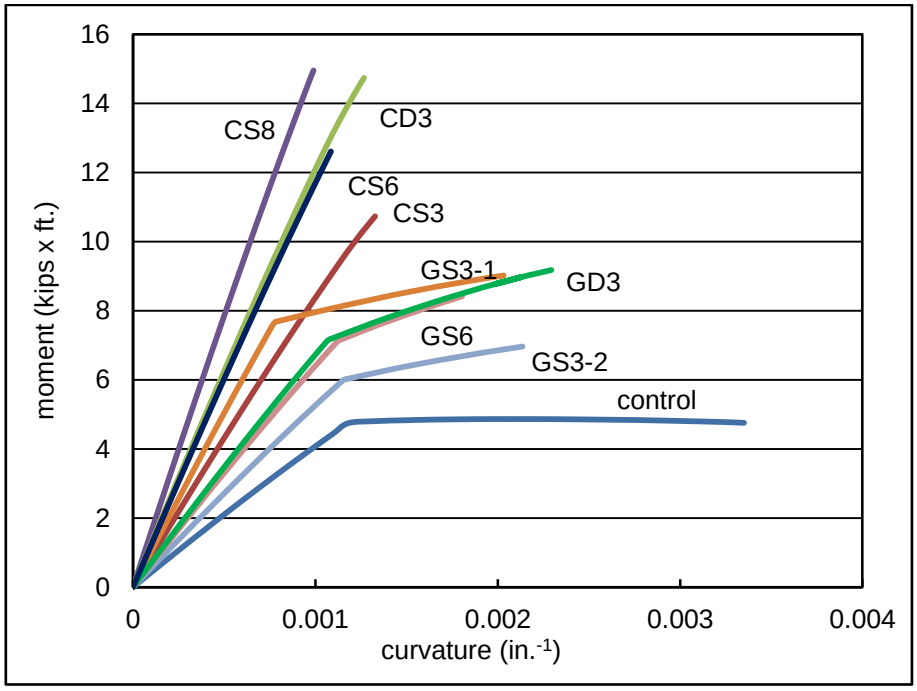

Figure 5.5 - Comparison of Predicted Moment-Curvature Curves Using Model 1

Table 5.6 - Ultimate moment and curvature calculated using Model 2

Wallette	predicted curvature (in^{-1})	predicted moment $(kips \cdot ft.)$	experimental moment $(kips \cdot ft.)$
Control	0.00249	4.76	6.02
CS3	0.00141	9.64	11.7
CS6	0.00117	11.5	14.7
CS8	0.00106	13.6	17.3
CD3	0.00134	13.5	13.5
GS3-1	0.00216	8.99	8.00
GS3-2	0.00226	6.97	6.93
GS6	0.00193	8.43	8.67
GD3	0.00240	9.56	10.5

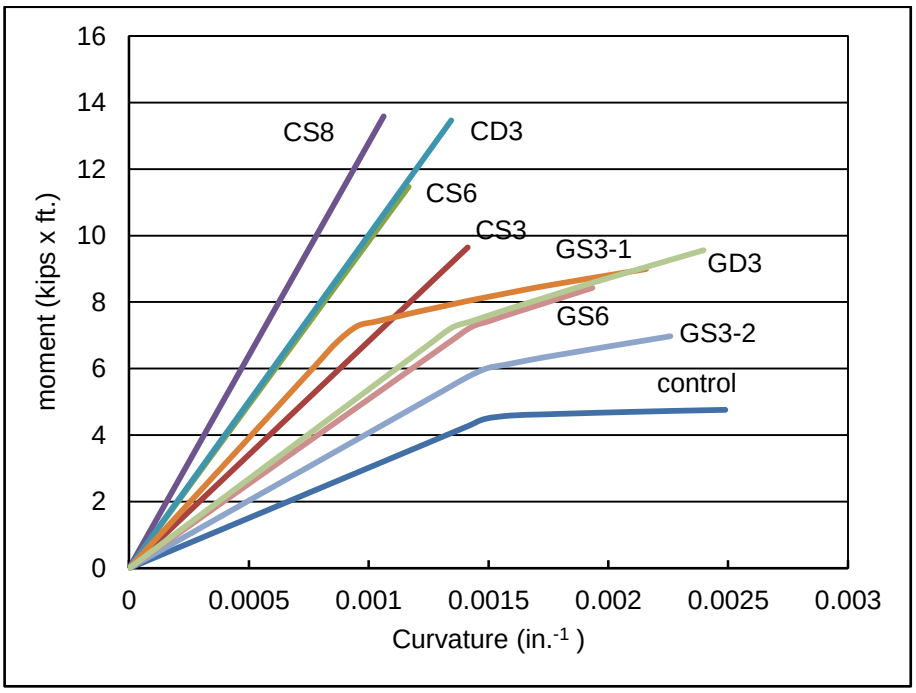

Figure 5.6 - Comparison of Predicted Moment-Curvature Curves Using Model 2

As expected, no matter which model is used in the calculation, the wallettes strengthened using the same amount of FRP have similar stiffness, which is confirmed by the curves of CS6 and CD3, as well as that of GD3 and GS6. The higher stiffness of GS3-1, compared to GS3-2, is due to the location of the internal steel reinforcing bar. It should be noted that the maximum FRP failure strain used in the calculation of moment-curvature is the maximum measured strain by the OPTOTRAK system, as shown in Table 4.1.

For illustrative purposes, a comparison of moment-curvature curves calculated using Model 1 and Model 2 is shown in Figure 5.7. The solid lines show the moment-curvature curves calculated using Model 1, while the dashed lines show the moment-curvature curves calculated using Model 2. As can be seen in Figure 5.7, Model 1 provides a higher stiffness than Model 2.

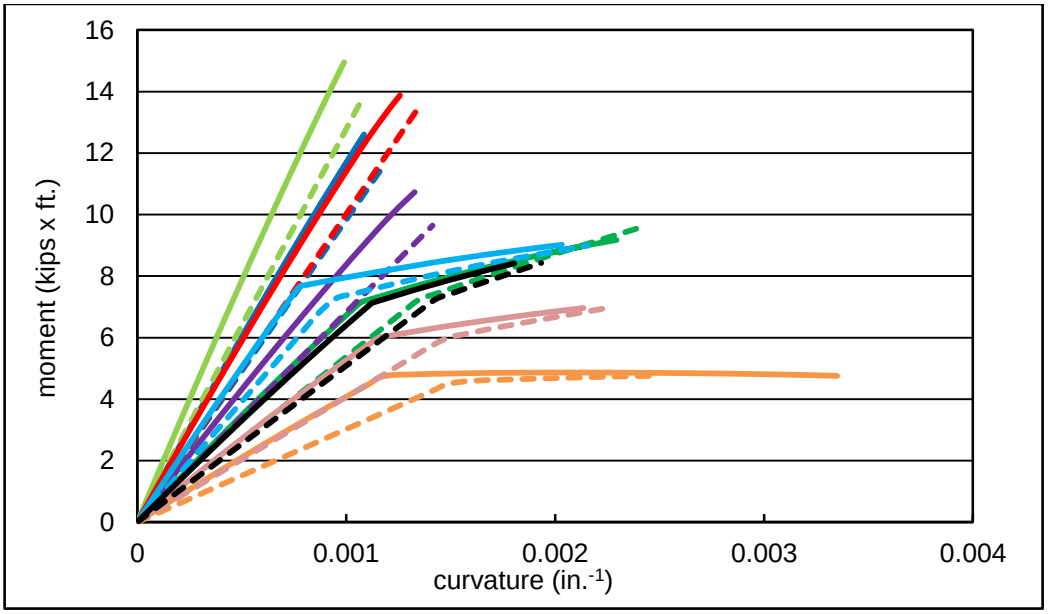

Figure 5.7 - Comparison of Moment-Curvature between Model 1 & 2

5.3. Design Procedure

As can be seen in Section 5.2, the layered-sectional analysis can provide a good prediction of the moment capacity of FRP strengthened steel reinforced CMU wallettes. However, it is not well suited for design. Hence, a simplified design approach based on a sectional analysis is presented in this section.

5.3.1. Basic Assumptions

This design procedure follows the same basic assumptions used in FRP strengthened unreinforced CMU walls, including:

- A plane section before loading remains plane after loading;
- The tensile strength of CMU and the compressive strength of FRP are neglected;
- The tensile behavior of FRP is linear elastic up to failure;
- The reinforcing steel is elastic-perfectly plastic; and
- There is no relative slip between any two materials until failure occurs, such as FRP and CMU, steel reinforcing bar and grouted concrete.

5.3.2. Design Recommendations

According to the experimental results of the wallette tests, the failure mode for FRP strengthened steel reinforced CMU walls is governed by FRP debonding, and limited by FRP rupture. Based on the discussion in Section 5.2.2, the layered-sectional analysis approach confirmed that both Model 1 and Model 2 are suitable to simulate the compressive stress-

strain relationship of CMU. Hence, both the linear elastic compressive stress-strain relationship and an idealized rectangular stress block were used in the proposed design approach. When debonding controls, the extreme CMU compressive strain is generally less than 0.003. So, detailed expressions for γ and β_1 are needed to define the idealized rectangular stress block. As previously described in Chapter 2, Tumialan & Galati (2003) and Galati & Garbin (2005) provide different expressions to calculate γ and β_1. The expressions are described in Equation 2.5 to Equation 2.8. Since FRP rupture is also a typical failure mode based on the test results, the Chen & Teng (2001) model without the limit of width ratio is not used in the design procedure, even though it provides good prediction of debonding strain. ACI 440.7R.-10 gives conservative prediction for both debonding strain and rupture strain. So ACI 440.7R-10 is recommended for use in the design procedure. The design procedure is based on a trial-and-error method. Figure 5.8 shows a flow chart of the design procedure. The calculated moments capacity compared to the experimental results are summarized in Table 5.8.

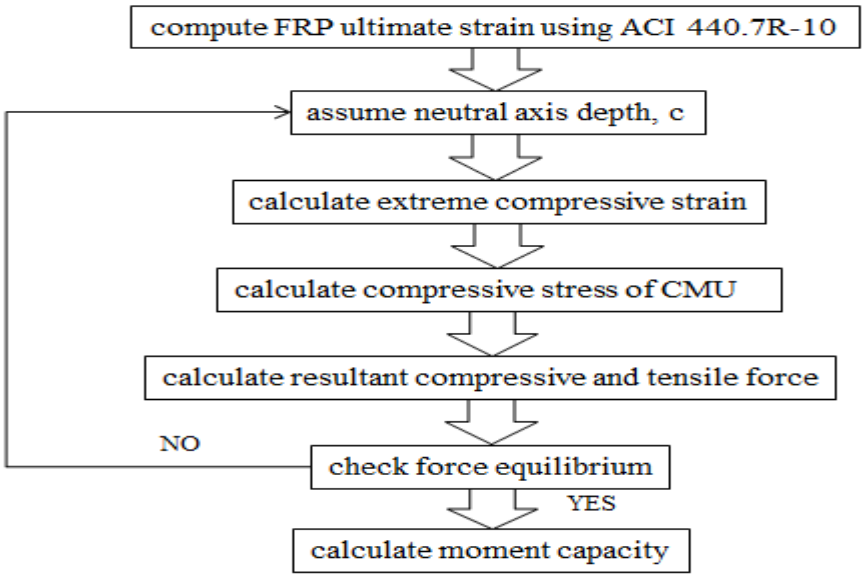

Figure 5.8 - Flow Chart of Design Procedure

Table 5.7 - Calculated moment capacity and experimental result

	Tumialan & Galati (2003) (kips x ft.)		Galati & Garbin (2005) (kips x ft.)		Linear elastic approach (Equation 5.3) (kips x ft.)		Experimental result (kips x ft.)
control	4.77	79.2%	4.85	80.5%	4.76	79.1%	6.02
CS3	7.34	62.7%	7.37	63.0%	6.30	53.8%	11.7
CS6	10.3	70.2%	10.3	70.4%	9.23	62.8%	14.7
CS8	13.7	79.3%	14.0	81.1%	12.4	71.5%	17.3
CD3	10.6	78.6%	10.5	77.5%	9.4	69.9%	13.5
GS3-1	8.63	107.8%	8.47	105.9%	8.35	104.4%	8.0
GS3-2	6.49	93.6%	6.33	91.3%	6.21	89.7%	6.93
GS6	8.09	93.3%	7.85	90.5%	7.81	90.0%	8.67
GD3	8.25	78.6%	7.94	75.6%	7.96	75.8%	10.5
AVG(%)	**82.6%**		**81.2%**		**77.4%**		
S.D.(%)	**13.6%**		**12.7%**		**15.4%**		

As illustrated in Table 5.8, the predicted moment capacity is lower than the test results, which means the method is reasonably conservative and safe in design. ACI 440.7R-10 is recommended to use in design to predict the FRP strain. In addition, Tumialan & Galati (2003), Galati & Garbin (2005), and the linear elastic approach give similar prediction of the calculated moment capacity. Since failure of the FRP strengthened steel reinforced CMU wallettes is governed by the FRP and the neutral axis is generally located within the CMU flange, the specific compressive stress-strain relationship of the CMU has little effect on the moment capacity prediction. For design purposes, it is up to the designer to decide what the most appropriate model is to use for specific CMU material.

Chapter 6 CONCLUSIONS

This chapter provides a summary of the research program that investigated the behavior of fiber-reinforced polymer strengthened steel reinforced concrete masonry wallettes in out-of-plane bending conducted at the Constructed Facilities Laboratory (CFL), at North Carolina State University (NCSU) in Raleigh, NC. Analysis and design recommendations are made based on the experimental results.

This research project creates the first database of steel reinforced CMU wallettes strengthened with externally bonded FRP systems subject to out-of plane bending. The test series comprising nine steel reinforced CMU wallettes loaded in three-point out-of-plane bending was undertaken, eight of which were strengthened with either Glass or Carbon externally bonded FRP systems using the wet lay-up technique. Two failure modes were observed: IC debonding and FRP rupture. All of the CFRP strengthened wallettes and GD3 failed by IC debonding, and all of the single layer GFRP strengthened wallettes failed by FRP rupture. All the strengthened wallettes exhibited an increase in load carrying capacity and post-cracking stiffness compared to that of the unstrengthened control wallette, with a corresponding reduction in out-of-plane displacement regardless of the failure mode.

6.1. FRP Strengthening System

The load carrying capacity and the post-cracking stiffness of the FRP strengthened wallettes are related to the reinforcement ratio of each FRP strengthened alternative. As expected, wallettes strengthened by a higher reinforcement ratio have a higher load carrying capacity and post-crack stiffness. Wallettes strengthened by the same reinforcement ratio have the same post-crack stiffness. In addition, the behavior of GS3-1 and GS3-2 shows clearly that the moment capacity of the FRP strengthened steel reinforced CMU wallettes is very sensitive to the location of the internal steel reinforcing bar.

In addition, even though the carbon and glass fibers used in this program have similar nominal thickness, the thickness of cured CFRP and GFRP laminate is different. The surface of the CFRP laminate is flat, however, the GFRP laminate has a wavy surface due to the fabric profile. The wavy surface causes a significant difference in laminate thickness at different points. As can be imagined, stress will concentrate at thin locations increasing the sensitivity to the sharp edge of a crack in a CMU wall. The stress concentration could be confirmed in Figures 4.34, 4.39 and 4.44, all of which show extreme strain concentration at mortar joints, where horizontal cracks occur. The stress concentration is considered as the main reason for all the single layer GFRP strengthened wallettes failing by a premature rupture of the GFRP. The double layer GFRP laminates address this problem, and the strengthened wallette failed by IC debonding with a higher moment capacity. It should be noted that GD3 and GS6 have similar stiffness. So when the FRP laminate has a wavy

surface, it may be more efficient to use two layers of narrow FRP rather than a wide single layer.

When the limit on the width ratio in the Chen & Teng (2001) model is not enforced, the model provides good predictions on the FRP debonding strain. However, the model over-predicts the FRP strain when FRP rupture occurs. CNR_200 (2004) is not suitable for FRP strengthened CMU wallettes. Said & Wu (2008) provides the highest prediction on FRP strain, and is not safe to use in design. ACI 440.7R-10 gives conservative prediction on FRP strain, no matter what the failure mode is. In addition, ACI 440.7R-10 is validated even though the total force per unit width that the FRP system transfers to the CMU substrate exceeds the limit shown in Equation 2.14.

The layered-sectional analysis provides good prediction of moment capacity of FRP strengthened steel reinforced CMU wallettes. In the analysis, the calculated moment capacity is safe but accurate no matter which model is used for the compressive stress within the CMU cross-section. Since the failure mode of FRP strengthened steel reinforced CMU walls is governed by FRP, and the depth of neutral axis is very small, the calculated moment capacity is not that sensitive to the CMU compressive stress-strain relationship.

6.2. Design Recommendations

Generally, the behavior of FRP strengthened steel reinforced CMU wallettes is governed by IC debonding. To calculate the moment capacity of the FRP strengthened steel reinforced CMU wallettes, the analysis procedure should efficiently start with the FRP debonding strain. ACI 440.7R-10, which is the design guide for FRP strengthened URM walls, provides good prediction of the FRP strain and is safe for design. Based on the experimental results and previous analysis, the compressive stress-strain curve of CMU does not have a significant effect on the calculated moment capacity. It is up to the designers to determine the most appropriate model to use for their specific CMU material.

The location of the neutral axis is then determined using a typical trial-and-error sectional-analysis method until internal force equilibrium is satisfied. For the wallettes considered, the average predicted moment capacity is above 75% of the experimental result. This method provides reasonable and safe predictions, and is suitable in design.

6.3. Future Work

Future work is still necessary in order to develop a better understanding of FRP strengthened steel reinforced CMU wallettes. Such future work should include:

1. Steel reinforced CMU wallettes strengthened with FRP wider than 8 in. should be tested. As can be seen in Table 5.1, the predicted strain by ACI 440.7R-10 is closer to the experimental measured strain when the width of FRP increases. When a wider FRP is used, the predicted strain might be beyond the experimental data, which means the ACI 440.7R-10 might not be suitable. In that case, the failure mode might also change.
2. More tests on steel reinforced CMU wallettes strengthened with different types of FRP, especially single layer GFRP, should be conducted to obtain a wider database and address the premature rupture failure observed.
3. Reinforced wallettes constructed using other kinds of masonry, such as clay bricks, should be strengthened and tested in order to generate a more robust database and design approach.
4. Strengthened wallettes should be tested under different boundary and load conditions in order to observe the potential for other possible failure modes.

REFERENCES

ACI Committee 440.2R, (2008). Guide for the Design and Construction of Externally Bonded FRP Systems for Strengthening Concrete Structures. *ACI 440.2R-08. American Concrete Institute*, Farmington Hills, Michigan, United States, 2008, 76 pp.

ACI Committee 440.7R, (2010). Guide for the Design and Construction of Externally Bonded Fiber-Reinforced Polymer Systems for Strengthening Unreinforced masonry Structures. *ACI 440.7R-10. American Concrete Institute*, Farmington Hills, Michigan, 2010, 50 pp.

Albert, M., and Elwi, A., & Cheng, J. (2001). Strengthening of Unreinforced masonry Walls Using FRPs. *Journal of Composites for Construction, Vol. 5, No. 2, May, 2001,* 76-84 pp.

ASTM A370-12a. (2012). Standard Test Methods and Definitions for Mechanical Testing of Steel Products. *American Society for Testing and Materials*, West Conshohocken, PA., United States.

ASTM C39-12a. (2012). Standard Test Method for Compressive Strength of Cylindrical Concrete Specimens. *American Society for Testing and Materials*, West Conshohocken, PA., United States.

ASTM C109-12. (2012). Standard Test Method for Compressive Strength of Hydraulic Cement Mortars (Using 2-in. or [50mm] Cube Specimens). *American Society for Testing and Materials*, West Conshohocken, PA., United States.

ASTM C140-13a. (2013). Standard Test Methods for Sampling and Testing Concrete Masonry Units and Related Units. *American Society for Testing and Materials*, West Conshohocken, PA., United States.

ASTM C1314-12. (2012). Standard Test Methods for Compressive Strength of Masonry Prisms. *American Society for Testing and Materials*, West Conshohocken, PA., United States.

ASTM C1552-12. (2012). Standard Practice for Capping Concrete Masonry Units, Related Units and Masonry Prisms for Compression Testing. *American Society for Testing and Materials*, West Conshohocken, PA., United States.

ASTM D3039-08. (2008). Standard Test Method for Tensile Properties of Polymer Matrix Composite Materials. *American Society for Testing and Materials*, West Conshohocken, PA., United States.

Italian National Research Council. (2004). Guide for the Design and Construction of Externally Bonded FRP Systems for Strengthening Existing Structures. *CNR-DT 200/2004, Advisory Committee on Technical Recommendation for Construction*. *Rome, Italy, 2004*, 144 pp.

Chen, J.F., and Teng, J.G. (2001). Anchorage Strength Models for FRP and Steel Plates Bonded to Concrete. *Journal of Structural Engineering, Vol . 127, No. 7, July, 2001*, 784-791 pp.

Ehsani, M., and Saadatmanesh, H. (1996). Seismic Retrofit of URM Walls with Fiber Composites. *TMS Journal, December, 1996*, 63-72 pp.

Galati, N., Garbin, E., Tumialan, G., and Nanni, A. (2005). Design Guidelines for Masonry Structures: Out of Plane Loads. *7th International Symposium on Fiber Reinforced Polymer Reinforcement for Concrete Structures, Kansas City, MO. Vol. I, SP-230-16*, 269-288 pp.

Hamilton III, H. R., and Dolan, C. W., (2001). Flexural Capacity of Glass FRP Strengthened Concrete Masonry Walls. *Journal of Composites for Construction, Vol. 5, No. 3, August, 2001*,170-178 pp.

Hamilton III, H.R., Holberg, A., Caspersen. J., and Dolan, C. W., (1999). Strengthening Concrete Masonry with Fiber Reinforced Polymers. *4th International Symposium on Fiber Reinforced Polymer Reinforcement for Concrete Structures, Baltimore, MD.* 1103-1115 pp.

Hamoush, S.A., McGinley, M. W., Mlakar, P., Scott, D., and Murray, K., (2001). Out-of-Plane Strengthening of Masonry Walls with Reinforced Composites. *Journal of Composites for Construction, Vol. 5, No. 3, August, 2001*, 139-145 pp.

Park, R., Priestley, M. J. N., and Gill, W. D., (1982). Ductility of Square-Confined Concrete Columns. *Journal of the Structural Division, Vol. 108, No. 4, April 1982*, 929-950 pp.

Priestley, M. J. N., and Elder, D. M., (1983). Stress-Strain Curves for Unconfined and Confined Concrete Masonry. *ACI Journal, Vol. 80, Issue 3, 1983*, 192-201 pp.

Said, H., and Wu, Z., (2008). Evaluating and Proposing Models of Predicting IC Debonding Failure. *Journal of Composites for Construction, Vol. 12, No. 3, June 1, 2008*, 284-299 pp.

Teng, J. G., Chen, J. F., Smith, S. T., and Lam, L., (2002). FRP-Strengthened RC Structures. *Chichester, England; New York: Wiley, 2002*, 245 pp.

Marshall, T., (2009). On the Performance of Buildings in Hurricanes, A Study for the Saffir-Simspon Scale Committee. *HAAG ENGINEERING CO. October 18, 2009*, 34 pp.

Tumialan, J. G., Morbin, A., Micelli, Francesce., and Nanni, Antonio., (2002). Flexural Strengthening of URM Walls with FRP Laminates. *Third International Conference on Composites in Infrastructure (ICCI 2002), San Francisco, CA, June 10-12, 2002*.

Tumialan, J. G., Galati, N., and Nanni, Antonio., (2003). Fiber-Reinforced Polymer Strengthening of Unreinforced Masonry Walls Subjected to Out-of-Plane Loads. *ACI Structural Journal, Vol. 100, No. 3, May-June 2003*, 321-329 pp.

Velazquez-Dimas, J. I., and Ehsani, M. R., (2002). Modeling Out-of-Plane Behavior of URM Walls Retrofitted with Fiber Composites. *Journal of Composites for Construction, Vol. 4, No. 4, November, 2000*, 172-181 pp.